

## Review

# A comprehensive review on laser powder bed fusion of steels: Processing, microstructure, defects and control methods, mechanical properties, current challenges and future trends

Shubhavardhan Ramadurga Narasimharaju<sup>a</sup>, Wenhan Zeng<sup>a</sup>, Tian Long See<sup>b</sup>, Zicheng Zhu<sup>c</sup>, Paul Scott<sup>a</sup>, Xiangqian Jiang (Jane)<sup>a</sup>, Shan Lou<sup>a,\*</sup>

<sup>a</sup> EPSRC Future Metrology Hub, University of Huddersfield, Huddersfield HD1 3DH, UK

<sup>b</sup> The Manufacturing Technology Centre (MTC), Ansty Park, Coventry CV7 9JU, UK

<sup>c</sup> Advanced Forming Research Centre, National Manufacturing Institute Scotland, Renfrewshire PA4 9LJ, UK

## ARTICLE INFO

## Keywords:

Laser powder bed fusion process  
Steels  
Thermo-physical phenomena  
Microstructure  
Mechanical properties  
Post-process treatments  
Current challenges  
Future trends

## ABSTRACT

Laser Powder Bed Fusion process is regarded as the most versatile metal additive manufacturing process, which has been proven to manufacture near net shape up to 99.9% relative density, with geometrically complex and high-performance metallic parts at reduced time. Steels and iron-based alloys are the most predominant engineering materials used for structural and sub-structural applications. Availability of steels in more than 3500 grades with their wide range of properties including high strength, corrosion resistance, good ductility, low cost, recyclability etc., have put them in forefront of other metallic materials. However, LPBF process of steels and iron-based alloys have not been completely established in industrial applications due to: (i) limited insight available in regards to the processing conditions, (ii) lack of specific materials standards, and (iii) inadequate knowledge to correlate the process parameters and other technical obstacles such as dimensional accuracy from a design model to actual component, part variability, limited feedstock materials, manual post-processing and etc. Continued efforts have been made to address these issues. This review aims to provide an overview of steels and iron-based alloys used in LPBF process by summarizing their key process parameters, describing thermophysical phenomena that is strongly linked to the phase transformation and microstructure evolution during solidification, highlighting metallurgical defects and their potential control methods, along with the impact of various post-process treatments; all of this have a direct impact on the mechanical performance. Finally, a summary of LPBF processed steels and iron-based alloys with functional properties and their application perspectives are presented. This review can provide a foundation of knowledge on LPBF process of steels by identifying missing information from the existing literature.

## 1. Introduction

Since their inception, steels and iron-based alloys have been the leading engineering materials for structural and sub-structural applications [1]. The steels have become part of our day-to-day life, and their importance to our society is extensively revealed by their plenitude of applications. These applications include aerospace, automotive, medical, machinery, nuclear reactors, marine/oil and gas, shipbuilding, food and transportation, electronics and consumer applications [2,3]. According to the World Steel Association, there are over 3500 different

grades of steel produced based on their applications, encompassing unique physical, chemical, and environmental properties [4]. Availability of steels in numerous grades has increased their array of properties including higher strength, higher corrosion resistance, good ductility and toughness, low cost and nearly 100% recyclability etc. [5].

Among the steels family, low carbon alloy stainless steels (SS), particularly 316L SS have been one of the most widely used type due to low cost, ease of processing, good corrosion resistance and excellent toughness even in severe working conditions. The outstanding combination of good corrosion resistance, higher strength and higher

\* Corresponding author.

E-mail addresses: [shubhavardhan.narasimharaju@hud.ac.uk](mailto:shubhavardhan.narasimharaju@hud.ac.uk) (S.R. Narasimharaju), [Z.Wenhan@hud.ac.uk](mailto:Z.Wenhan@hud.ac.uk) (W. Zeng), [TianLong.See@the-mtc.org](mailto:TianLong.See@the-mtc.org) (T.L. See), [zicheng.zhu@strath.ac.uk](mailto:zicheng.zhu@strath.ac.uk) (Z. Zhu), [p.j.scott@hud.ac.uk](mailto:p.j.scott@hud.ac.uk) (P. Scott), [x.jiang@hud.ac.uk](mailto:x.jiang@hud.ac.uk) (X. Jiang), [S.Lou@hud.ac.uk](mailto:S.Lou@hud.ac.uk) (S. Lou).

<https://doi.org/10.1016/j.jmapro.2021.12.033>

Received 25 January 2021; Received in revised form 2 December 2021; Accepted 11 December 2021

Available online 18 January 2022

1526-6125/© 2022 The Authors. Published by Elsevier Ltd on behalf of The Society of Manufacturing Engineers. This is an open access article under the CC BY

license (<http://creativecommons.org/licenses/by/4.0/>).

mechanical properties are the important features of martensitic type steels. Martensitic type steels such as precipitation-hardened (PH) steels (17-4PH & 15-5PH) are basically used in aerospace, chemical, petrochemical, food processing, general metal working, oil & gas, powerplant and injection molding industries [6]. The combination of good corrosion resistance with higher hardness, yield strength and ductility, good weldability and abrasion resistance are necessary for tools and die making industry, tool steels fulfill this criterion. Most commonly used tool steels in metal AM process are the carbon-free maraging steels (18Ni-300) [7]. In addition to splendid high temperature tensile properties, creep resistance and favorable irradiation resistance makes oxide dispersion strengthened (ODS) steels perfect candidates for high temperature turbine blades and heat exchanger tube applications [8]. A taxonomic classification of steels along with their applications is shown in Fig. 1 [9]. In addition to major class of steels (tabulated in Table 1), some of the less studied steel types used in LPBF process are martensitic steels, TRIP/TWIP steels, silicon based (Fe-Si), nickel based (Fe-Ni), and cobalt based (Fe-Co) alloy steels, China low activation martensitic (CLAM) steel and etc.

1.1. The scope of the review

This article is focused to fill the de facto gap by reviewing steels and iron-based alloys used in LPBF process. Firstly, the basics of thermo-physical phenomena operative during LPBF process, solidification by phase transformation, and formation of metallurgical defects and their potential control methods are discussed. Secondly, microstructure, wear and surface texture characteristics, mechanical properties are reviewed.

Furthermore, the significance of post-process treatments on LPBF processed steel components are enumerated. In particular, we concentrate to critically review on how the typical LPBF process parameters have an absolute impact on the formation of; (i) different type (size, morphology) of microstructures, and (ii) process related metallurgical defects. Consequently, how these two combinations have the direct influence on wear and surface texture characteristics and finally on mechanical properties such as hardness, tensile and fatigue properties of as-built and post processed LPBF fabricated steels and iron-based alloys. This article also describes the current state of the art, technological challenges, and future trends, with special emphasis on AM, forecast of AM technology, and its applications in various industrial sectors.

We intentionally do not discuss the details of all types of AM process, instead we restrict our review just to LPBF process. However, other AM processes such as Electron Beam Powder-Bed Fusion (EPBF), Directed Energy Deposition (DED) processes are equally capable of fabricating plethora of steels. Similarly, this review is largely limited to commonly used steels and iron-based alloys; the overwhelming majority (>90%) of referred articles to review this article are concerned with LPBF process of steels. Except in a very few countable occasions, conventional process or other AM process of other metallic alloys have been cited where relevant. Additionally, this review does not extensively cover AM of other similar/dissimilar metal alloys or metal matrix composites (MMC). Discussing all of these would further lengthen this review excessively.

1.2. The organization of the article

The goal of this paper is to provide a critical overview for readers to

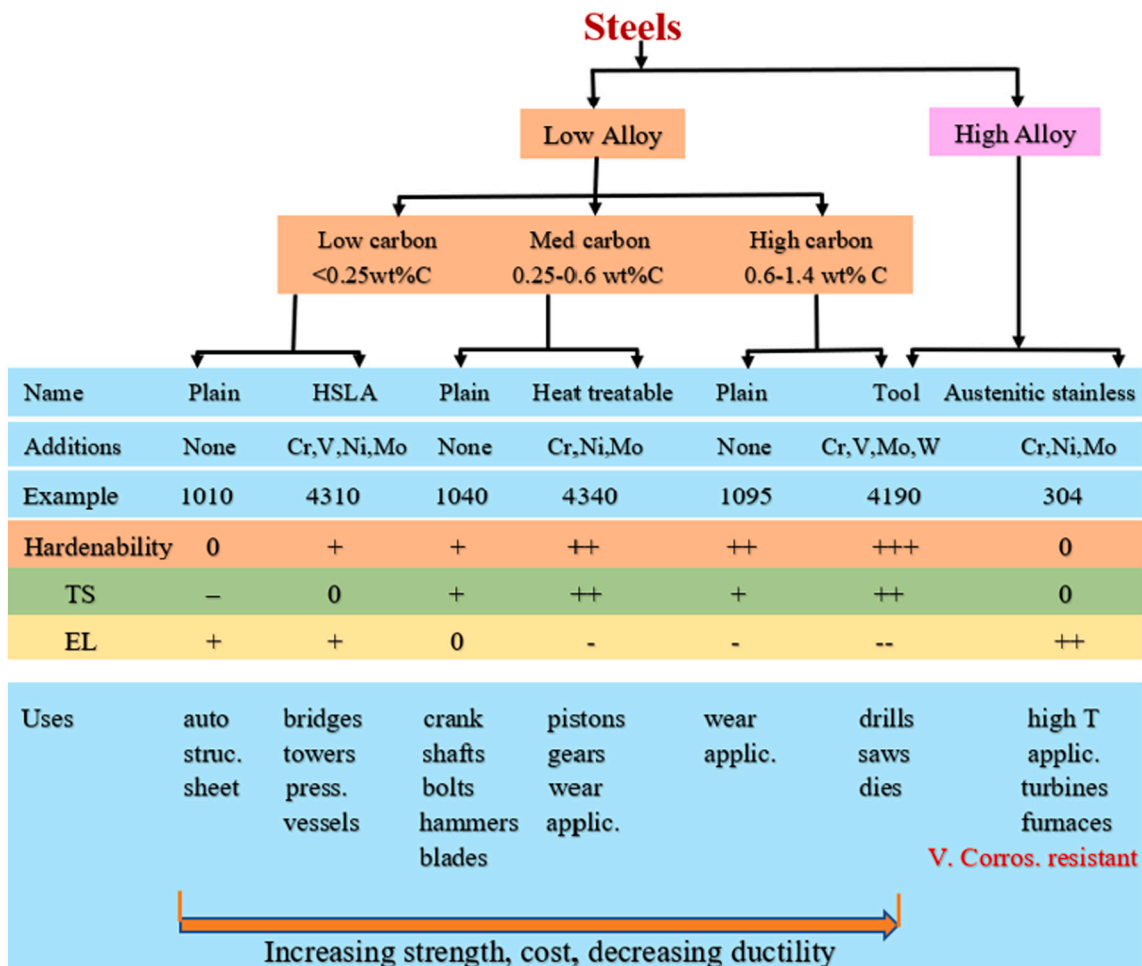


Fig. 1. Taxonomy scheme for various steels. [Based on data provided in Tables 11.1(b), 11.2(b), 11.3, and 11.4, [9]].

**Table 1**  
Chemical composition, mechanical properties of major class of steels fabricated in LPBF process.

Type	Common name/grade	C	Cr	Mn	Mo	Ni	Si	Ti	Others	TS (MPa)	Elongation (%)
Austenitic stainless steel	AISI 316L	<0.08	~17	<2	~2.5	~13	~0.75	–	–	~310	~30
Duplex stainless steel	SAF2705	<0.03	~25	<1.2	~4	~7	<0.8	–	–	~900	~25
PH stainless steel	17-4 PH	<0.07	~17	1	–	~5	1	–	–	~1400	~16
Maraging steel	18-Ni300	<0.03	<0.5	<0.1	~5	~18	<0.1	~0.7	~9 Co	~2050	~8
Carbon bearing steel	AISI H13	~0.4	~5	~0.5	1.15	–	~1	–	–	~1600	~9
ODS steel	PM200	~0.07	19	0.07	0.13	0.03	–	0.5	0.5Y <sub>2</sub> O <sub>3</sub>	~875	~15

gain profound knowledge about the LPBF process of various steels. The review first enlightens introduction to Steels, AM, LPBF and their respective applications. Section 2 is organized to describe the important process parameters, and complex thermophysical phenomena that influences the phase transformation, and evolution of microstructure in LPBF process. A thorough discussion on the defects formation, potential control methods, and common issues that arise during LPBF processing of various steels are addressed in Section 3. Section 4 seeks to critically examine the microstructure, wear and surface texture characteristics, mechanical behavior, i.e., hardness, tensile, and fatigue properties of LPBF of steels on various combined process parameters. Effect of post-process treatments on LPBF processed steels are investigated in Section 5. Finally, Section 6 highlights the summary and future scope. It is therefore hoped that this review will help in understanding the current state of the LPBF technology, the scientific knowledge gaps and the research mostly required for the advancement and extension of LPBF process of steels.

### 1.3. Steels in additive manufacturing and their applications

Currently, steels that are used in structural and automobile applications are mostly manufactured by conventional methods like casting, extrusion, and powder metallurgy [10,11]. The products produced by these traditional processes have been widely used but many problems still persist. The reason pertained to slow cooling rates of casting process induce coarser microstructure, and the defects related to inherent characteristics (porosity, part shrinkage) can subsist simultaneously, which collectively annihilate the mechanical properties [12–14]. Besides, fabrication of steels in the standard process which is time consuming due to a series of independent processes (materials preparation, production and assembly) making it less flexible. With extensive development in manufacturing, special attention has to be paid towards structure-performance requirements of steel components. For example, cellular or lattice type steel structures that are primarily used in working at elevated temperatures under extreme environments (missiles, aircrafts applications) to thwart from oxidation, corrosion while retaining their mechanical integrity [15,16]. Constituent fabrication of complex, functionally graded materials (FGM) for structural components in AM offers greater advantage of saving time, costs and the flexibility (see Fig. 2). More importantly, AM process reduces the weight and stress concentration factors associated with other conventional welding and joining techniques [17,18]. Despite the fact, some of the traditional manufacturing issues still exist in AM process, but the comparative analysis reveals that AM process or LPBF process, have been successful in fabricating defect free (minimum number of process related metallurgical defects) good quality parts exhibiting excellent mechanical properties as compared to conventional processes like casting, extrusion processes [19]. The higher strength is attributed to the combined effect of (AM process induced) refined microstructure (dendritic, cellular type of grains), and potential high dislocation density caused during rapid solidification [19–31]. As the technology continues to advance exponentially, the manufacturing process is no longer about just producing physical products. A fundamental shift is imperative to meet the change in consumer demands, nature of products, and the economics of production and supply chain. Data-driven models using advanced machine

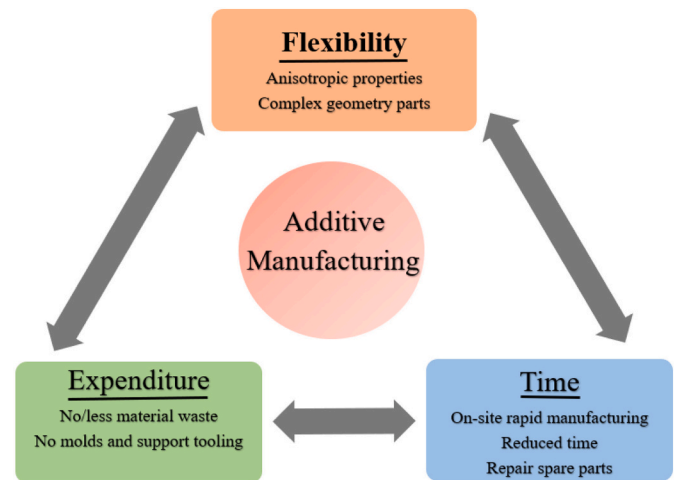


**Fig. 2.** Correlation between Additive manufacturing (AM) key features and its advantages.

learning algorithms, added sensors and connectivity are capable of revolutionizing conventional manufacturing into smarter manufacturing. Fabrication of smart steels products by utilizing the smart and robust AM technology that possess designer surface topography and mechanical performance, highly dense and dimensionally accurate, near net shape parts with reduced requirement of post-processing is going to be a major research and development objective in the future.

AM process is classified into a family of technologies where the material is added, rather than removed to produce an end product. Unlike traditional manufacturing process which involves materials being shaped or carved into required final components by parts of it being subtracted in a variety of ways. AM herein is perceived pole opposite; three dimensional (3D) components are built directly from 3D CAD file by means of an additive strategy-based depositing or melting successive layers of the feedstock materials in an enclosed chamber of the additive manufacturing system. AM is considered as the direct manufacturing technology that gives freedom to fabricate parts from the materials composed of metals, polymers, ceramics, and composites with complex features through external and internal layout, in addition to reduced material consumption [32,33]. The materials used in AM process can be in the form of powder, wire, sheet, etc. [34,35]. AM process is often described by other terms such as additive fabrication, additive technique, additive layer manufacturing, layer manufacturing, solid freeform fabrication and freeform fabrication [36].

Out of many AM processes, LPBF process is currently the most favoured powder bed fusion method which is used to fabricate metallic materials [37]. According to SmarTech Publishing's latest metal AM report "Additive Manufacturing with Metal Powders 2018", LPBF technology is one of the most used and studied AM method [38]. Forecast of AM technologies have been constantly driving the industry revenues resulting from hardware, materials, and software. This revenue growth is predicted (by the Wohler's report 2020) to be worth of \$US 16 billion in 2020, growing to \$US 40.8 billion in 2024 (see Fig. 3) [39].

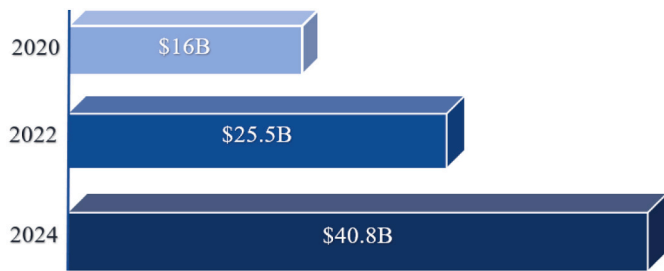


Fig. 3. Forecast of AM Industry growth (Wohler's report 2020) [39].

Metal AM technology has attracted many researchers and industries because of its distinctive applications. In recent years metal AM is used to fabricate end-use products of the medical devices (dental restorations, medical implants), aerospace and military applications, automobile industrial and consumer applications [40] (see Fig. 4a & b). AM is also expanding its territory into aircraft maintenance and transportation sector by production of spare parts and refurbishing the damaged components [41–44].

#### 1.4. Laser powder bed fusion process of steels

Laser powder bed fusion process is also known as Selective Laser Melting that uses a high-power laser beam to selectively melt the predefined contours in subsequent layers of powder. The molten metal pool rapidly solidifies by cooling [46]. Selected regions in each layer are melted by a laser beam, to form a 3D cross-section of the final part. Consequently, the underlying build platform is lowered down, followed

by deposition of another layer of powder with the powder coater/wiper mechanism. This cycle is successively repeated until the three-dimensional solid object is built. The unfused powder is removed and recycled, this entire process is carried out inside a chamber filled with atmospheric gas (Argon, nitrogen), to avoid oxidation (see Fig. 5).

Some applications of LPBF process are shown in Fig. 6. LPBF fabricated products possess higher density with refined microstructure, which contributes to the excellent mechanical properties, superior surface quality and dimensionally accurate final parts. Such a layer-wise production approach offers LPBF process an edge over conventional process in enabling consolidated parts with elaborated internal features

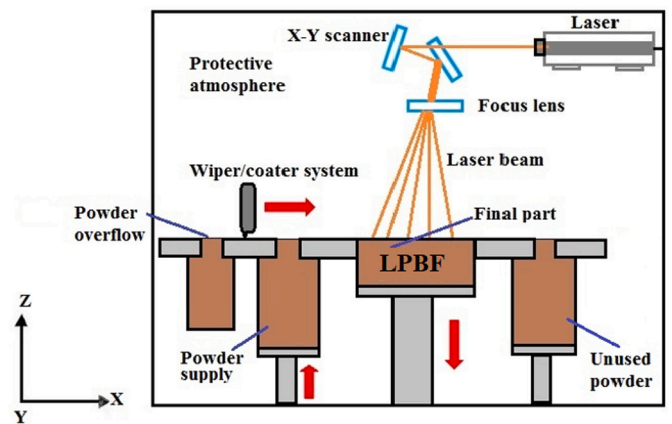


Fig. 5. Schematic illustration of the LPBF process.

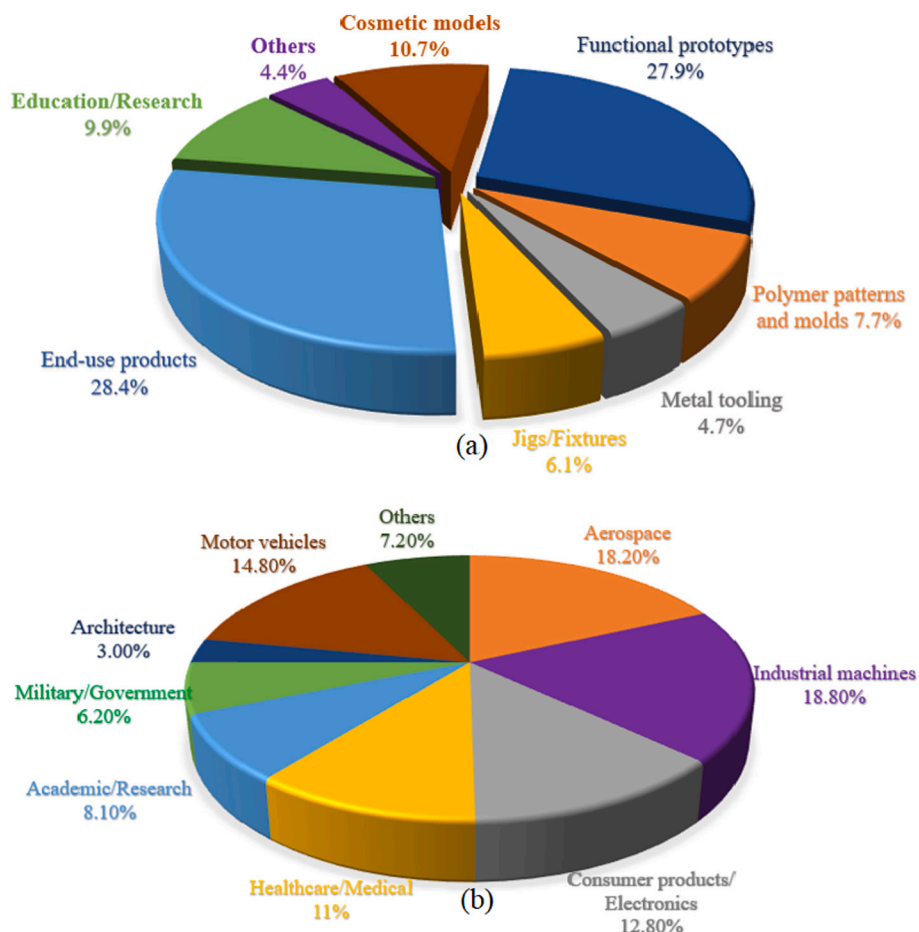


Fig. 4. (a) Categories and (b) Industrial sectors of AM applications based on Wohler's report 2019 [45].

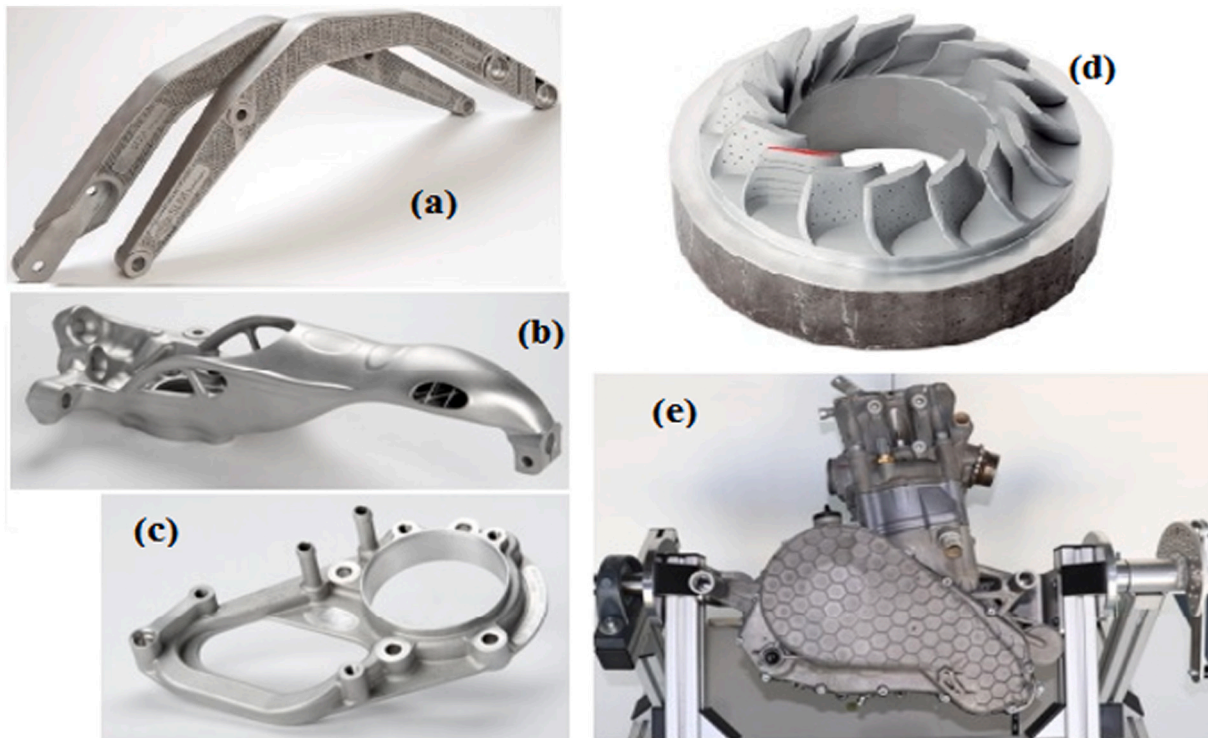


Fig. 6. Various LPBF produced metallic part applications; (a) orthopaedic implant, (b) car steering knuckle, (c) engine mount cooling channel, (d) aircraft engine blades (e) formula student racing engine [43,44].

for complex assembly, higher production rate, reduced design iterations, and quicker introduction of new products/prototypes to the market which were previously considered unfeasible to manufacture functional end-use products promptly [47–52]. The transition from rapid prototyping to fabricating final products also display numerous technological barriers such as part variability, incomplete knowledge related to structure-process-property correlation. Meanwhile, LPBF process undergoes complicated thermodynamic and heat transfer mechanisms. The surface finish of the scan track is uncontrollable and unpredictable during the printing process which eventually affects the final quality of LPBF products [53]. Oxidation of feedstock materials, process induced inevitable thermal residual stresses generated during complex thermophysical phenomena [54], are the most commonly occurring problems. Dimensional accuracy from a design model to the actual part is another issue faced by LPBF technology. Although as-built LPBF components can be directly used as functional parts, aforementioned inherent problems need to be addressed prior to the fabrication of standalone parts, which should overcome to render a reliable, scalable, and high throughput widely adopted LPBF technique as a viable fabrication process.

The laser interaction with the metallic powder generally leads to the formation of a smaller size molten pool approximately 0.9–1.4 mm in length, 0.16–0.63 mm in depth, and 0.12–0.38 mm in width respectively depending upon various LPBF process parameters [55,56]. The cooling rates can reach up to  $10^3$ – $10^8$  K/s due to very fast movement of the laser beam [57,58], again relying on the LPBF processing parameters, type of the material used, and its various physical and chemical properties [59]. Such a high cooling rate can sometimes impede grain growth and segregation of alloying elements. Along with mixing and stirring action of Marangoni convection, and particle accumulated structure formation mechanism, a thin, continuous and unique meta-stable cellular microstructure or in some cases even amorphous microstructure is formed in the molten metal pool [60].

The thin continuous refined microstructure formed is responsible for the significant improvement of the mechanical performance of the LPBF processed steel components. It is important to have both small and large

powder particles: finer particles are easily molten and favour a relatively good part density, design quality surface finish; whereas the larger particles benefit ductility, mechanical strength, hardness and toughness [61,62]. Moreover, LPBF produced components typically display anisotropic microstructure at different length scales. The anisotropic microstructure is generally formed by the rapid solidification process through conduction, convection and radiation, in the direction of heat dissipation [63]. Anisotropy largely depends on the type of scanning strategy employed, base plate temperature, and the build direction [64]. The quality of LPBF processed components depends on the selection of the right parameters combination. A broad spectrum of LPBF process parameters accountable for the complex physical phenomena that is ultimately responsible for final quality of LPBF parts is illustrated in Fig. 7. The summary of these parameters grouped as input parameters, process physics, and outputs. There are more than 150 parameters that need to be considered during LPBF process which are not discussed in detail here. However, some of the most important process parameters (laser power (LP), scan speed (SS), hatch spacing (HS), and layer thickness (LT), atmospheric chamber gas and pressure), and their impact on various physical and mechanical behaviours of LPBF steels are discussed. In the design parameter chart, the output represents the final quality of the LPBF processed product, listed as part geometry, microstructure, mechanical properties, defects, surface roughness, etc.

It is widely known fact that LPBF processed parts primarily exhibit significant anisotropy in microstructure as aforementioned. For example, components built in different directions i.e., parallel (e.g. horizontal) or perpendicular (e.g. vertical) to the substrate undergo a different thermal history which leads to anisotropic mechanical properties, and different surface texture (finish) [52,65]. The ratio between hatch spacing and spot size plays a major role on the process stability that affects the quality of the LPBF products [66]. As a result of opting smaller hatch spacing, a continuous and thin layer is formed due to heat accumulation and slow cooling process in a molten melt pool [67]. In contrast, fully dense, good quality LPBF products were produced even with the selection of large hatch spacing combined with unusually high

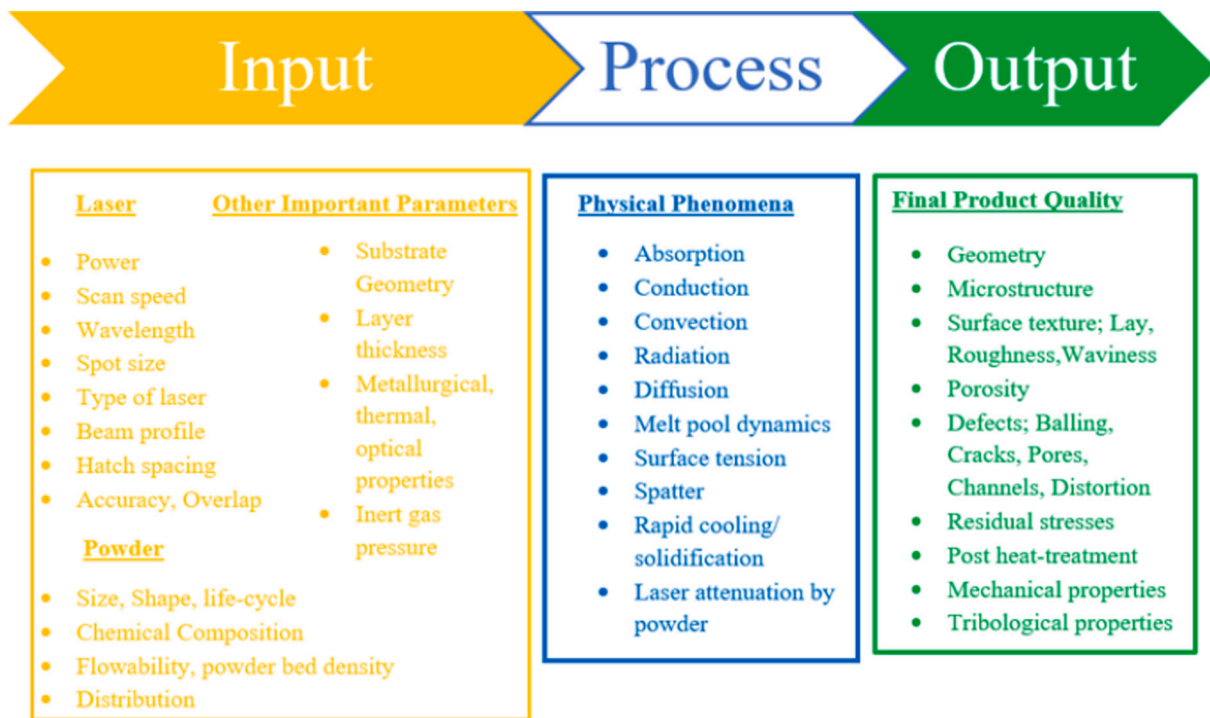


Fig. 7. A detailed process design parameter(s) of the LPBF process.

energy density and increased processing scan speeds [68]. To attain the process stability and good quality LPBF products, it is recommended to choose the average hatch spacing to spot size ratio between 0.6 and 1.5 [69]. Lower energy input or larger layer thickness causes insufficient energy input penetration (to achieve effective overlap) between the melt track layers that lead to the formation of lack of fusion (LOF) or incomplete fusion hole defects [70,71]. Similarly, at a relatively of lower scan speed and at a fixed or higher laser power, the energy input is high resulting in higher thermal stresses and keyhole porosity defects [71,72]. The higher energy input induces greater temperature gradient, combined with the larger thermal residual stresses frequently causes thermal cracks [73,74]. Conversely, at a relatively lower laser power and at a higher scan speed, the supplied low energy input is not sufficient to completely melt the surrounding powder particles (by wetting) leading to the formation of balling defect [75].

It is also evident that higher energy density reduces product dimensional accuracy, making it difficult for process optimization, which may lead to compromise between the specimen dimensionality and defects [76]. From the already published work, adopting higher layer thickness resulted in an decrease in relative density. Consequently, a combination of LPBF layer thickness along with the scan speed influences the microhardness [77–79]. Selection of layer thickness more than 0.1 mm will lead to staircase defects on curved and inclined LPBF built surfaces [80]. In addition to conducting physical experiments, computational modelling of the LPBF process is extremely important to optimize the process parameters. These models are also helpful to predict the complex temperature field of molten melt pool, development of microstructure, residual stresses, distortion, warping and etc. Some of the researchers attempted to correlate experimental and modelling results of LPBF fabricated steels [81–83]. Childs et al. investigated the link between range of laser powers and scan speeds with respect to the formed melt tracks through experiments and modelling of LPBF of M2 tool steel, H13 tool steel, and 314S-HC stainless steels [81,82]. From their research it was clearly shown that, a perfect combination of higher laser power with the lower scanning speed is necessary to achieve stable the melt tracks, as these stable melt tracks are beneficial to manufacture fully dense LPBF parts. Badrossamay et al. studied LPBF process of M2

tool steel and 316L stainless steel through experiments and simulation. Their results revealed that the thermal history of the LPBF process was responsible in ascertaining the amount of melt under the laser fluence. Also, simulation result suggested that the laser absorptivity may increase with increase in the scan speed. The maximum power and scanning speeds used were 200 W and 0.5 mm/s respectively [83]. Li et al. developed a practical multiscale modelling for instant prediction of LPBF steel part distortion [84]. Equivalent heat source was developed by micro-scale laser scan model, local residual stress field was predicted in meso-scale layer hatch model, and finally residual stress model was utilized to predict the part distortion and residual stress in macro-scale part model [84]. Contuzzi et al. evaluated the influence of LPBF process parameters on temperature distribution in a three dimensional model. The simulated results showed good agreement with the real dimension of the melted zone. It was concluded that their simulated model could be used to optimize LPBF of steel process parameters; to predict the bonding between the melt tracks, and to characterize the best building strategy [85]. Peng et al. developed the energy demand model to manufacture the LPBF steel parts (free from porosities) using critical parameters (laser power, scan speed, layer thickness and hatch spacing). The authors reported that the higher power with higher scan speeds results in a relatively thicker layer with stable molten melt pools, thereby producing high density parts. Hatch spacing could be selected based on the actual molten pool. They suggested that this combination effectively reduced energy density, and the corresponding energy demand [86]. Further details about various LPBF modelling methods are presented in relevant subsection 2.4.

LPBF research on different types of steels and iron-based alloys have been carried out mainly to examine the appropriate processing parameters that are suitable to achieve fully dense high quality components and their resultant microstructure. However, the major concern is process insight and manipulation of exact role of (each parameter or combination of) process parameters on physical and mechanical behaviours, and thus compliance with the industrial standards of engineering parts fabricated through LPBF process is not well established. Ascertaining the mechanical properties and surface roughness which are influenced by the process design parameters is also very important that can be helpful

to predict the quality and service of the LPBF components [87]. The use of non-optimized LPBF process parameters contribute to poor mechanical properties due to the formation of various metallurgical defects. Mechanically sound products with relatively high density, refined microstructure, and good surface quality can be produced by choosing a suitable combination of optimal process parameters [69]. Further critical review on linking crucial LPBF parameters with the resultant microstructure, metallurgical defects and mechanical performance have been discussed in the following Sections 3 and 4.

In addition to the most critical LPBF process parameters, metal powder features (particles size and grain distribution, packing density) plays a significant role in determining the final part quality. A decent amount of research has been carried out in this domain [61,88–91]. Spierings et al. investigated the impact of three different particle size distributions (PSD), and different layer thickness on the surface quality and mechanical properties of LPBF stainless steels. It was found that the smaller steel powders with PSD  $D_{50}$  of 15.2  $\mu\text{m}$  and 28.26  $\mu\text{m}$  needed a lesser heat input to achieve 99%-part density than that of the powders with PSD  $D_{50}$  of 37.70  $\mu\text{m}$  [61]. It was attributed to the smaller particles that are easily melted, however, the bigger particles are helpful in undergoing higher elongation before failure. Authors concluded that the PSD not only affects the part density but also affect the surface quality and mechanical properties [61]. Similar kind of results were reported by Liu et al. [89]. They confirmed that the smaller powder particles displayed better flowability resulting in higher density, good surface quality and better strength and hardness [89]. Azizi et al. examined the powder recycling implications on powder characteristics by the virtue of size, distribution, flowability and density measurements [90]. The authors reported only difference in the flowability between the virgin and recycled powders, whereas rest of the characteristics like PSD, phase homogeneity and chemical composition remained unchanged [90]. Coe et al. most recently inspected the single mode and bimodal PSD of LPBF of stainless steels with wide range of energy densities. It is worth noting that bimodal powder with PSD  $D_{50L}$  of 36.31  $\mu\text{m}$  provided slightly higher (2%) tap density than the single mode spherical powders. In addition, bimodal powders utilized higher laser power (>203 W) to reach 99% relative density. Also, as-built bi-modal powders parts showed marginally higher hardness. However, bimodal powders displayed poor flowability [91].

As in the case of LPBF processed steels; various steel and iron-based powders are used as precursor materials, however, there are still lot of uncertain bases which need to be addressed. For example, what is the ideal or universal powder grain size distribution that is best suited for different LPBF processing windows with respect to different types of steel powders. The correlation between the universality of various steels powder characteristics and the processing envelope to achieve highly dense parts, possessing outstanding mechanical properties and excellent surface quality is one of intriguing area that definitely need to be explored.

## 2. Thermo physical phenomena of laser powder bed fusion process

LPBF process generally undergoes a highly complex phenomena, governed by the kinetics and thermodynamic mechanisms that occur at different spatial and temporal time scales. The important thermophysical phenomena that take place within the powder-bed, inside the molten melt pool and in the solidified phase of a typical LPBF process is explained in the following three subsections (Sections 2.1–2.3).

### 2.1. Thermo physical phenomena during the laser-powder bed interaction

The focused laser beam irradiates the surface of the powder bed, leading to the formation of more complex heterogeneous heat transfer phenomena such as powder-bed radiation (between laser beam and the power particles), convection (between the powder bed and the

environment), and finally heat conduction (between the powder bed and building substrate, and/or inside the powder bed) (see Fig. 8a) [92], depending upon various physical, and optical properties of the materials. The focused laser beam absorption is governed by multiple reflections off the oblique surface particles through pores, then it is penetrated and further scattered into a greater depth which can sometimes reach the range of the powder bed layer thickness as shown in the Fig. 8b [93–95]. The photon energy is converted into thermal energy which is dissipated across the powder bed.

The spatial power density distribution of incident laser beam on the powder bed is generally assumed to follow Gaussian distribution, with the associated  $2\sigma$  (standard deviation) value usually being taken as the laser beam spot size. Typical laser spot diameters vary from 25 to 100  $\mu\text{m}$  with the layer thickness lies between 25 and 50  $\mu\text{m}$  depending on the powder morphology and the build material [48]. The choice of lasers depends on the absorptivity of the powder materials [96]. For example; polymers, ceramics, and metal oxides are usually inclined towards the use of continuous CO<sub>2</sub> lasers with a wavelength 10.6  $\mu\text{m}$ , whereas other continuous fibre-lasers (Nd:YAG) with a wavelength:1.1  $\mu\text{m}$  is normally used for processing the metals. In general, the nominal laser power and the laser scan velocities are in the range of  $P \approx 50\text{--}1000$  W, and  $v \approx 0.1\text{--}3$  m/s [97]. The number of factors that influences the overall absorption and local energy distribution includes laser power, wavelength, polarization, angle of incidence, powder temperature, surface roughness, surface oxidation and inclusions/impurities [88,98].

### 2.2. Thermo physical phenomena within the molten melt pool

As soon as the focused laser beam strikes the local positions on the powder surface, the melting temperature is reached and the laser beam instantly melts the powder causing phase transition from solid to liquid droplets leading to the formation of a molten melt pool, (ideally) with a continuous melt track. The formed molten melt pool undergoes very complex physical phenomena driven by buoyancy, gravity, surface tension and capillary forces, due to high thermal gradients induced by the high velocity laser beam onto the metal powders [99]. The transfer of heat within the molten melt pool is dominated by thermo-capillary-convection or Marangoni convection which drives the molten liquid metal from the hotter laser spot to the cold rear, (see Fig. 9) influenced by the temperature dependent surface tension [99,100], and particle accumulated structure (PAS) formation mechanism [60]. Surface tension, capillary forces, wetting behavior, as well as inertia effects are considered as the primary driving forces [101–103]. Viscosity and gravity forces are considered as secondary effects that influence the melt pool kinetics, thermodynamics, geometry as well as the surrounding powder morphology by attracting or rejecting individual powder grains [102]. The interaction of both primary and secondary forces would decide the stability and the final geometry of melt track. The shape of the molten melt pools are generally controlled by the surface tension and capillary flow, and thus it can be controlled by adjusting the laser processing parameters [104]. Formation of the molten metal pool is considered as the first point of solidification microstructure.

### 2.3. Thermo physical phenomena within the solidified phase

Metallurgical microstructure is instantly established when the solidification of molten melt pool begins. The solidified microstructure determines the macroscopic properties of the final LPBF built product. The phase transformation of the solidified microstructure is distinguished by the grain morphology and grain texture which are influenced by the prevalent spatial temperature gradients, cooling rates, as well as the velocity of the solidification front [106]. The solidification process in LPBF process are classified into two regions; the first region consists of the temperature field which is in direct contact with the laser beam (fusion zone), and the heat affected zone (HAZ) [107]. The first region undergoes highly complex kinetic and thermodynamic mechanisms

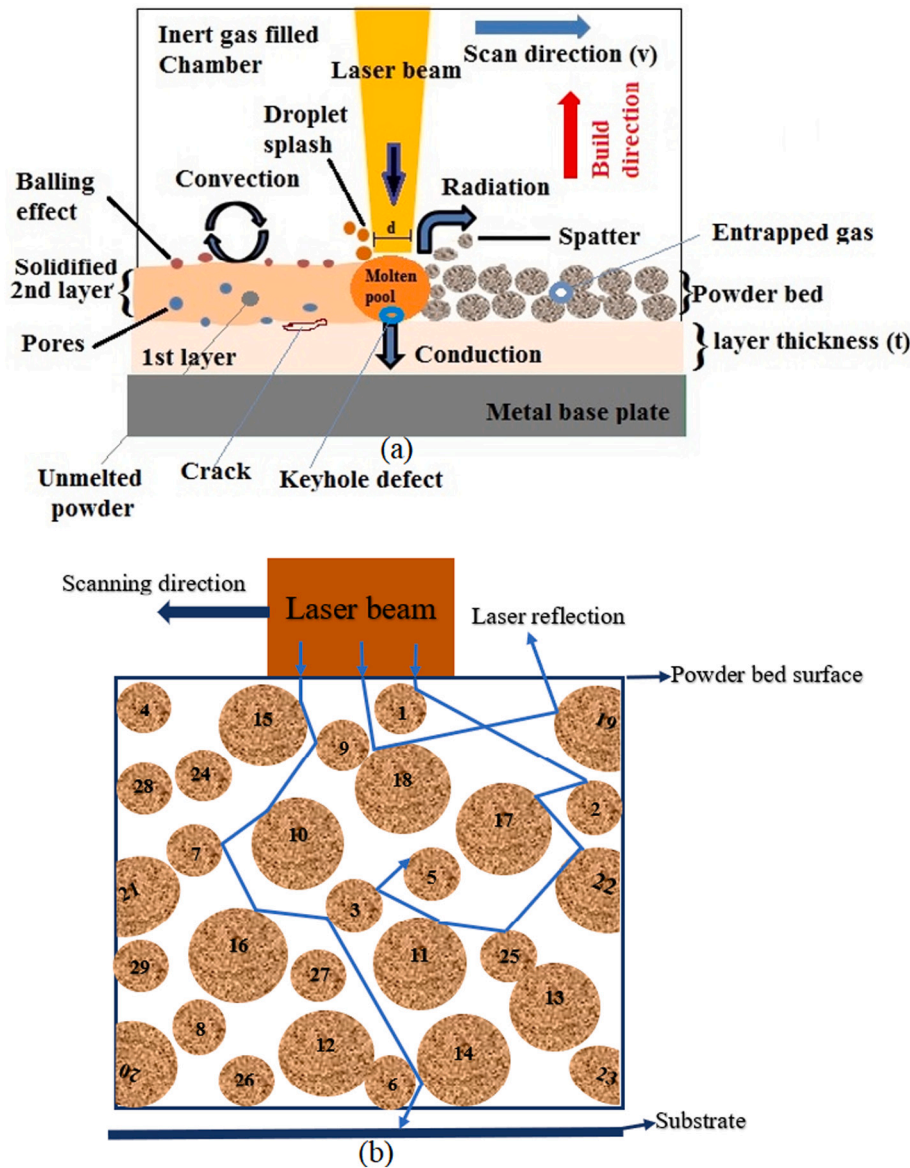


Fig. 8. Schematic illustration of thermophysical phenomena in LPBF process (a) various heat transfer phenomena, (b) interaction between laser beam and powder bed.

within the molten melt pool with all the individual physical phenomena as explained in the previous sections. These distinct non-equilibrium condition during LPBF process results in formation of fine grain metastable microstructures [60], and compositions of the resulting phases, typically give rise to superior mechanical properties [108–110]. In the second region (HAZ), the thermal evolution is predominant in already deposited layers, located below the current layer and further away from the laser heat source which are exposed to prolonged repeated heating and cooling cycles resulting in solid phase transformations and grain coarsening [109–112].

#### 2.4. Summary of relevant studies on thermophysical phenomena of LPBF process of steels

Based on the available literature, there are three kinds of computational models namely analytical models, empirical models and numerical models. Analytical models focus on the physics side of the process, and they tend to be beneficial to optimize process parameters. These models require high computation time to capture the complex thermophysical phenomena of the molten melt pool. Analytical methods are

accountable to model the part of process physics with different prediction accuracy, they do not incorporate the multi-physics, and thus are less effective since more complex physics is involved during LPBF process. Fathi et al. studied a mathematical model accustoming a parabolic equation to build the molten melt pool's top surface during laser powder deposition [113]. The temperature distribution inside the clad and substrate was acquired by solving the heat conduction equation based on an infinitely fast-moving laser heat source. This model enabled to the predict molten melt pool depth, temperature field and the dilution as a function of clad height and width [113]. Mirkoohi et al. investigated a three-dimensional (3D) semi-elliptical model with moving heat source approach to predict the in-process temperature profile inside LPBF processed part [114]. The authors further studied the effect of time spacing (laser pulse), the impact of number of scans and hatch spacing on the thermal properties and the molten melt pool geometry. From this analytical model, few details were considered to predict the geometry of the molten melt pool more precisely and realistically [114]. Lee et al. developed a novel hybrid heat source model to predict and analyse melt pool characteristics including molten melt pool dimensions and melting modes of LPBF processed steels [115]. This formulated hybrid model

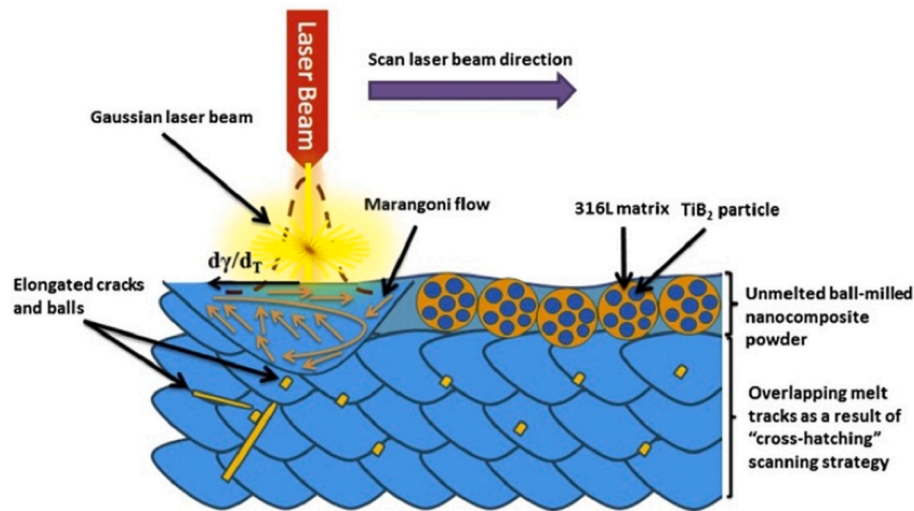


Fig. 9. Schematic illustration of Marangoni convection (flow) during LPBF process [105].

considered different absorption mechanisms for the porous and dense-state materials, and an effective absorptivity was employed to analyse melting mode transitions [115].

Empirical models are more case sensitive, but are time-efficient compared to numerical models. Numerical modelling method in LPBF process draws great research interest in both academia and industry fraternity. Numerical methods are used to simulate the laser interaction with powder particles, molten melt pool formation and the thermal stress field distributions in LPBF process [116–121]. Numerical methods in LPBF process are categorised as microscopic, mesoscopic, and macroscopic scale models. As the name indicates microscopic models usually deals with thermo-mechanical phenomena that takes place in microscopic level such as energy absorption, heat conduction, convection, radiation, thermo capillary effects, Marangoni effect and recoil pressure [116]. Additionally, microscopic models also comprised of stable/unstable phase transformations, microstructure evolution involving size, shape and the orientation of resultant grains in the molten melt pool. Ninpetch et al. developed a power scale computational fluid dynamics (CFD) model to study the thermal behavior, molten metal pool flow characteristics of LPBF processed steel, and also to analyse the influence of laser power, scan speed on the melt track formation [116]. It was revealed from the results that CFD model could be used to describe the complex thermophysical phenomena like heat transfer and molten melt pool characteristics, along with the laser scan track width and depth entity [116]. Lindroos et al. formulated a novel thermomechanical crystal plasticity model which demonstrated the microscale level structure evolution, residual stresses, and the strains in a single track LPBF processed H13 steels [117]. Their model effectively addressed the microscale residual stress anomalies that depend on molten melt pool thermal, and microstructural evolution, phase transformations and the interplay with the surrounding matrix of H13 steel. It was concluded this microscale model was exceptionally robust in predicting microstructural residual stresses and the deformation [117]. Mesoscale models are generally utilized to address the solitary grain and the complex thermo-hydrodynamic phenomena of molten melt pool during LPBF process. These types of models are helpful to study the bonding properties between the successive melt track layers, which determines the formation of process related metallurgical defects, responsible for the surface quality of the final part. L. Cao simulated mesoscale multi-layer multi path forming process to predict the molten melt pool behavior dynamics of LPBF built steel. Impact of three scan strategies on grain orientation, porosities and the surface morphology were investigated and compared with the experimental results [118]. It was found that the grain orientation of current formed layer of the first

scan strategy and the third scan strategy was almost same as that of already formed layer, however, the reported grain orientation of current formed layer under the second scan strategy was significantly different from that of already formed layer. Additionally, they reported porosities and the surface morphology in scan strategy three was lower than the other two scan strategies [118]. Lie et al. developed a new ray tracing heat source 3D mesoscale simulation for LPBF processing of steels [119]. The simulated model analysed the laser interactions with the powder bed, considering the multiple laser reflections from the surface of the steel powder. It was found that the proposed ray tracing heat source model was able to simulate the laser heating process of LPBF process better than the conventional one. In addition, this model was successful in identifying the local defects such as balling [119]. Macroscopic models mainly focus on simulating the whole fabrication of LPBF parts. Macroscopic models are accountable for predicting the spatial temperature distributions, residual stresses, distortion, warping of LPBFed parts. Li et al. developed a geometry scalable predictive model across the microscale laser scan, mesoscale layer hatch and the macroscale part build-up to quickly predict the residual stresses and distortion with respect to different scanning strategies [122]. The model predictions were validated by experimental data, it was found that the geometry scalability law in context of layer thickness is achievable for the complex part geometries to predict the residual stresses and distortion without compromising the accuracy. The authors concluded that adapting orthogonal scanning pattern between the two adjacent layers was beneficial to reduce the residual stresses and distortion [122]. Shiomi et al. studied the distribution of residual stress model, and proposed base plate pre-heating, stress relieving heat treatment and laser re-scanning methods to reduce the residual stress formed during LPBF processing of steel [123]. Li et al. evaluated finite element analysis (FEA) model to predict the transient thermal stress field, and optimize LPBF process parameters to analyse these impact on residual stresses and deformation [124]. This FEA predictive numerical model could be used as an effective tool for the parametric study of LPBF process parameters, residual stresses and deformation [124]. Altogether, multi-scale computational models are therefore considered as the basic reliable tools to understand the complex thermophysical phenomena that occur in LPBF process. Concurrently, these basic reliable tools could serve as predecessor to design physical experiments.

For further information related to computational modelling methods in context of LPBF process of steels; interested readers are requested to refer these articles [125–129]. Overall, publications on modelling studies of LPBF process are abundantly available, however, the research specific to the simulation of LPBF process of steels and iron-based alloys

are limited.

## 2.5. Solidification theory of laser powder bed fusion process

To understand the formation of microstructure and property evolution of LPBF processed parts, it is crucial to ascertain solidification theory and the associated thermal behavior.

During conventional welding or similar processes, nucleation begins at existing base-metal grains in the fusion line which act as a substrate, and these grains grow towards the centre of the weld by epitaxial growth (see Fig. 10). Since the molten melt pool is in intimate contact with the base-metal grains, it (molten melt pool) completely wets these base-metal grains [130]. Homogeneous nucleation typically requires larger time scales which is unachievable in LPBF process. Nucleation is commonly initiated at the solid-liquid interface between the base metal grains surface and liquid metal pool [131,132]. The solidification commences at the molten melt pool boundary and directed towards the centre of the melt pool itself [133]. LPBF process induces heterogeneous nucleation at the molten pool boundary, and epitaxy grains growth with columnar solidification front. These grains grow randomly in the direction perpendicular to the molten melt pool boundary, and along the maximum temperature gradient, that facilitates the maximum heat extraction and the highest degree of undercooling [134–136]. As a result of epitaxial nucleation, columnar dendrites or cells within each grain tends to grow in preferred crystallographic direction  $\langle 100 \rangle$  [137]. This is the conducive crystal growth direction or commonly observed solidification texture for cubic crystals including face-centred cubic (FCC), and body-centred cubic (BCC) metals [130,138]. The crystallographic orientation mainly depends on the scan strategies [131]. The growth of columnar grains in LPBF process of steels with a strong texture of  $\langle 100 \rangle$  preferentially aligned to the build direction (Z-axis) [138,140].

It is well established that directional solidification microstructure of metal alloys is determined by the effect of two apparent parameters: temperature gradient at the solid-liquid interface “ $G$ ”, and growth rate of the solidifying front (or solidification rate) “ $R$ ” (see Fig. 11).  $G$  and  $R$  dominate the solidification microstructure together [137]. The ratio between temperature gradient and growth rate ( $G/R$ ) decides the morphology of the solidified grains, while the product of these two quantities ( $G \cdot R$ ) determines the cooling rate of the material within the solidification interval and therefore controls the size of the resulting microstructure [130,137]. The fast cooling and rapid solidification of the molten melt pool in LPBF process primarily depend on the energy density, and the scan velocity [141–143]. As shown in Fig. 11, the microstructure evolution by solidification undergoes a morphological transformation from the planar front to the equiaxed dendrites as the

degree of constitutional supercooling increases [144,145].

The constitutional supercooling region does not exist in planar microstructure, as the temperature gradient  $G_a$  at the front of solid-liquid (S/L) interface is relatively high, but the actual temperature in liquid phase is higher than the liquidus temperature ( $T_L$ ) (see Fig. 12a). The embryos advancing are re-melted by the molten melt pool causing smooth interface without any solute segregation in grains. Due to the low temperature gradient  $G_b$  of the liquidus phase, constitutional supercooling region is apparent, resulting in cellular microstructure. Numerous small, equidistant, and prismatic grains with hexagonal cross-section are formed at S/L interface which extends into the supercooled liquid due to unstable state of planar crystal interface (Fig. 12b) [145,146]. The constituent (solute) is rejected towards the lateral sub-grain boundaries, as the corresponding  $T_L$  of sub-grain boundary decreases. When temperature gradient  $G_c$  is further decreased, already formed cellular crystalline microstructure penetrates deep inside the liquid for a prolonged depth, also results in constitutional supercooling in transverse direction (Fig. 12c). The coexistence of columnar or equiaxed dendrites, along with the liquid phase in a sensitive region is called as mushy zone [146]. It is quite appealing to notice that a very high degree of constitutional supercooling in this mushy zone (Fig. 12d). This phenomenon is attributed to temperature gradient, crystallization rate, and the Gaussian distribution of the laser energy, as well as distribution of the supercooling of the molten melt pool in different zones [147]. Hence, the formation of different types of grains is expected in the solidified microstructure [148,149]. Further information about the solidification theory of LPBF process can be referred to [150,151].

It is evident that laser power, scanning velocity, and different building directions affects the grain features of LPBF built parts. Elongated grains (Fig. 13a) are prevalent in the building direction, while the equiaxed grains are apparent in the transverse direction (see Fig. 13b) [152]. The faster cooling rate sometimes affect the sub-structure grain boundary formation, resulting higher hardness and wear resistance due to evenly distributed fine dendrites on a surface [153,154].

## 3. Formation of metallurgical defects and their potential control methods

Formation of metallurgical defects such as; balling, porosities, key-holes, cracks, metal inclusions, residual stresses, warping, delamination, oxidation, loss of alloying elements, denudation etc., and surface asperities namely; staircase effect, partially-melted/un-melted particles, spatters, re-entrant features [155] etc., are commonly observed during metal LPBF process (see Fig. 14). Incorrect selection of process parameters would likely introduce inevitable metallurgical

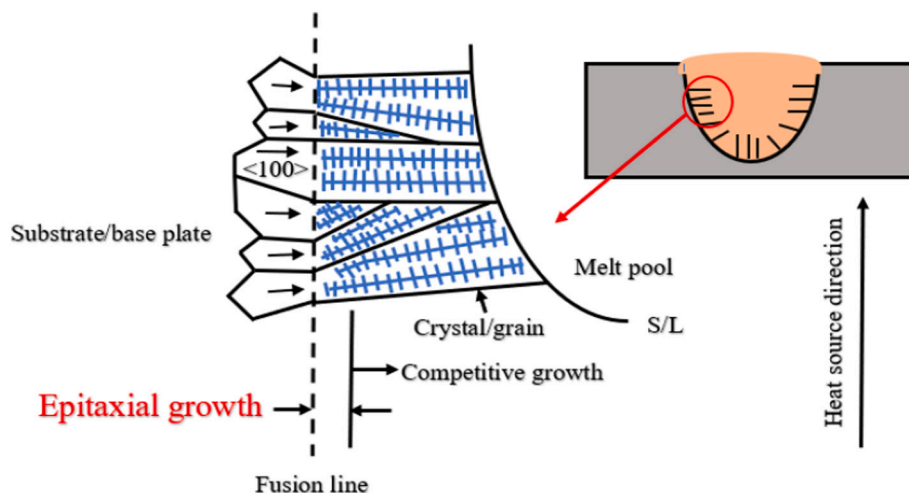


Fig. 10. Schematic illustration of epitaxial growth in LPBF process, similar to conventional welding [130].

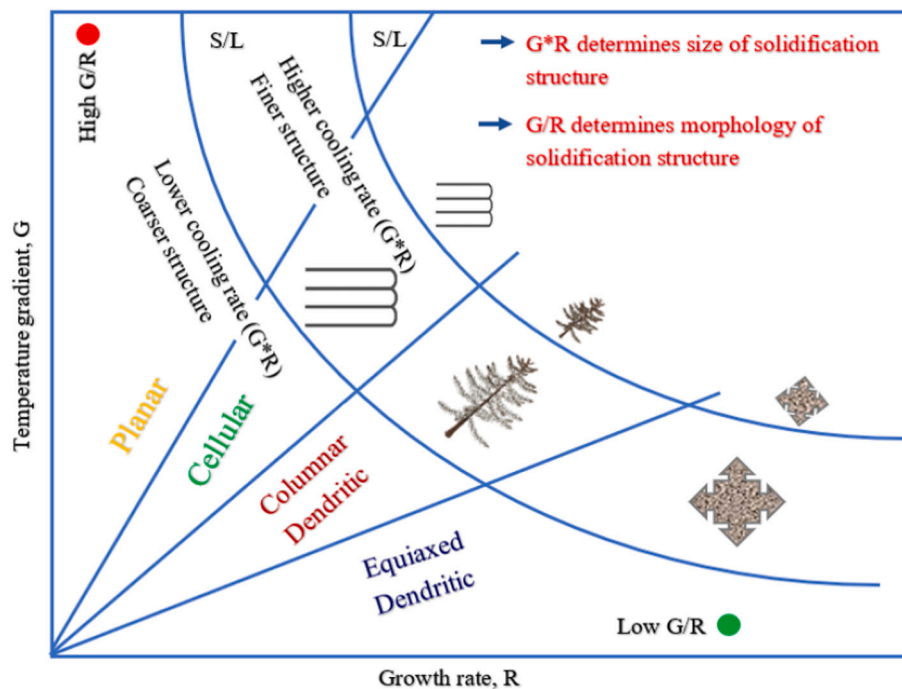


Fig. 11. Effect of temperature gradient  $G$  and growth rate  $R$  on the morphology and size of solidification microstructure [130].

defects and surface asperities into LPBF fabricated part, which causes adverse effect on the resultant microstructure, surface texture, physical and mechanical properties [156].

### 3.1. Balling

Balling phenomenon is described by the Plateau-Rayleigh capillary instability, which occurs when the deposited melt track sometimes tends to break up into half-cylindrical shape or into spherical balls [157]. This phenomenon depends on the process variables such as scanning speed, surface tension, viscosity and density of the materials deposited [158]. Balling phenomena is one of the critical surface defects which is considered as the severe processing defect in LPBF process [159]. Surface tension and wettability have a greater impact on the formation of molten melt pool. The combination of surface tension and capillary forces drive the molten pool to shrink into its lower surface energy state (a sphere), when coalescence of individual melt tracks is in poor contact with underlying substrate results in the formation of balling defect [157]. In other words, balling defect can also occur when the liquid phase present along the surface and grain boundaries of molten melt pool fails to completely wet the remaining solid particles and the underlying substrate due to the presence of surface impurity [103]. The balling defect leads to pores, higher surface roughness, reduced density, causes lack of fusion between the powder particles/layers, imparts irregular melt tracks, and in some extreme conditions causes obstruction to the deposition process [159]. Severe balling phenomenon on a certain melt track layer inevitably leads to the formation of humping or ripple effect [160]. These ripples can carry forward onto the next layer resulting in lack of coalescence between the layers causing poor metallurgical bonding, and induce low part density. Ripple defect contribute to stacking of materials that can have serious impact on the surface quality of the scan track resulting in poor surface roughness of LPBF built 316L stainless steels [160].

When the laser beam incident on the powder bed, melting starts instantly at the local positions of powder particles surface. The phase transition from solid to the liquid molten 'cluster' is formed between the surrounding powder particles, causing reduction in surface area that gives rise to agglomeration. The selected laser spot size is usually bigger

than the (starting) particles size. As the powder particles are melted together, smaller agglomerates gradually grow and are bound to form significantly bigger agglomerates (coarsening). As this process continues, a further reduction in surface tension of the molten melt pool tends to form a ball-shaped structures (balling). The dimensions of these formed balling structures are several times bigger than the original particle size (see Fig. 15) [159].

High surface tension and viscosity are the two important hydrodynamic forces that enhance balling initiation. Higher laser energy density induces more heat to form a bigger geometry molten melt pool and a wider region of contact with the substrate. The bigger and wider molten melt pool decreases the viscosity and increases the liquid metal flowability (wettability) thereby, limiting the tendency of balling (see Fig. 16) [161]. However, employing extreme laser power and scan velocity give rise to various detrimental effects. Excess heat input causes vaporization by over-heating the molten melt pool. As shown in Fig. 17a & b, intense vaporization is generally observed at the top surface of the molten melt pool due to Gaussian beam heating and the highest recoil pressure right underneath the laser beam. The combination of excessive heating and the higher recoil pressure lead to the ejection of metal vapour jet plume in the form of hot spatters, un-melted powder particles that converted into powder splashes [158]. Laser re-melting can be employed on each of the fully molten metal layer to enhance the microstructure, thereby overcoming balling phenomena. Laser re-melting is also helpful to minimize the spatters by rewetting the substrate at the expense of longer production times [162,163].

Similarly, preheating the base plate can improve the flowability between liquid metal and the substrate that results in the formation of a better metallurgical bond, and subsequently reduces the (balling) contraction effect arising from surface tension [164]. Nevertheless, excessive preheating chamber temperature causes droplet spatters which again lead to the formation cluster of partially melted powders obstructing the molten melt pool wettability. The preheating temperature during LPBF process of steels ranges from 80 to 900 °C [165].

### 3.2. Porosity

The degree of metal powders compactness is generally low. In

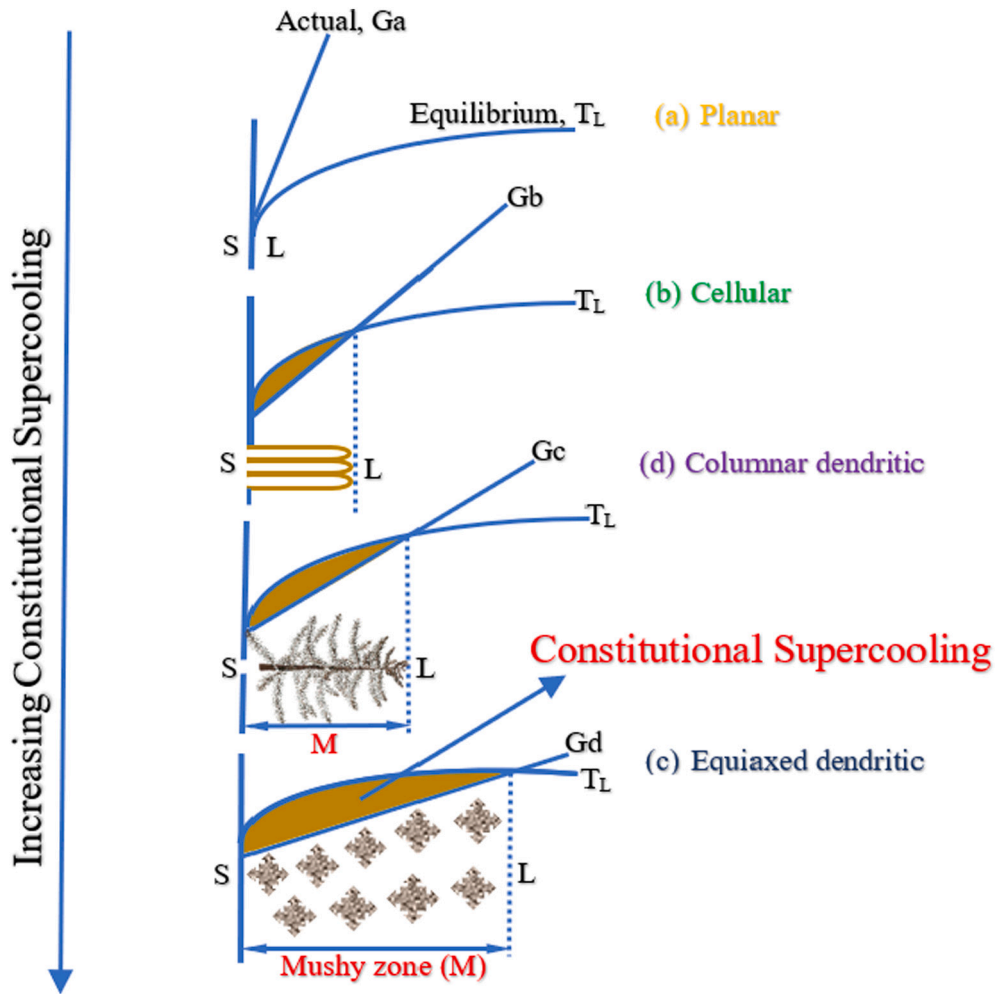


Fig. 12. Effect of constitutional supercooling on solidification mode: (a) planar; (b) cellular; (c) columnar dendritic; (d) equiaxed dendritic (S, L, and M denote solid, liquid, and mushy zone, respectively) [130].

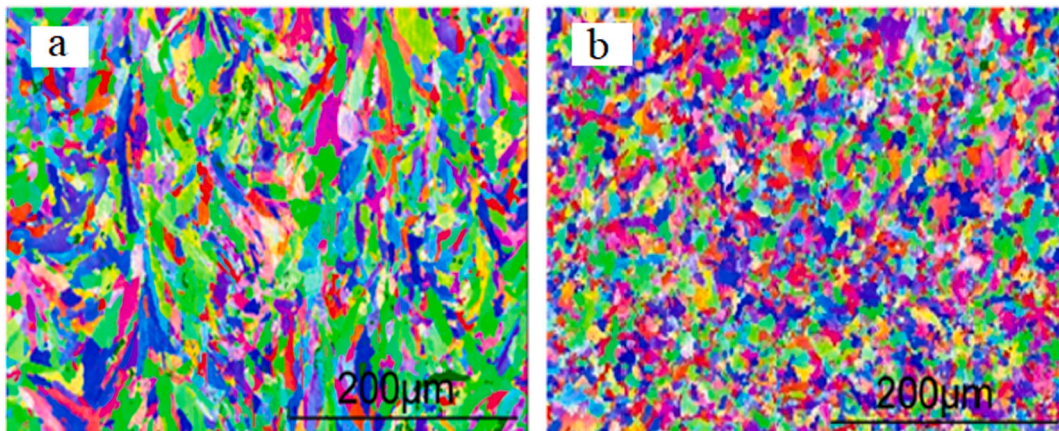


Fig. 13. Electron backscattered diffraction (EBSD) images of (a) elongated grains in the build direction and (b) equiaxed grains in the transverse direction [24].

addition, existing gas in the powder particles can easily diffuse into molten melt pool which cannot escape out of the molten melt pool surface due to rapid cooling and solidification. Thus, porosity is formed in LPBF fabricated steel parts [167]. Conversely, the gas solubility in liquid metal is commonly high at elevated temperatures which also contribute to the formation of pores. The porosity defects in LPBF process could be classified into incomplete fusion holes, keyhole/or

depression defect and voids [167–170].

Incomplete fusion holes are related to insufficient energy input that fails to completely melt the metal powders and inadequate penetration of liquid metal into previously solidified layer causing poor metallurgical bonding [171]. The lack of fusion defects can range up to a few hundreds of microns which basically are irregular in shape, and are commonly formed at the melt track layers interface. If the supplied heat



Fig. 14. List of various metallurgical defects and surface asperities emerge during LPBF process.

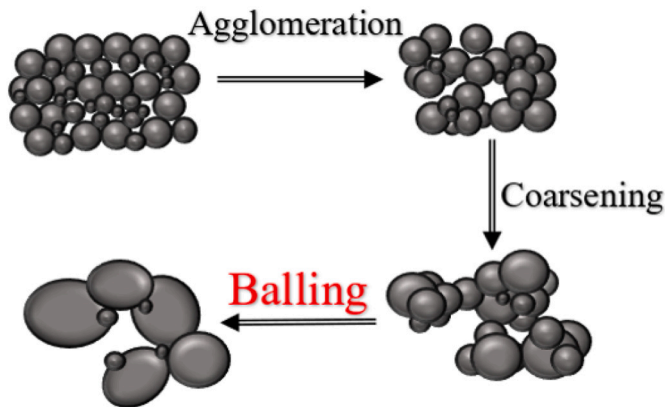


Fig. 15. Schematic illustration of balling phenomena [159].

input is low, then the formed width of the molten pool becomes too small. The less wider molten melt pool lead to an insufficient overlap between the melt tracks. This insufficient overlap gives rise to the formation of un-melted powders at melt tracks interface (Fig. 18a & b). As a result of incomplete fusion holes, the surface of this location becomes rough which directly obstructs the flow of molten pool causing inter-layer defects. These interlayer defects gradually propagate as the process continues, finally to form a multi-layer defect [167,168].

The keyhole pores are usually spherical (Fig. 18c & f) in shape caused by the gas bubbles trapped inside the powder particles in the powder mass. The keyhole pores are also attributed to very high laser energy density [31], which leads to the vaporization of low melting point elements within the alloy in the form of gas bubbles. The vapour bubbles can be trapped by fast moving laser beam and sometimes be easily

dragged to the bottom of the molten melt pool by convective currents. The fast solidification rate does not allow these gas bubbles to arise and escape from the molten melt pool [172,173]. The spherical pores are formed due to trapped gases inside the powders during the powder atomization process or inside the molten pool during LPBF processes. In some cases, keyhole pore is also referred as depression defect that can exist at the end of a melt track with a width almost equal to the laser spot size (Fig. 18e) [169–171]. End-hole is ascribed to very high scan velocities, where laser irradiation time is not sufficient for a deep keyhole formation, instead, an open pore is created at the end of the melt track surface. End hole pore is usually induced by the dominant downward recoil pressure that is exponentially dependent on the temperature of the molten melt pool region which is directly under the laser beam [169,174].

Void formation is not entirely limited to low laser energy input. Perhaps, it also depends on the stability of the melt track. Voids could be either trapped gas pores, lack-of fusion holes or keyhole pore induced porosities [158]. Voids are characterized by inside layered morphology associated to molten melt pool boundaries (Fig. 18d). Void defects normally originate from the higher residual stresses generated by the rapid cooling of the molten melt pool, also sometimes could nurture the formation of cracks along the melt pool boundaries, leading to final segregation and void formation [167]. There is a strong possibility of voids or open porosity to occur at a higher scanning speeds due to inability of the liquid metal flow to completely fill the surrounding area, where the shielding gas is originally present (see Fig. 19). Insufficient filling of the neighbouring gaseous region and rapid cooling rates leads to the generation of voids or open porosity of several hundreds of microns at the surface and distributed along the overlapping gaps [173].

Porosities can lead to serious metallurgical defects, yield lower part density, and adversely affect the surface texture and mechanical performance of LPBF fabricated steels. The strategies used to suppress

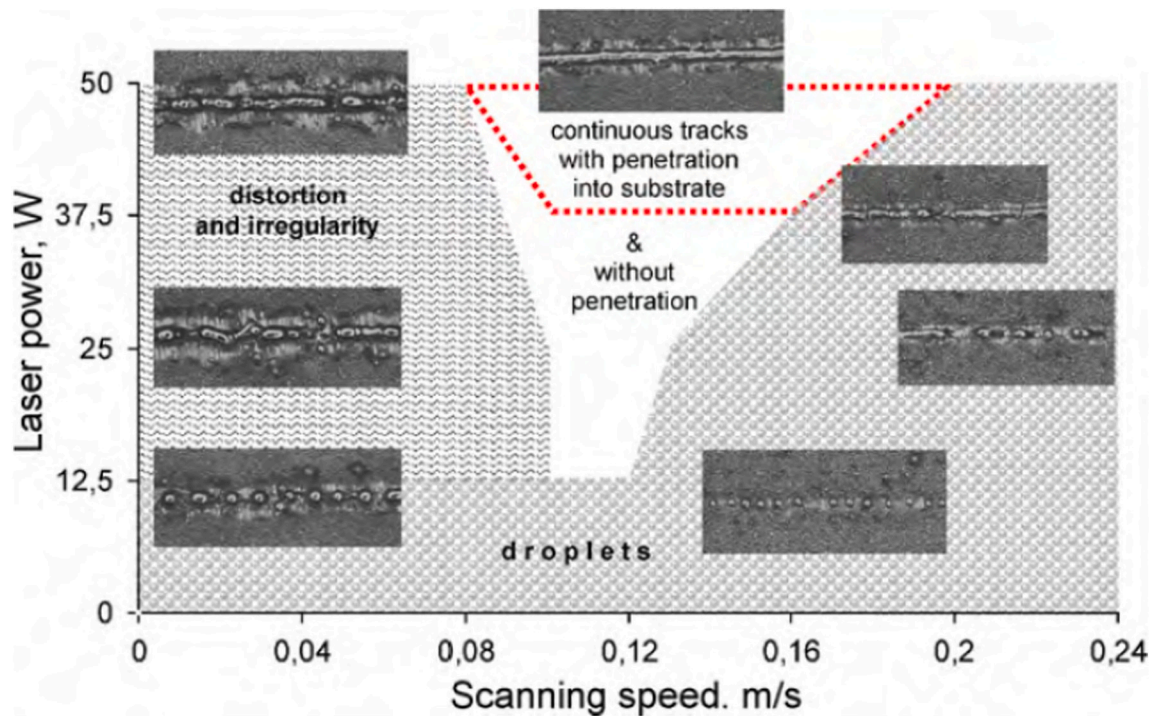


Fig. 16. Single track process map for the first layer of stainless-steel grade 316L [161].

balling are equally applicable to limit the porosities. For example, substrate preheating, [176] and employing laser re-melting reduces porosity. Selection of adequate process parameters that produce sufficient liquid metal and the larger molten metal pool lifetime is considered to be beneficial to eliminate the surrounding gas pores (region) during LPBF process.

### 3.3. Residual stress and cracking

Residual stress is a characteristic of the thermal manufacturing processes, and parts produced by LPBF process are especially vulnerable to residual stresses. Residual stresses can also lead to the formation of various building defects associated with LPBF parts failure [177]. Higher temperature gradients and densification ratio which are attributed to the LPBF process, tend to create higher residual stresses. High thermal stresses cause surface defects and porosity that normally occur around the melt pool. In extreme cases, higher residual stresses results in part distortion, shrinkage, cracking, warping and delamination of LPBF produced part from its support structures. As a result of this, resultant mechanical properties, part density, dimensional accuracy of LPBF parts tends to be substantially compromised [84,153,177].

Thermal stresses generally occur from the temperature gradient or the solidification-induced shrinkage of adjacent laser melted zones in solidified material, thereby a decrease in thermal stresses would also result in a decreased residual stresses. Thermal stresses are mainly responsible for cracking. Based on the expansion behavior of the material heating or cooling, thermal stresses formed during LPBF process are classified into (i) temperature gradient mechanism (TGM) in the solid substrate (ii) cool-down phase of the melted top layers [178]. In the first case, the top layers of the solid substrate expand thermally when it experiences the high thermal energy gradients induced by the laser beam. The thermal expansion is restricted by the colder underlying solidified layers. This induces elastic compressive stresses in the top layers of the substrate. The thermal expansion may exceed the yield stress of the material and upend the plastic deformation of top layers in the direction of the laser energy source (Fig. 20a). However, when it reaches the yield stress point, the compressive stresses in the material causes

plastic deformation of the top layers. As the plastically deformed layers cool down, printed material layer contracts and bend in the opposite direction (see Fig. 20b). As a result, the compressive stresses are converted into residual tensile stresses that induce cracking in the LPBF processed parts [178]. In the second case, already melted upper layer temperature is higher at the beginning as compared to the underlying layer. When the molten melt pool is cooled and solidified, upper layer tends to shrink to a greater extent due to thermal contraction. Although, this deformation is again inhibited by the underlying colder layers. Thus, tensile stresses are introduced in the upper layer and the compressive stresses in the bottom layers [178–180]. Due to the complexity of LPBF process and the difficulty in experimental measurement, finite element simulation methods are commonly used to predict the distribution and evolution of residual stresses [84].

Cracking in LPBF process can be divided into solidification cracking and liquation cracking (Fig. 21a & b). Solidification cracking occurs in the terminal stages of the solidification when dendrites have almost fully grown into equiaxed grains, which are separated by a small residual liquid strip in the form of grain-boundary films in mushy zone. At this point, molten melt pool can be rather weak and thus susceptible to the cracking under tensile stresses. In simple terms, solidification cracking occurs inside molten melt pool or in fusion zone [181], when the liquid flowability is limited by the increased viscosity at a lower temperature, and the inter-dendritic liquid flow is obstructed by the solidified dendrite arms. Solidification cracking occurs when the localized tensile stresses developed across the adjoining grains overpower the ultimate tensile strength (UTS) of the completely solidified material at a certain point and temperature [182]. It is found that the effect of solidification cracking on the final clad properties is unaccountable as it commonly occurs at the top deposit surface. Solidification cracking can be eliminated by adopting laser re-melting or by machining. Liquation cracking needs to be carefully monitored as it remains in heat affected zone once it is formed [183].

Liquation cracking initiates from the weaker region, i.e. partially melted zone or at the heat affected zone (HAZ) in pre-layers, propagating through the intergranular region with the further deposition proceeding layer by layer [184]. Liquation cracking is also called as hot

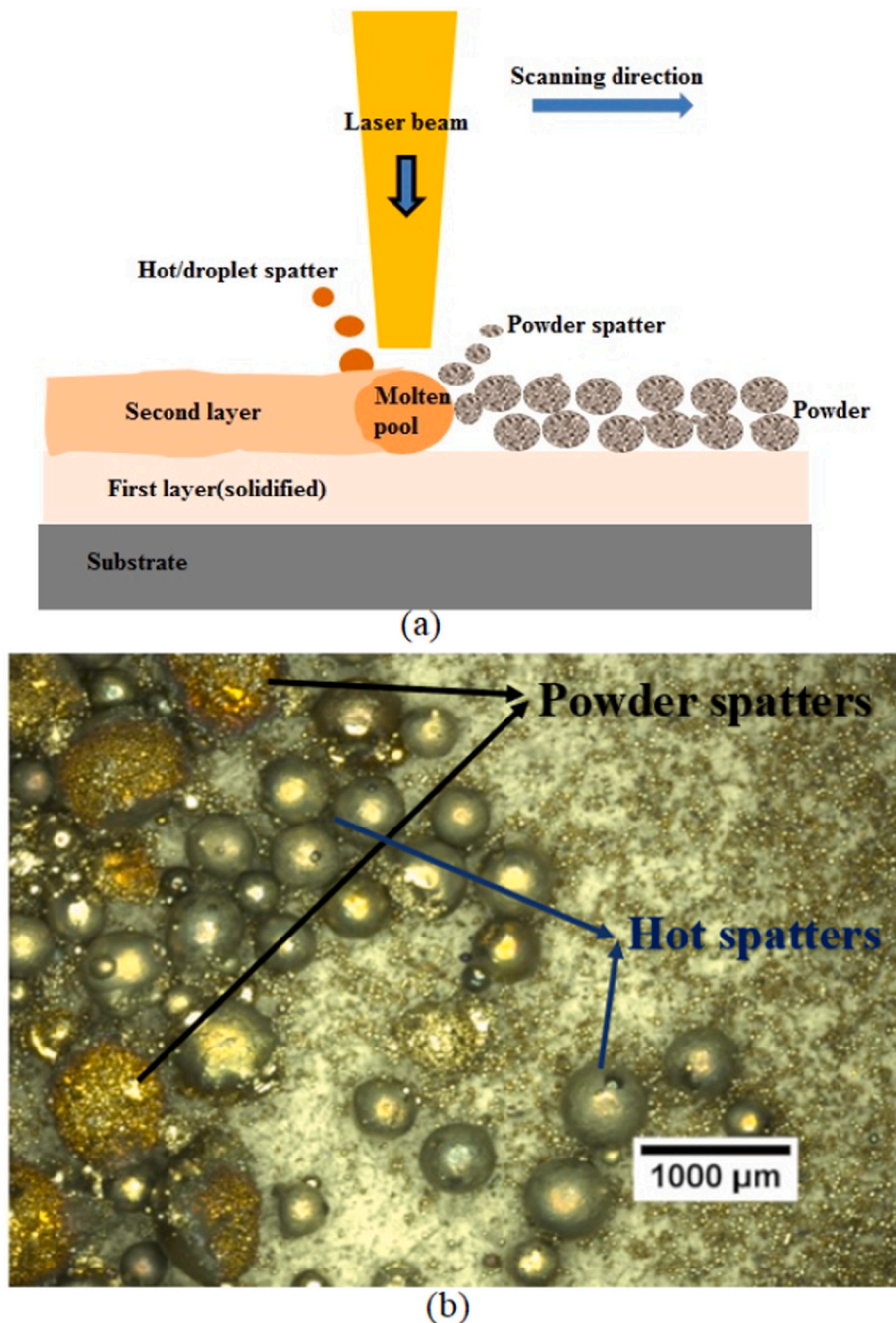


Fig. 17. Schematic illustration of spatters formation (a) hot/droplet spatter and (b) powder spatter [166].

cracking, mostly occur in alloys with high contents of alloying elements. These alloys precipitate several low-melting eutectics in HAZ and intersection regions between the layers that are re-melted above the eutectic temperature (solidus temperature) [130]. Once a liquation crack is formed, it becomes an initiation site for the crack propagation and crack gradually expands as the deposition progresses. Liquation cracking tendency depends greatly on the grain boundary misorientation, that is influenced by the stability of liquation films and local stress concentration [184].

Ductility-dip-cracking (DDC) is a key mechanism of crack initiation/formation in the presence of high angle grain boundaries in LPBF process. It occurs at a modest temperature where ductility and tensile properties are relatively low [185]. Due to lack of diffusion in a non-equilibrium rapid solidification process, the solidus and liquidus temperatures decrease, and the temperature range of solidification becomes

wider initiating DDC in LPBF process [186].

The faster melting and solidifying rates in LPBF process results in tensile residual stresses because the localized high laser energy input, coupled with the lower thermal conductivity of the powder particles [136]. A higher temperature gradient is developed right next to the laser spot. Comparing austenitic SS and low-carbon steels, the former is more susceptible to solidification cracking than the later one because of their lower thermal conduction and higher thermal expansion coefficients. Furthermore, some of the alloying impurities, like Sulphur (S), phosphorous (P), and silicon (Si), have a serious impact on cracking in SS materials. The cracking sensitivity can be reduced by decreasing S + P + Si content. It is also interesting to note that a considerable amount of nitrogen value is detrimental to the solidification cracking of stainless steels [187]. The high carbon steels usually composed of a continuous martensite phase, whereas in SS, a continuous phase is often in the form

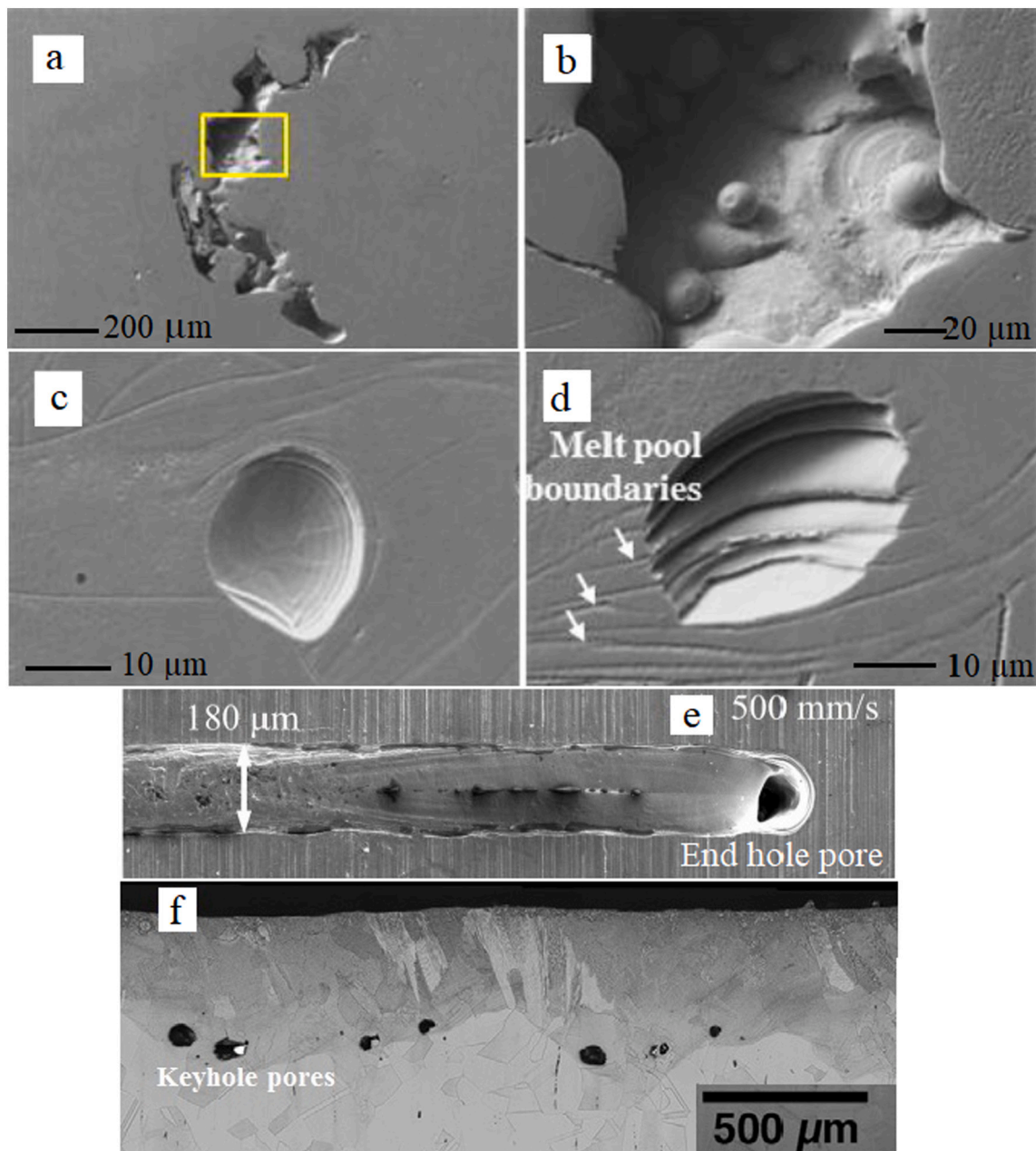


**Fig. 18.** SEM images of porosity defects observed in 316L LPBF samples: (a) low and (b) high magnification of insufficient fusion defect; (c) gas pore; (d) void/cavity defect; [167], (e) end-of track hole [175]. (f) An array keyhole pores at the bottom of melt tracks [169].

of retained austenite, that helps in preventing from cracking. An extreme cracking in M2 (medium-alloyed tungsten molybdenum steel) and H13 tool steels can be prevented by preheating partially or fully. The preheating becomes beneficial to suppress martensite formation. Rapid solidification generally results in the formation of finer microstructure; however, it is not sufficient to curb the segregation. But a low melting phase is sufficiently non-uniform to avoid segregation and cracking. This type of cracking is observed generally in high copper alloy 17-4 PH SS [188]. Similar cracking has also been observed in high silicon steel which was influenced by higher laser energy input [136].

In order to control the thermal stresses and cracking, the following necessary steps can be adapted. Higher heat input results in the formation of higher thermal residual stresses that causes cracking. Hence, the formation of cracks also depends on the selection of optimum range process parameters [182]. The presence of low-melting alloy elements along the grain boundaries can induce severe grain-boundary liquation

cracks. Introducing some alloying elements which tend to limit the solidification temperature range can be beneficial to alter the chemical composition of the molten pool and thereby, preventing from the cracking [189]. Base plate preheating is the new enhancing tool added to LPBF process of steels, that aims to lower the thermal gradients, minimize residual stresses, which in turn results in the fabrication of higher density parts with superior mechanical and physical properties [176,180]. Higher cooling rates are generally avoided as they tend to induce thermal strains and reduce the time available for the liquid metal to fill the cracks [185].

### 3.4. Oxidation

The environment of the LPBF processing chamber is very important to fabricate oxides-free parts. Despite using protective inert environments and a shielding inert gas flow to limit the oxygen content in the

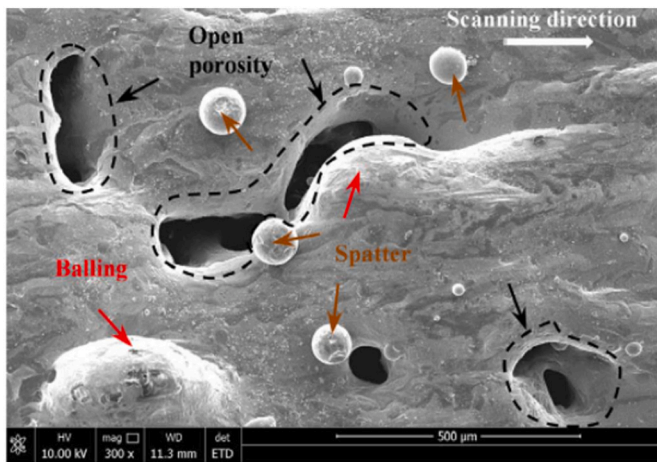


Fig. 19. Scanning electron microscope (SEM) image showing open porosity or voids [173].

working chamber, there is always a chance of small percentage of unwanted oxygen content (~ 0.1–0.2%) present during LPBF process [190]. This is due to the invisible air filling between the powder particles. Similar to the conventional metal casting process, sources of oxides formation in LPBF process arise from oxygen existing in the surrounding atmosphere entrapped inside the porosity of the powder particles. The entrapped oxygen being unable to completely vaporized from the surface caused by the extreme intermix irregular strong laser fluence flow convections of the molten metal pool [190]. Passive oxide films on the powder's surface before the melting can also be formed due to a large area being affiliated with a powder mass [191]. Oxygen content present in the powder could directly be translated into LPBF fabricated specimen

[192].

Ti<sub>3</sub>O<sub>5</sub>, Al<sub>2</sub>O<sub>3</sub>, Cr<sub>2</sub>O<sub>3</sub>, Fe<sub>2</sub>O<sub>3</sub>, NiCr<sub>2</sub>O<sub>4</sub>, NiFe<sub>2</sub>O<sub>4</sub> are the common oxide phases formed during LPBF of maraging steels, stainless steels, and Inconel 718 metal powders respectively [191,193,194]. Generally, alloying elements in steels such as Mn, Si, Ti and Al display higher affinity to oxygen. These elements can be selectively oxidized on the surface of LPBF built part [190]. Maraging steel 18Ni(300), Ti and Al have the highest affinity to oxygen. Oxide phase is generally more stable than the nitride in the steels molten melt pool. A portion of Ti from the maraging steel reacts with the nitrogen to form small cubic TiN particles. TiN is most likely to be formed by higher N<sub>2</sub> supply from the atmosphere (see Fig. 22). In addition, a combined oxide phase containing mainly Ti<sub>3</sub>O<sub>5</sub> and Al<sub>2</sub>O<sub>3</sub> can also be formed. The mechanism of formation of oxides, nitrides, and carbides is similar to other types of steels. The formation of nanometer range oxide films can be easily evaporated during intense stirring action of the molten melt pool by a laser beam, causing negligible damage to LPBF processed parts. On the other hand, micrometer range oxides films (10–100 μm) of irregular geometry formed cannot be completely vaporized by stirring action of the laser beam and Marangoni flow. The oxide layer can grow thicker with increasing oxygen content in the atmosphere, at the same time as the layer re-melting. When re-melting of a new layer begins, the oxide film formed previously breaks down, and part of this oxide hovers on top of the newly formed layer, with the rest trapped inside the LPBF fabricated component. The trapped oxide leads to the formation of oxide inclusion [194]. The oxide inclusions become a site for some partially melted/unmelted powders entrapment. The oxide residues can have a substantial negative impact on heating, melting, and fusion of powder particles, thereby affecting the stability of the molten melt pool [190]. Thick oxide inclusions increases the surface tension effects, limit the absorption of the laser energy and wetting of substrate, obstructs molten pool flow-ability. These oxide inclusions also result in the formation of

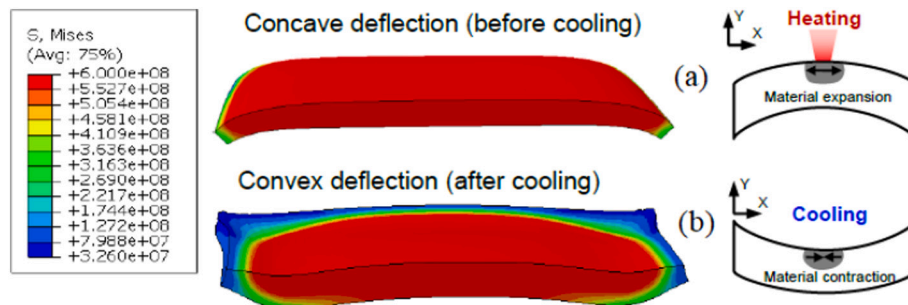


Fig. 20. Schematic of thermal gradient mechanism of residual stress in LPBF: process (a) heating; (b) cooling [84].

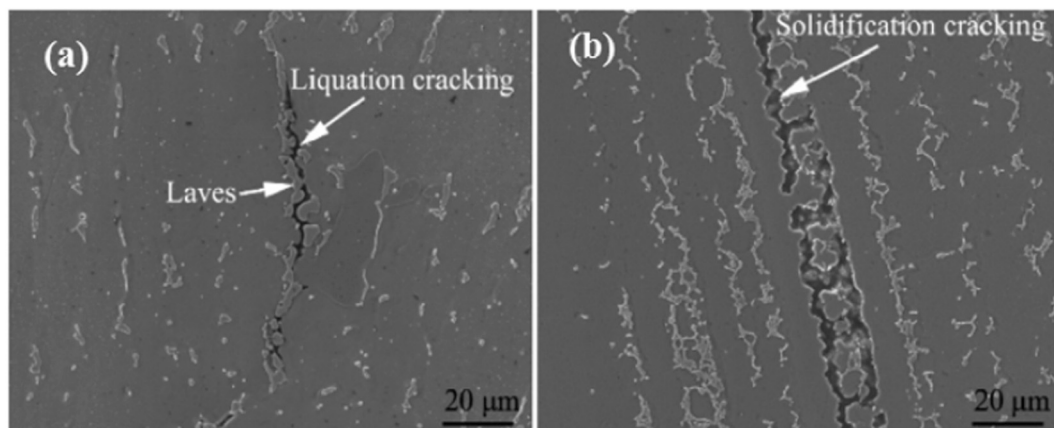
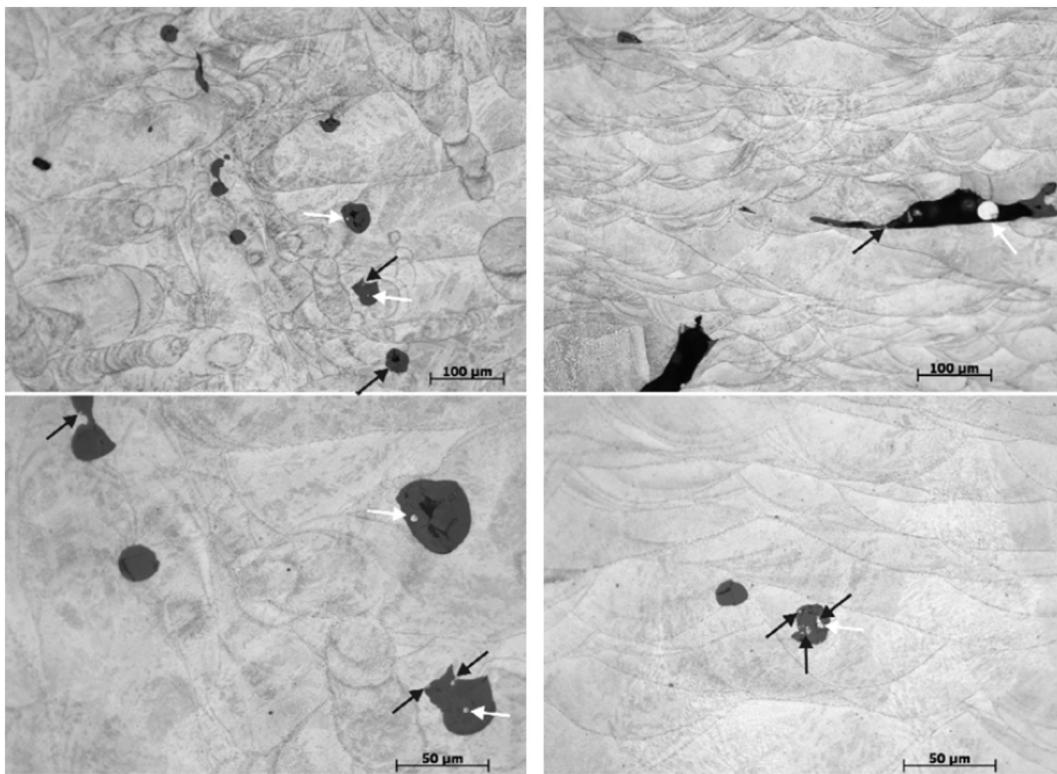


Fig. 21. Morphology of cracking (a) Liquation and (b) solidification cracking [183].



**Fig. 22.** Light optical micrographs at different magnifications of the LPBFed parts built with laser re-melting under technical pure N<sub>2</sub> atmosphere. Top (left) and side views (right) are showing the melt pool shapes and the dark grey oxides containing white parent powder particles (indicated by the white arrows) and yellow TiN inclusions (indicated by the black arrows) [194]. (For interpretation of the references to colour in this figure legend, the reader is referred to the web version of this article.)

metallurgical defects such as balling, insufficient melting between powder particles, reduces the part densification, induces cracking and consequently lowering the mechanical properties [191–193]. It is worth noting that any pickup of moisture from the environment by the feed-stock powders paves way to the introduction of oxygen content into the LPBF system [166].

It is well documented in the existing literature that metal powder characteristics like flowability, tap density, compressibility, grain shape and the size distributions have significant effect on the final quality of LPBF built parts [195,196]. Hoeges et al. investigated the impact of different powder atomization methods on the quality of LPBF processed maraging steel parts [197]. High-pressure water atomization was used to produce maraging steel with niobium instead of titanium. Niobium has a lower affinity to oxygen, which is beneficial in preventing the formation of stable solid oxides/inclusions, and also optimizes the flowability of maraging steels [197]. Formation of oxide inclusions due to the oxide contamination of the powder has been discussed in LPBF process of 17-4 PH steel [198]. The major issues associated with water atomized powder characteristics include irregular particle shape, lower tap densities, and oxidized surfaces. Most of the researchers used gas atomized powders in the literature.

To minimize oxidation, clean and dry powders must be used, despite maintaining sufficiently low oxygen partial pressure. However, the surface oxidation can sometimes become advantageous. An appreciable increase in absorption of CO<sub>2</sub> laser radiation on a surface of oxidized metal powders, compared with normal powders (without oxide growth) which strongly reflected the 10.6 μm radiation [191]. Formation of nanometer scale, continuous and thermodynamically stable oxides films on the surface of 316L, H13, P20 and 18Ni300 steel powders resulted in improved laser absorptivity [199]. Similarly, formation of secondary phase nano oxide particles (oxide dispersion strengthened) during LPBF processing of steels resulted in higher part density, better mechanical

and physical properties [200,201].

### 3.5. Loss of alloying elements

In LPBF process and other laser processing technologies, vaporization is basically intense in a small region right underneath the laser beam where the temperature is high. At a very high laser fluence, the temperature at the surface of the molten melt pool is higher than the boiling point of steels, that contributes to vaporization. Vaporization leads to loss of alloying elements, resulted from the concentration and pressure gradients. The concentration of vaporized alloying elements on molten melt pool surface is higher than that inside the shielding gas [202]. The intensity of vapour pressure at molten melt pool surface is higher than the surrounding environment pressure, thus the surplus pressure drives vapours containing alloying elements to eject away from the surface [202,203]. The vaporization and segregation of alloying elements change the chemical composition of LPBF processed steels. For example, nickel, manganese concentrations were significantly reduced, while the increase in silicon and iron alloying elements concentrations were recorded during LPBF process of Invar 36 steel [158]. Similarly, nickel, manganese and chromium alloy concentrations were decreased with an increase in silicon, molybdenum alloying elements in LPBF process of 316L stainless steels. This phenomena was attributed to the concentrations of alloying elements with lower boiling temperatures decreased, while the concentrations of the other alloying elements with higher boiling temperatures increased, except the base alloying element iron [158].

Loss of alloying elements reduces part density, causes microstructural defects such as keyhole, pores, spatters, voids, cracks, un-melted tracks and exhibit a lower mechanical performance of LPBF fabricated parts [20,158]. Hence, minimizing the loss of alloying elements is considered as an important criterion during the laser parameters

optimization process. Although the laser energy density is a key process parameter, scan speed also plays an equally important role in vaporization. Vaporization of alloying the elements can be minimized by careful selection of laser power and scanning speed.

### 3.6. Denudation

Powder denudation is the apparent depletion of powder particles around the solidified melt track (see Fig. 23). In a typical LPBF processing environment, the denudation is caused by the intense evaporation of the metal vapour plumes from the molten melt pool. The intense vaporization causes the pressure to drop inside the vapour plume and produces an ingoing flow of ambient gas towards the centre of the melt track known as Bernoulli's effect. This inward ambient gas flow is enough to sweep in the powder particles along its flow, which can be included in the molten melt pool or ejected with the vapour plume [204]. Adopting increased laser power, higher scan speed and atmospheric gas pressure (argon gas) results in higher powder particles depletion. On the other hand, denudation also occurs if the laser fluence is not sufficient to completely melt the powder particles, and surface tension tends to pull the partly melted powder particles into the molten pool [100]. Powder denudation leads to porosity and accumulation of un-melted/partially melted particles between the melt track layers causing rough surface [94].

Careful selection of hatch spacing is also important to refrain from linear void structures associated with powder denudation effects [205]. Denudation is critical to process optimization; hence, it is always recommended to identify the suitable process parameters that result in reduced denudation [204,206].

### 3.7. Environmental effects

Argon (Ar), Nitrogen (N<sub>2</sub>), Helium (He) are the three most commonly used protective shield inert gases during LPBF process. In some cases, hydrogen (H<sub>2</sub>) is also used as a deoxidizer to provide required protective environments. LPBF processed steel components produced under Ar and N<sub>2</sub> environments exhibited near full density values, while the parts produced under He environment exhibited density around 90% using

the same processing parameters [207]. The reported lower dense part produced under He environment can be attributed to the shielding gas effect. The higher plasma plumes were generated in He environment above the molten melt pool restricting the laser interaction. He and H<sub>2</sub> environments could block the laser irradiation, resulting in less dense parts due to the transport of low laser fluence. The formation of higher plasma plumes is due to low specific gravity. These plumes can sometimes completely obstruct the laser irradiation causing porosity defects [207]. The lower plasma plumes generated under Ar and N<sub>2</sub> environments maintain good contact between the laser beam and the metal powders, which resulted in near full density parts with the values over 99% [207]. However, it is commonly believed that use of N<sub>2</sub> can react with the alloying elements present in the metal powders, forming unwanted nitrides in the solidified microstructure that tend to display detrimental impact on mechanical properties of LPBF fabricated parts. The difference in the final product densities can be related to the plasma plumes generated, that obstruct the laser beam. This can be combated by using Ar as the shielding gas and supplying the sufficient and continuous energy input, which can overcome the energy losses of metal vaporization and ionization processes [208]. Similarly, employing low atmospheric pressure during LPBF process of steels offers less resistance to metal vapours which causes a large number of free powder spatters (Fig. 24a). Therefore, strong environment pressure is recommended. Metal vapours that exist from the surface of the molten pool have to fight against the strong protective environment, which results in less powder spatters (Fig. 24b) [203].

### 3.8. Common issues associated with LPBF process of steels

In addition to the already discussed different process induced metallurgical defects, there are other most common issues that arise during LPBF fabricating of steels components are as follows:

1. LPBF process of steels commonly result in the formation of anisotropic microstructure along the build direction, especially orientation of defects at the interface of build layers, which affect the elongation and deter the mechanical properties [209].

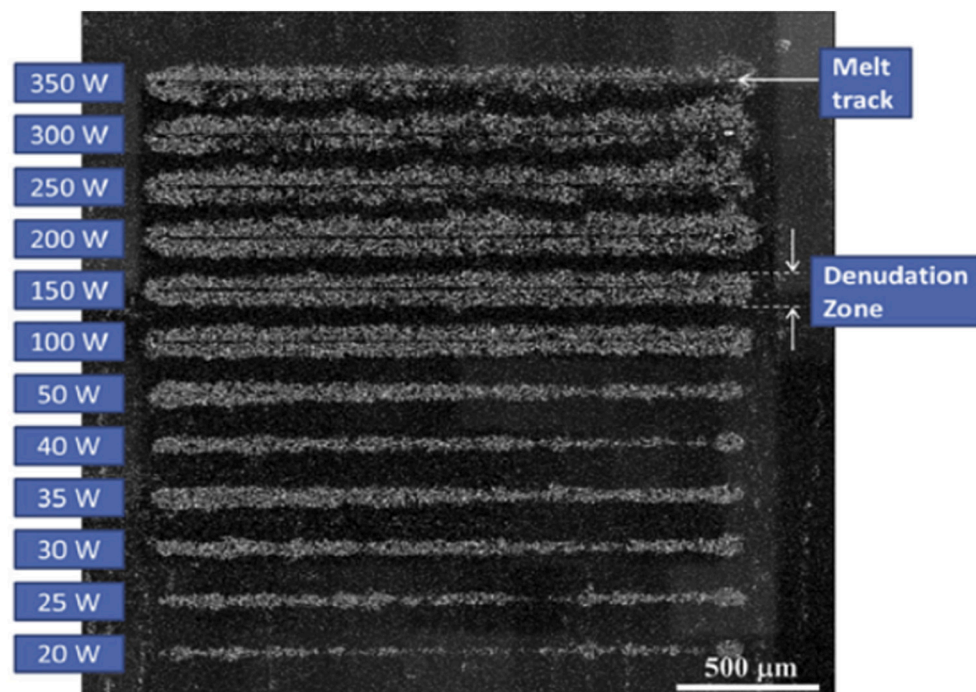


Fig. 23. Confocal height microscope image of denuded zones around melt tracks for different laser power and 2 m/s scan speed [204].

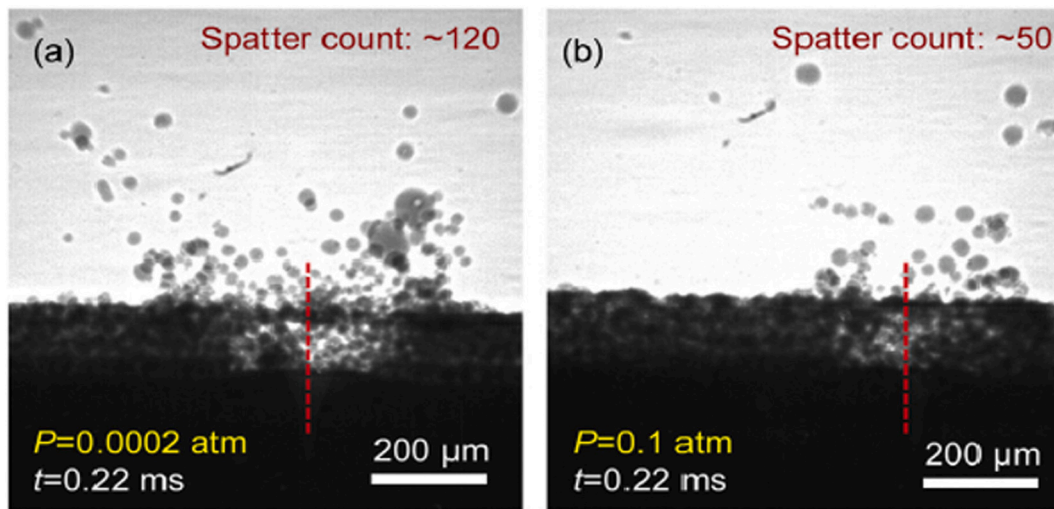


Fig. 24. X-ray images showing spatter counts for the same powder bed thickness with different environment pressure (a) weak environment pressure (b) strong environment pressure [203].

- The chemical composition of the parent steels is going to influence the crack-susceptibility. Low melting alloy elements such as sulphur and phosphorous cause solidification cracking, while manganese can lead to localized depletion, because of its high vapour pressure. Other alloying elements such as silicon, titanium can cause irregular porosities.
- Hard and brittle high-carbon martensite is expected to form during LPBF process of low carbon steels, due to subsequent rapid cooling, which significantly degrades the mechanical properties.
- LPBF processing of high carbon steels is more difficult than lower carbon steels, due to the fact that higher residual stresses are induced during rapid cooling by solidification shrinkage and thermal contraction. In addition to LPBF process induced residual stresses, there is higher possibility of forming undesirable (martensite) microstructure. Combination of martensite and hydrogen promotes hydrogen cracking.
- The higher carbon content promotes higher hardness levels and lower toughness and hence a greater susceptibility to hydrogen cracking in LPBF process of heat treatable low alloy steels.
- The possibility of formation of oxide films and passive carbides on the powder's surface before melting is greater due to the affiliation with powder mass in a large area which affects the surface quality of LPBF fabricated steel parts.
- Formation of large molten melt pool attracts more powder particles that reduces wettability due to presence of oxides and carbides; which favours the formation of defects. In addition, larger melt pool induces higher grains boundaries which becomes a site for liquation cracking.
- Poor flowability of steels powders can block the spreading of powder particles, that affects the continuity of layers thickness and induces surface roughness in LPBF produced part. Exothermic oxidation of steel powders increases the volume of the molten pool leading to a high degree of melt track instability and balling defect.
- In a broader view, it is difficult to produce large components for aerospace, marine, and other industrial applications as the existing LPBF systems are limited to manufacture small and medium size parts due to building chamber size constraint (300 mm × 300 mm × 350 mm).

Based on the existing literature on LPBF of different steels, three LPBF processing windows have been proposed such as the lower processing window, higher processing window and finally the optimum processing window (see Fig. 25). Additionally, impact of the respective

processing windows on the final part quality is outlined. Laser power; 100–200 W, scan speed; 500–1500 mm/s, layer thickness; 40–60 μm and hatch spacing; 75–100 μm, chamber gas pressure at 0.1 atm, oxygen content less than 0.1 vol% are deemed to be optimum processing window parameters, as mostly tend to satisfy all the required constraints (refined microstructure <1 μm, fewer defects, part density >98%, surface roughness <25 μm, hardness >600 HV, yield strength >750 MPa, and tensile strength >550 MPa etc.). Selection of these parameters does not necessarily yield the same results as quoted, concurrently, choosing parameters outside this range could yield excellent results as universality of LPBF machines are not defined. It is believed that this proposed LPBF processing windows gives an overall basic idea (of the role) of most important parameters on the final part quality, and would also act as reference while selecting the appropriate or right combination or the optimized set of process parameters to achieve the superior final part quality.

#### 4. Microstructure, wear and surface texture characteristics, mechanical properties of LPBF processed steels

##### 4.1. Microstructure characteristics

Microstructure evolution during LPBF is not trivial. It is impossible to attribute the microstructure characteristics of a specific type of steel to all other types of steels. However, it is necessary to understand the general aspects of microstructure evolution in LPBF process of steels for further research. Tan et al. studied the microstructure evolution of LPBF process of maraging steels in both horizontal and vertical planes [141,210]. The authors noticed a massive submicron sized hexagonal cellular grains uniformly distributed at the centre, and a needle-shaped elongated grains prevalent at the boundaries of the melting tracks (perpendicular to the scanning direction) [141]. These microstructure characteristics would form in response to the instant melting and rapid solidification at higher cooling rates during LPBF processing of maraging steels (see Fig. 26a). In a horizontal plane, heat input decreases exponentially when the solidification rate ( $R$ ) is increased. This is due to the temperature dependent thermal flux generated by laser fluence would be much higher at the centre of melt track, as compared to the thermal flux at the boundaries as a result of heat dissipation [210]. Owing to the simultaneous action of higher heat dissipation and faster cooling rate, the temperature of liquid metal ( $T_L$ ) at this point reaches well below the melting point ( $T_M$ ) at the centre, and the degree of undercooling ( $\Delta T = T_M - T_L$ ) is sufficiently high enough for the new

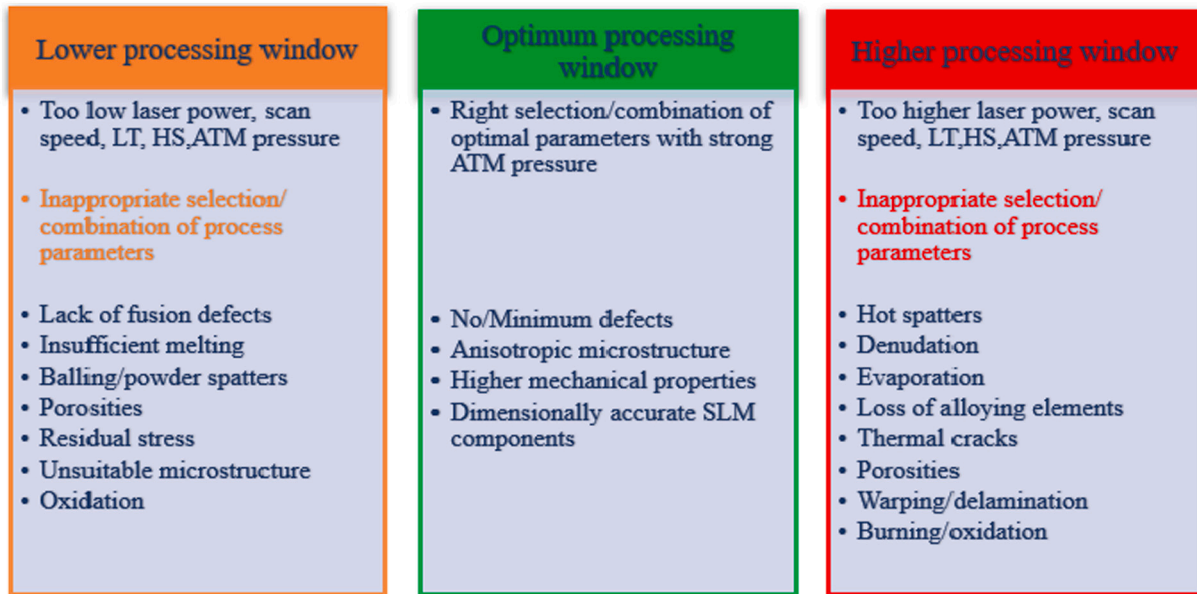


Fig. 25. Label of LPBF processing windows and their effects on final part quality.

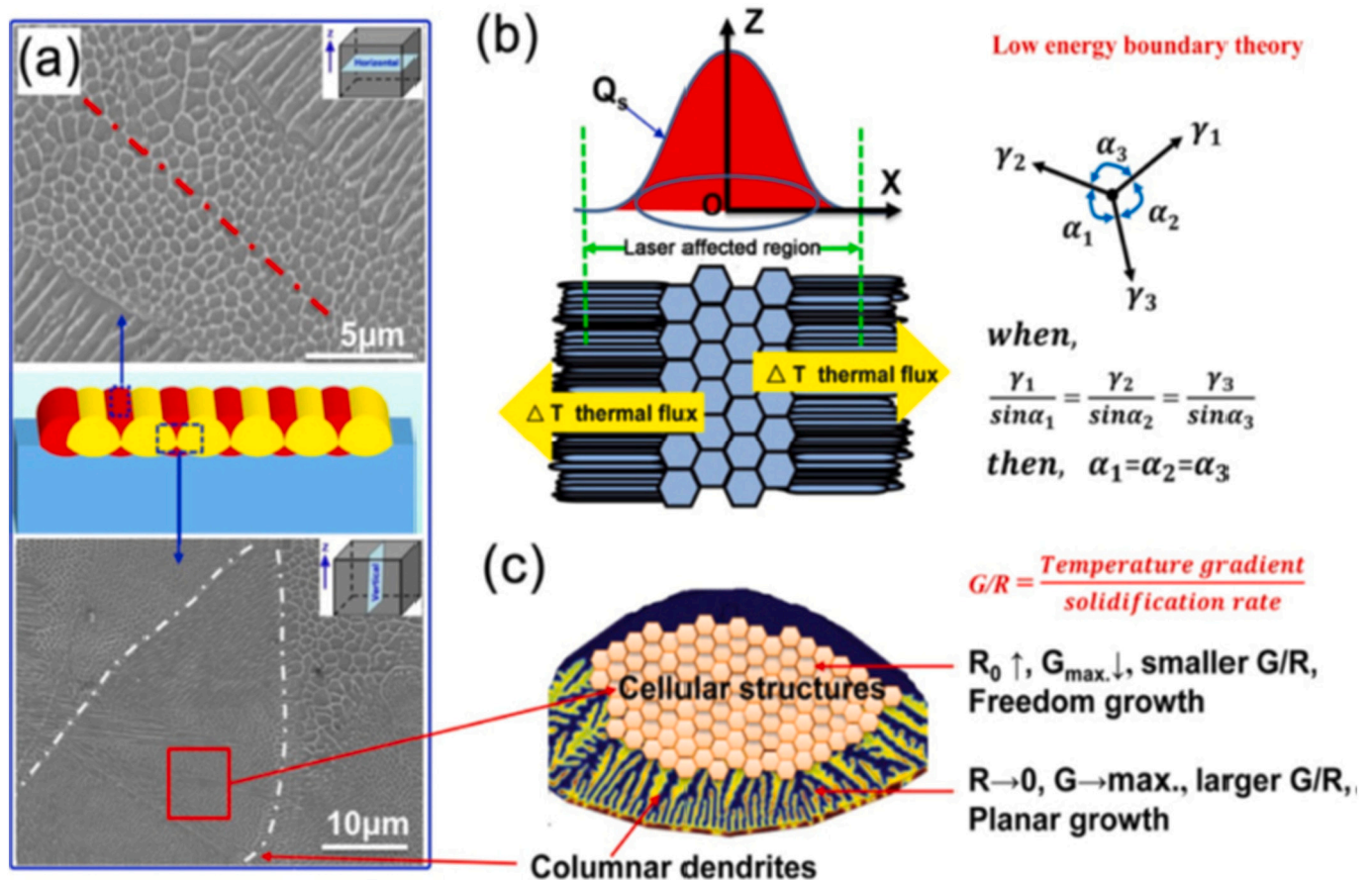


Fig. 26. Microstructural evolutions of LPBF fabricated specimens: (a) the characteristic morphologies of the horizontal and vertical cross-sections; (b) the schematics and formation mechanism of the cellular crystals and elongated acicular crystals; (c) schematics and formation mechanism of the microstructures in the molten pool and overlapped area [210].

grains to nucleate in random orientations [210]. Furthermore, the growth rate of the crystal nucleus is consistent in all directions resulting in easy formation of equiaxial crystal grains. The equiaxial crystals exhibit hexagonal cellular structures as seen in Fig. 26b. The formation

mechanism of various crystals morphologies in a vertical plane is shown in Fig. 26c. Planar solidification structure could be observed at the bottom of the molten melt pool ( $G$  is maximum &  $R \sim 0$ ). As  $G/R$  ratio decreases with the gradual increase in  $R$ , ascending from the bottom of

melt pool in layer stacking/or building direction cellular dendritic structure is visible. A further decrease in G/R value to reach the middle of the molten melt pool, the cellular structure is prevalent followed by a finer/coarser equiaxed crystal that is predominantly evident at the boundaries of the molten metal pool [141,149,210].

Boes et al. reported the heterogeneous dendritic microstructure consisting of low thermal gradients induced fine equiaxed grains, and the elongated dendrites influenced by higher thermal gradients at lower solidification rate [211]. Microstructures of LPBF built 316L steel parts characterized by the columnar grains of austenite with intercellular segregation of Mo, Cr and Si alloying elements, resulted in the formation of non-equilibrium ferrite [140,212]. The occurrence of sub-grain cellular structure (less than 1  $\mu\text{m}$ ) can be mainly related to the micro-segregation of primary elements such as Mo, V and C, due to the Marangoni convection and the difference in temperature between the inside and outside of the molten metal pool [192]. Columnar grains with ferrite content  $\sim 68.8\%$ , and grain orientation is predominantly in  $\langle 001 \rangle$  direction with an average grain length to width ratio of 11.5:1 has been reported during LPBF process of duplex stainless steels [213]. The microstructure of LPBF process of duplex steels was largely composed of ferritic with small traces of austenite and nitrides (presumably Cr<sub>2</sub>N)

nucleating at grain boundaries. It is worth noting that the growth morphology of austenite is along the grain boundaries or of Widmanstatten type [213].

A needle shaped nano precipitate martensites with width  $\sim 200$  nm and 15–50 nm in length were observed at 450–510  $^{\circ}\text{C}$  in LPBF processing of maraging steels [153,210]. A very fine microstructure ( $< 2$   $\mu\text{m}$  or less) mainly consisting of  $\alpha\text{-Fe(M)}$  phase (M, Cr, Ni, Mo) formed during LPBF process of nickel-molybdenum alloy steels [214]. The microstructure of the LPBF built hot work steel characterized by  $\alpha\text{-Fe}$  dendritic cells decorated at the grain boundaries by the carbon rich  $\gamma\text{-Fe}$  regions [215]. LPBF fabricated 316L stainless steels displayed a finer and equiaxed grain, which resulted in superior mechanical properties without compromising ductility [212]. (A schematic illustrating typical microstructure at various length scales formed during LPBF process of 316L SS is shown in Fig. 27a). Wang et al. accredited this combined property to superior nature of the microstructure composed of solidification cells, low & high angle grain boundaries, dislocations, and oxide inclusions [212] (Fig. 27b–h).

LPBF process of austenitic SS are almost extensively restricted to 316L SS and 304L SS. 316L and 304L SS are in a composition range where solidification front is dominated either with a primary ( $\delta$ ) ferritic

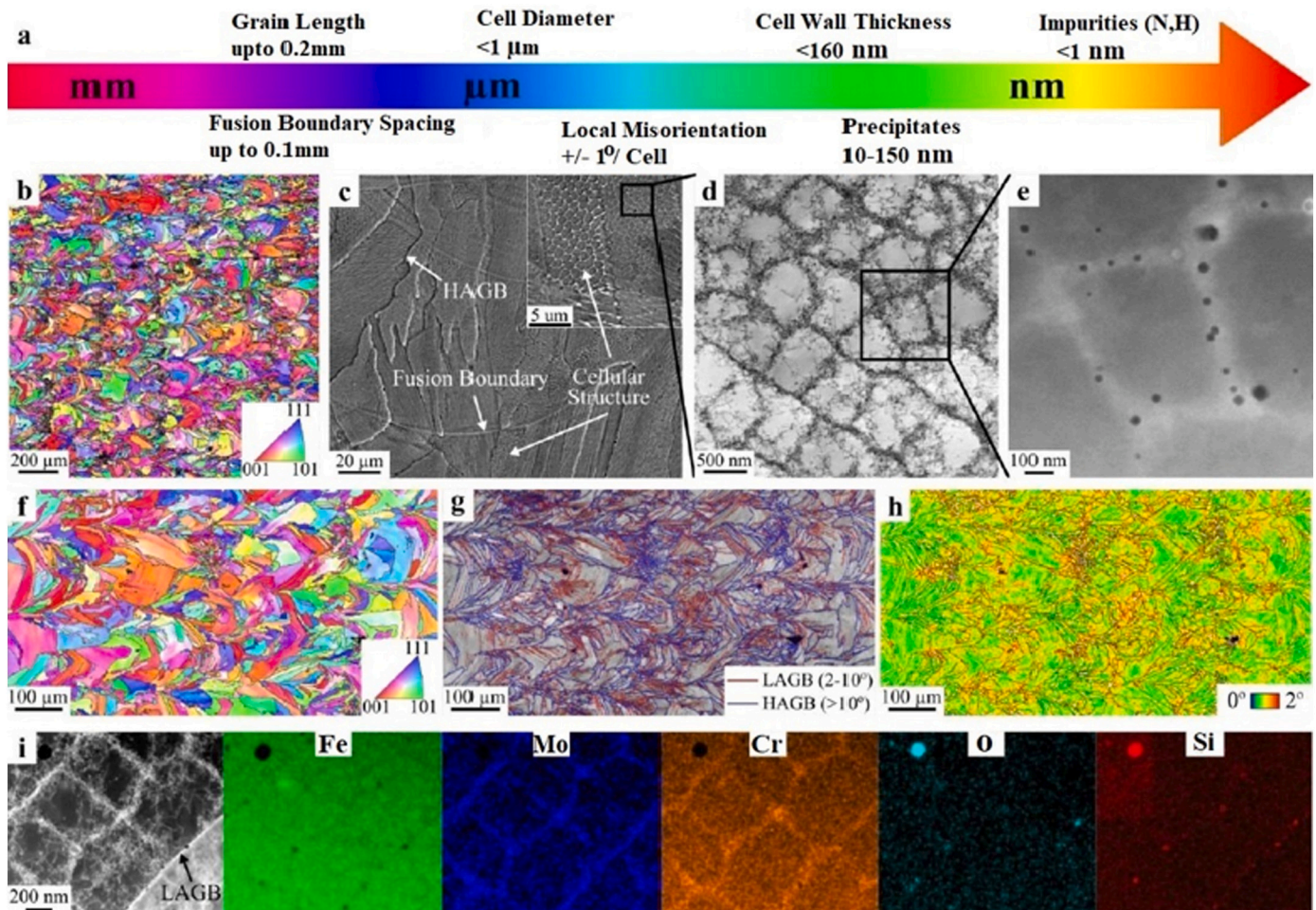


**Fig. 27.** Schematic illustration of typical microstructure of LPBF 316L SS. (a) Label of discovered microstructure at various length scales, (b) an electron backscatter diffraction (EBSD) inverse pole figure (IPF) revealing grain orientations, (c) SEM image showing fusion boundaries, high-angle grain boundaries (HAGBs), and solidification cellular structures, (d) transmission electron microscopy (TEM) image of solidification cells, (e) high-angle annular dark-field (HAADF) scanning TEM image (STEM) of the solidification cells shown in d, (f) EBSD acquired with a 1- $\mu\text{m}$  size (g) EBSD image of superimposed HAGBs and low-angle grain boundaries (LAGBs). Legend representation, HAGBs ( $> 10^{\circ}$ ) coloured in blue and LAGBs ( $2\text{--}10^{\circ}$ ) coloured in red. Fraction of HAGBs and LAGBs are  $\sim 59\%$  and  $\sim 41\%$ , (h) Kernel average misorientation (KAM) map to demonstrate local misorientation across individual grain, (i) HAADF STEM image showing segregation of Mo and Cr alloying elements in to the solidified cellular structure and low angle grain boundaries, while EDS confirms the corresponding Fe, Mo, and Cr this segregation. EDS map also confirms that these particles are predominantly rich with Si, O, and Mn [212]. (For interpretation of the references to colour in this figure legend, the reader is referred to the web version of this article.)

phase or with a primary austenitic ( $\gamma$ ) phase. LPBF processing of stainless steels exhibits fully refined austenitic microstructure, with the columnar solidification grains  $\sim 1 \mu\text{m}$  diameters or less [5,162,216–218]. The number of solidified columnar grains may vary from tens and/or hundreds that are very similar to the crystal orientation, collectively form a single austenite grain i.e. a material volume responsible for high angle grain boundaries (Fig. 27b & c) The grains formed in as-built LPBF SS samples are finer than those of conventional processes [180,184,216–218]. LPBF process of this type of steels is fully austenitic and there is no conclusive evidence of any solid-state phase transformations [180,216,219–221]. The intercellular regions shows an enrichment with Cr and Mo, which are, however, not sufficient to stabilize the ferrite [218,212] (Fig. 27i). A strong fibre texture with  $\langle 001 \rangle$  crystallographic direction aligned along the build direction (i.e. against fast heat dissipation direction) was revealed during LPBF process of steels [180,221]. The strong texture is caused by the  $\langle 001 \rangle$  crystallographic direction, as it is the fastest growing direction in the solidification of cubic metals, and hence dendrites or cells grow aligned with the temperature gradient [222].

Z. Sun et al. employed a modified laser scan strategy by adopting relatively high laser power with smaller hatch spacing to improve the mechanical properties of LPBF processed 316L SS [223]. This modified approach lead to the formation of new  $\langle 110 \rangle$  crystallographic texture along the build direction instead of a regular  $\langle 001 \rangle$  texture. The modified  $\langle 110 \rangle$  crystallographic grain orientation favours twinning effect under deformation, as a result of this the material experiences higher strain hardening rates which profits in achieving superior mechanical properties (ductility and UTS) [223]. H. Sun et al. moved a step forward to show that it is possible to regulate crystallographic texture by carefully controlling the process parameters during LPBF processing of 316L steel. They reported crystallographic lamellar microstructure  $\langle 100 \rangle$  and  $\langle 110 \rangle$  oriented grains along the build direction [224]. As already mentioned texture control could be a reliable tool to control anisotropic microstructure in yield and tensile strength [225]. However, the strain hardening behavior is predominantly dependent on grain morphology, resulting in anisotropy in ductility despite the reduced crystallographic texture [225]. LPBF process of maraging steels displayed different solidification microstructure with cellular/dendritic sizes  $\sim 0.3\text{--}2 \mu\text{m}$  as compared to conventional built maraging steels [226,227]. The cellular structure in LPBF processing of maraging steels is a result of micro-segregation during solidification which enriches some of the alloying elements in the inter-dendritic regions. The microstructure of LPBF produced H13 tool steel consists of solidification cells/dendrites with retained austenite located in the inter-dendritic regions. The observed size of the cells/dendrites was in the range of  $0.5 \mu\text{m}\text{--}2 \mu\text{m}$ . It is worth noting that there is only limited information available in the literature regarding the crystallographic texture of H13 tool steels and maraging steels. This could be probably related to the very weak crystallographic texture [228].

As-built LPBF processed 17-4 PH steel displayed a high fraction of austenite phase or even fully austenitic microstructure. Facchini et al. reported LPBF of 17-4 PH stainless steel contained 72% austenite and 28% martensite [229]. In addition, the presence of little traces of Nb-rich carbides was unsure [188]. TEM investigations confirmed the presence of retained austenite between martensite discs. LPBF process of 17-4 PH steels (including austenitic, martensitic and ferritic steels) usually display strong crystallographic grain orientation in  $\langle 001 \rangle$  direction aligned along the building direction (z-axis) [230,231].

LPBF process of (TWIP/TRIP steels) high-manganese steel was investigated by [232], the microstructure consisted of mainly austenite, together with  $\alpha$ - and  $\epsilon$ -martensite, along the small quantity of Mn segregation was observed as compared to cast ( $X_{30}\text{Mn}_{22}$ ) steels [232].

LPBF synthesized mechanically-alloyed (ODS steels) PM2000 steels revealed that a homogeneous distribution of retained oxides. However, the average sizes of these retained oxides were in the range of  $48 \text{ nm}\text{--}61 \text{ nm}$ , which are significantly coarser than the conventionally-produced

PM2000 steels ( $30 \text{ nm}$ ) [233]. Similar microstructure wholly ferritic in nature was reported during LPBF built mechanically alloyed PM2000 or MA956 steels [234–236]. The fully ferritic microstructure exhibited strong fibre texture with the  $\langle 001 \rangle$  direction parallel to the build direction. The ferritic microstructure revealed a homogeneous distribution of both finer and coarser oxides [234]. The presence of both finer and coarser oxides could be attributed to agglomeration of nanometer-sized oxides [236]. The strong crystallographic texture results in anisotropic mechanical performance of LPBF processed ODS steels [234]. The crystal structure of the oxides is sometimes represented by  $\text{Y}_2\text{Ti}_2\text{O}_7$  or  $\text{Y}_4\text{Al}_2\text{O}_9$  [219]. LPBF fabrication of Fe-14Cr-1W powder mechanically alloyed with  $\text{Y}_2\text{O}_3$ , and  $\text{TiH}_2$  reported a similar microstructure to the one described above for LPBF process of PM2000 [201].

#### 4.2. Wear and surface texture characteristics

As a result of complex thermophysical mechanism LPBF process undergoes, rougher surface finish is induced. Defects and surface asperities like thermal cracks, spatters, un-melted/partially-melted, ripple effect, staircase effect, surface and sub-surface porosities, re-entrant features emerge on LPBF parts surface which are responsible for causing the unfavorable surface finish or surface texture [155]. A thorough investigation of currently available literature on wear and the surface texture characteristics of LPBF process of steels reveal that the research is still in its early stages. Presently it is hard to relate the wear and surface texture characteristics of LPBF processed parts to the real applications. However, to expand LPBF applications into frictional pairs, it is paramount to study the wear performance of LPBF process of steels under various contact conditions [154]. Wear is defined as the loss or displacement of material from a contacting surface. The wear rate of LPBF processed steels linearly depends on the volume percentage of the porosity. Reported wear rate was 6–17% higher than bulk steels for less dense LPBF process of steels with the presence of porosities (see Fig. 28). It is indeed possible to achieve equivalent or superior wear resistance than conventional steels if LPBF built steel components are fully dense with minimum numbers of surface defects [237]. Similarly, the higher hardness, perfectly dense, plus good wear resistance could be accomplished when LPBF processed parts exhibit least surface asperities [238,239]. The principal wear phenomena act as a site for crack initiation and crack growth, originating from the pre-existed surface defects that subsequently leads to the premature failure of the component at lower applied loads [239].

Surface texture at this stage is generally used to study the basic capabilities of LPBF processes, an application to specific requirements is not completely introduced. Nevertheless, surface roughness plays a key role in determining the mechanical, tribological and functional properties of LPBF processed steel components. Surface texture is defined as the geometrical irregularities exist on the surface, excluding the geometrical imperfections that contribute to the form or shape of the surface [240]. LPBF built surfaces containing surface asperities and other particles features are often characterized by using 3D optical profilometers and X-ray computer tomography (XCT), allowing the captured data to be used for 3D surface texture characterization. Narasimharaju et al. more recently investigated the impact of various build surface inclinations with respect to 3D surface texture parameters [155]. It was found that varying surface inclination combined with staircase effect and un-melted/partially melted particles exhibit a strong correlation. Staircase effect was evident between  $3$  and  $45^\circ$ ; above  $45^\circ$  the staircase surface was supplanted by un-meted/partially melted particles at  $90^\circ$  [155]. Similar kind of research was carried out by Gogolewski et al., apart from investigating multiscale analysis of surface texture quality of models for LPBF built steel [241]. Horizontal built LPBF components are governed by balling, ripple effect, spatters, while staircase (stair-steps) effect, un-melted/partially melted particles are linked with the curved or inclined surface of LPBF processed parts (see Fig. 29a & b). Staircase effect could be minimized by adaptively

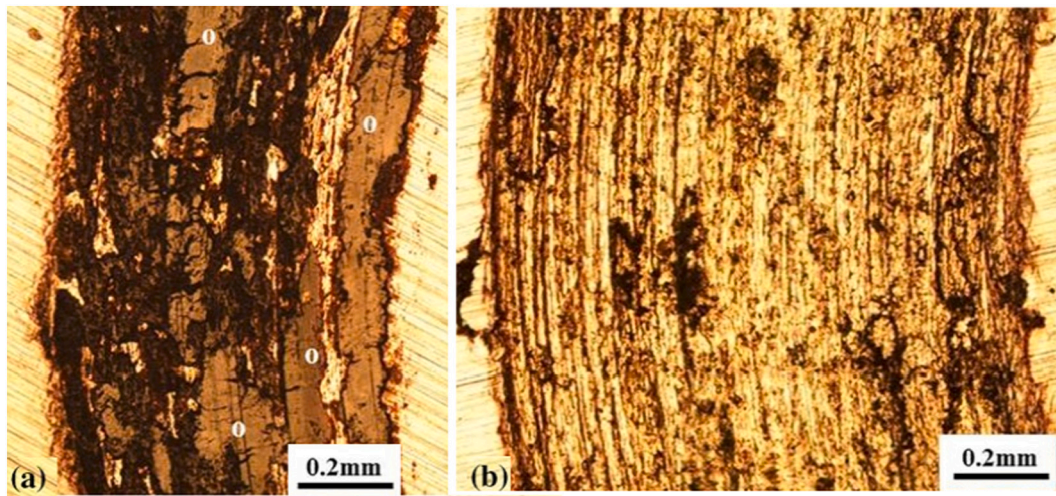


**Fig. 28.** Comparison of wear rate in dry wear test condition at 120 rpm, 10 N (a) bulk 316L and (b) LPBF 316L (175 mm/s, 150 W) samples. “O” marks in (a) indicate tribo-oxide film [238].

reducing the layer thickness between the melt track layers [80,242]. Lou et al. successfully examined the novel material ratio (Mr) curve as an effective analysis tool to differentiate two AM (LPBF process, high speed sintering) surface topographies, and allowing surface texture to be linked with process control and functional performance [243]. The recesses of 3D Mr curves are caused by re-entrant features (surface pores). Authors identified Vvv (valley void volume) parameter determined by the Mr2 ratio to characterize (height position) the open surface pore [243].

Lower energy density gives rise to shattered, rough and scattered porous worn surface with cracks due to insufficient fusion of powders. Similarly, excessive energy density leads to ejection of hot spatters and redepositing on the LPBF processed part surface resulting in higher surface roughness. Wear resistance and surface finish can be improved by selecting the optimized LPBF process parameters including smaller layer thickness, in addition to adopting laser re-melting, and suitable post-processing methods [244]. Partially melted powder particles on the interior surfaces can be eliminated while the surface finish and texture could be substantially improved (at least 45% Ra value) by employing chemical-abrasive flow polishing techniques [245]. Additionally, reinforcement of tungsten carbides during LPBF process of maraging steel resulted in the formation of a thin carbide layer that significantly reduced the wear rate by >1500 times [246].

#### 4.3. Mechanical properties of LPBF fabricated steels

##### 4.3.1. Hardness and tensile properties

The present studies on mechanical properties of LPBF process of steels are mostly concentrated on evaluating hardness, tensile

performance and fatigue properties. Tensile and hardness properties are summarized in Table 2. Schematic overview of basic mechanical properties of most common steels used in LPBF processes and conventional processes is shown in Fig. 30. This figure intends to provide a broad overview of the results reported in the literature but does not holds good for all classes/cases of steels, and sometimes considerable dependence of the material properties on LPBF processing conditions.

From the existing literature, average Vickers hardness values for LPBF processed steels range from 408 to 900 HV, which is certainly higher than wrought materials [26,213]. Residual stresses are sometimes tend to benefit the LPBF fabrication of steels. They can also improve the hardness values of a LPBF component if at a reasonable level [247]. The increase in hardness values also improves the wear resistance of LPBF built parts [248]. The refined microstructure of LPBF processed tool steel samples consisted of low martensite phase, and high content of fine carbides and the alloying elements (V, Mo, C), that are much more homogeneously dispersed in the material as compared to the as-cast state which resulted in higher hardness values [26]. The microstructure of LPBF built samples determines the mechanical properties and the difference in tensile properties along various directions is mainly due to the easy introduction of metallurgical defects into the bonding area between two adjacent melt track layers. The tensile properties of the LPBF fabricated samples along the vertical direction are inferior, as compared to those samples built in the horizontal direction [165]. In order to obtain the higher tensile properties, besides the position of the sample in the horizontal direction, the laser fluence also plays an equally important role.

For a low laser fluence ( $104.17 \text{ J/mm}^3$ ), unsurprisingly, resulted in higher porosities (lack of fusion holes or crater like voids). The porosities

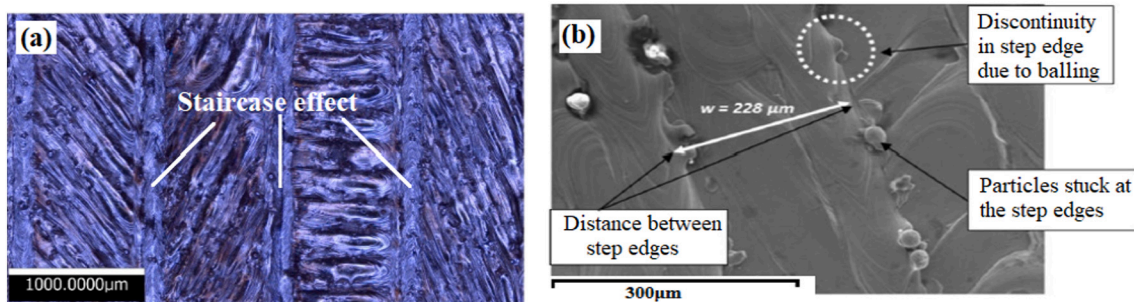


**Fig. 29.** (a) Alicona G4 image showing staircase effect [155], (b) SEM image of inclined surface illustrating un-melted/partially melted powders stuck at the step edges [242].

**Table 2**  
Hardness and tensile properties of LPBF of steels from different literatures.

Materials	Condition	Hardness (HV)	Yield strength (YS)	Ultimate tensile strength (UTS)	Elongation (%)	Reference
Maraging steel (MS)	LPBF	–	~915	~1165	~12.44	[210]
	LPBF aged	–	~1967	~2014	~3.28	[210]
	LPBF solution	–	~962	~1025	~14.40	[210]
	LPBF solution aged	–	~1882	~1943	~5.60	[210]
316L stainless steel (SS)	LPBF	–	455	579	~50	[25]
FeCrMoVC tool steel	LPBF	~900	–	–	–	[26]
316L SS	LPBF $\Psi = 0$	–	~494	~640	~56.7	[27]
	LPBF $\Psi = 45$	–	~498	~606	~59.9	[27]
	LPBF $\Psi = 60$	–	~536	~601	~62.7	[27]
	LPBF $\Psi = 90$	–	~489	~548	~43.7	[27]
316L SS	LPBF	~281	–	~590	~21.1	[170]
	LPBF single	–	~346	~921	~69.9	[22]
Austenitic SS	LPBF CLM	–	~387	~924	~67.5	[22]
	LPBF low power	~241	~500	~625	~47	[268]
ASTM A131 steel	LPBF 250 mm/s	–	~938	~1037	~4.5	[171]
	LPBF 300 mm/s	~241	~850	~1050	~4.75	[171]
316L SS	LPBF	–	~1100	~1200	~20	[21]
316L SS	LPBF	–	~517	~633	~74	[23]
304L SS	LPBF	–	~485	~712	~61	[24]
Invar 36	LPBF	–	~350	~400	~64	[20]
316L SS	LPBF heat treated (HT)	–	~550	~620	~90	[20]
17-4 PH SS	LPBF opt parameters	~355	~650	~940	~4	[269]
17-4 PH SS	LPBF	~395	~750	~950	~3.6	[269]
17-4 PH SS	LPBF	~475	~940	~1150	~2.8	[269]
Maraging steel	LPBF	–	~750	~1200	~17	[270]
MS-10%WC	LPBF	–	~650	~1000	~7.5	[270]
17-4 PH GA	LPBF 60 $\mu$ s time	–	~1116	~1358	~5.1	[271]
17-4 PH WA	LPBF 80 $\mu$ s time	–	~500	~990	~3.3	[271]
316L SS	LPBF	~202	–	~750	–	[272]
316L SS	LPBF HT @ 650C 2 h	~210	–	~700	–	[272]
	LPBF	~209	–	–	–	[273]
	LPBF HT	~215	–	–	–	[273]
CLAM steel	LPBF HT HIP	–	–	~966	~5	[274]
	LPBF	–	–	~757	~9	[274]
316L SS	LPBF 573 K	–	–	~694	~18	[274]
	LPBF 873 K	–	~550	~1016	–	[275]
	LPBF 1273 K	–	~459	~969	–	[275]
	LPBF 1673 K	–	~440	~941	–	[275]
	LPBF/plain carbon steel substrate	–	~347	~836	–	[275]
Maraging steel	LPBF/MS substrate	–	~174	~712	–	[275]
	LPBF/H13 substrate	~450	–	~2100	~15	[90]
		~286	–	~1200	~13	[90]
	~608	–	~1180	~11	[90]	

act as the main sites for crack initiation triggering brittle fracture with limited plastic deformation, causing cracks propagation under tensile loading conditions (see Fig. 31a). It was reported that using optimized energy density (125 J/mm<sup>3</sup>, 156.25 J/mm<sup>3</sup>) the part density reached to its maximum, and the obtained microstructure displayed decent refined dimples with numerous grain boundaries that would block dislocations movements causing the material to resist deformation resulting in higher yield strength and tensile strength (see Fig. 31b & c) [170]. It is worth noting that LPBF fabricated steels are strengthened without losing their ductility, unlike work-hardening that improves the tensile strength by sacrificing ductility. Adapting excess energy density (178.57 J/mm<sup>3</sup>) resulted in decreased toughness due to high degree of overheating of the molten melt pool, causing larger and shallow dimples with lower resistance to dislocations (see Fig. 31d) [170,249].

As a result of finer microstructural texture, the mechanical properties of the LPBF manufactured steels have been improved. In addition, refined microstructure provides higher resistance to the dislocation motions and other mechanisms of plastic deformation, such as sliding [167]. Owing to the high density of low-angle grain boundaries, and the fine cellular microstructures associated with LPBF processing, the yield strength (YS) of 316L stainless steel is greatly improved [19]. The unique development of crystallographic lamellar microstructure (CLM) via strengthening of LPBF built 316L steel resulted in higher YS, ultimate tensile strength (UTS), and significantly higher ductility [22]. The grain refinement of the nano-cellular structures, presence of nano-size

carbides along with the negative residual stress resulted in superior YS, UTS and higher ductility [20] in LPBF fabricated steels in comparison with other conventional manufacturing like standard casting, extrusion (wrought) and laser engineered net shape processes [23,24]. Similar higher yield strength and better ultimate tensile strength and compressive strength (CS) [YS = 455–640 MPa, UTS = 579–2100 MPa, CS = 3796 MPa] have been achieved in LPBF fabricated steels [26,27,249]. In some cases, higher elongation [24,25], and higher toughness are reported, the reason for this is attributed to the stress induced austenite-to-martensite transformation [28,58].

It is well acknowledged that LPBF processed stainless steels often display superior YS and UTS [180,212,217,218,225,250–252] as compared to conventionally manufactured steels. The reported YS values and UTS values from the literature show high variability and are in the range between 350 and 600 MPa, and 480–800 MPa respectively. Typical YS and UTS values for conventionally processed stainless steels lie in the range of 230–290 MPa and 580–590 MPa [253]. Additionally, LPBF processed steels display a higher yield to tensile strength ratio [180,217,250,252]. However, some of the researchers reported lower fracture toughness and elongation to fracture; as low as 12% for LPBF built stainless steels as compared to the wrought material typically; 40–50% [217,254]. Majority of the studies reported a higher elongation to failure and fracture toughness up to 67% [180,212,218,225,252,255]. The higher yield strength and tensile strength have been related to the finer microstructure and dislocation

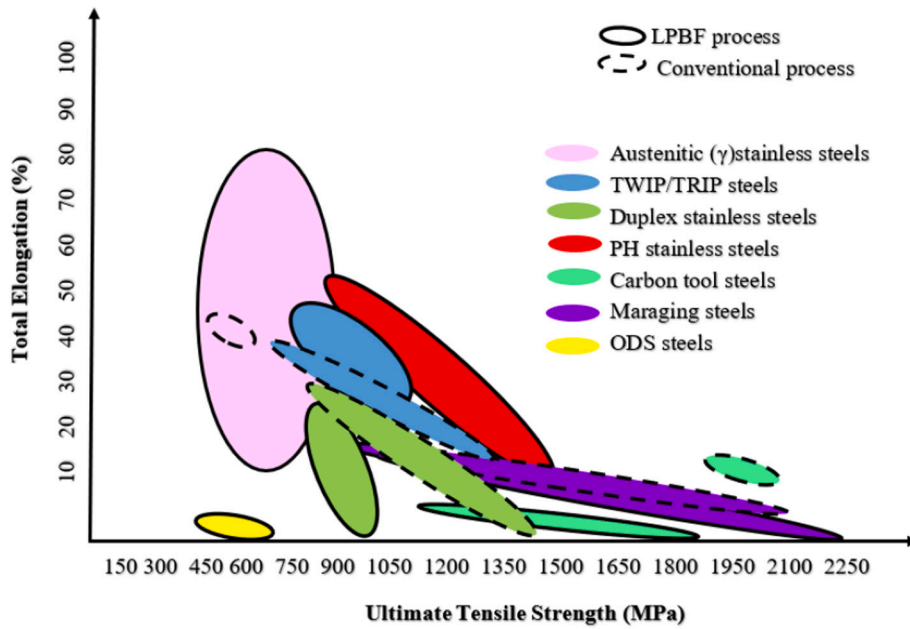


Fig. 30. Schematic illustration of basic mechanical properties of commonly processed steels in LPBF process and conventional process. Steels type is indicated by the field colour, whereas the field border represent the process type. (TWIP/TRIP stands for twinning/transformation-induced plasticity, PH-precipitation-hardening and ODS-oxide dispersion-strengthened).

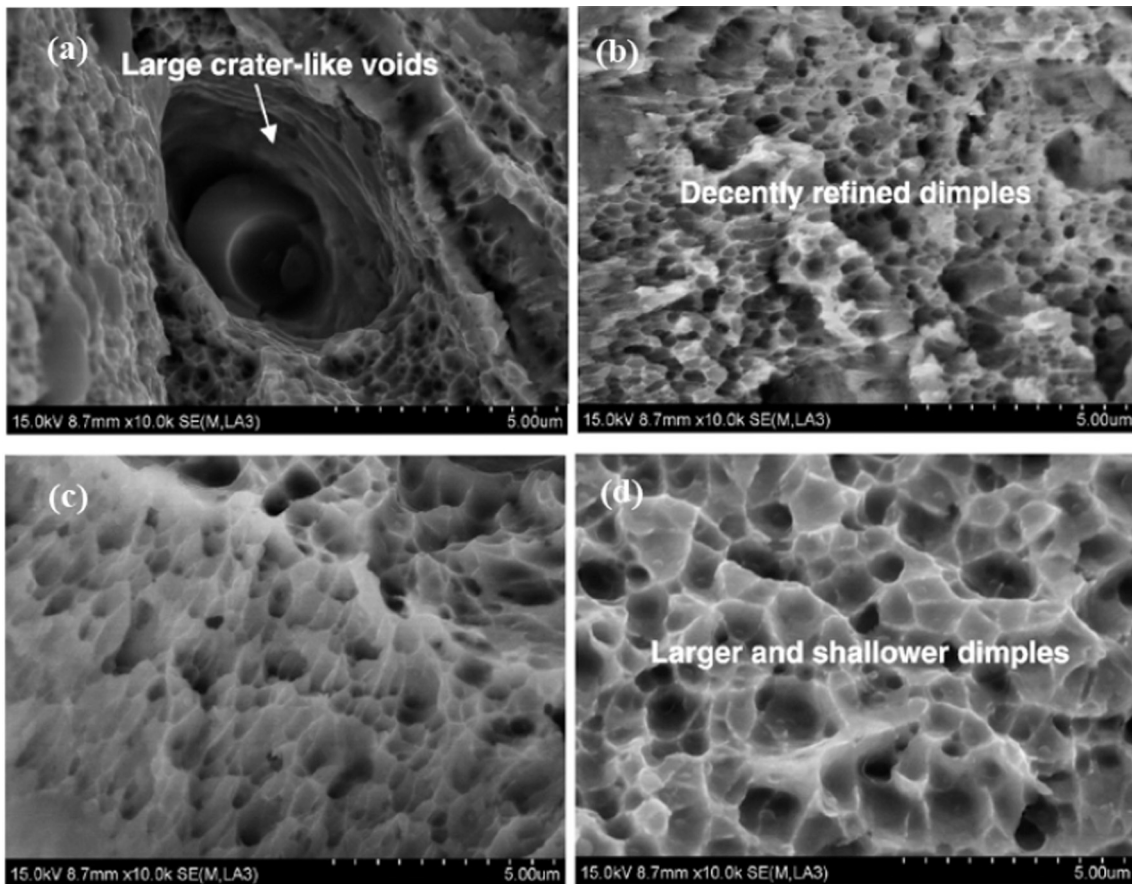


Fig. 31. Typical SEM images taken from the tensile fracture surfaces of LPBF-processed 316L specimens at different laser energy densities of (a) 104.17 J/mm<sup>3</sup>, (b) 125.00 J/mm<sup>3</sup>, (c) 156.25 J/mm<sup>3</sup> and (d) 178.57 J/mm<sup>3</sup> [170].

substructure as per Hall-Petch relation [212,218,225,251]. Also, in LPBF built steel components, the defects in the microstructure (brittle phases/inclusions, porosity) have a strong negative impact on the elongation to fracture.

LPBF fabricated duplex SS 2507 resulted in much higher YS and UTS, along with a moderate elongation at fracture (~8%), and a ductile fracture mode compared to conventionally produced ones. The higher mechanical strength and average ductility of LPBF built sample was the result of exclusive ferritic microstructure [256].

TRIP/TWIP steels (unlike austenitic stainless steels) are considered fully austenitic metastable steels which display transformation-induced-plasticity (TRIP) or twinning-induced-plastic deformation (TWIP). Haase et al. studied LPBF process of high-manganese steel (X30Mn22) [232]. From their study it was revealed that TRIP/TWIP effect was certainly functional when subjected to tensile deformation of the material, and also described its anisotropy arising from the strong (LPBF-typical) fibre texture. The tested YS and UTS were found to be higher in all the directions as compared to cast and rolled standard steels (302–416 MPa vs. 275 MPa and 906–1065 MPa vs. 894 MPa, respectively), but the elongation at fracture was lower (24–31% vs. 52%). These type of steels offer high work hardening ability which makes them attractive for applications where high energy absorption, high strain hardening rates, and high ductility are required [232].

Owing to the presence of martensite and austenite in different proportions in 17–4 PH steel microstructure, hardness and mechanical properties of LPBF processed 17-4 PH steel dispersed over a wide range of values. It is worth noting that lower mechanical properties were not only due to the presence of softer austenite phase but also due to the precipitation reaction that takes place in martensite during ageing [32,257,258]. Overall LPBF process of 17-PH steels are typically softer and less strong than wrought and age hardened materials [259].

In general, the mechanical properties of LPBF maraging steel are comparable to conventionally produced steel materials, but not entirely identical. LPBF produced maraging steels displays equal or slightly better YS and UTS as compared to conventional ones despite the finer microstructure resulting from LPBF process [77,210,260,261].

Hardness values recorded for LPBF produced H-13 tool steels range from 570 HV–680 HV, (and marginally higher 745 HV when measured in the skin area [262]) [192,263,264]. These values are close to or even superior than as-quenched wrought H13 steels, contemplating the fully-martensitic state. Many of the recorded YS and UTS values for LPBF processed maraging steel samples are significantly lower because of the extreme brittleness of this state which leads to the premature failure of tensile test specimens [68,262,264–266].

The strong crystallographic texture  $\langle 001 \rangle$  of LPBF processed ODS steels lead to an anisotropic mechanical behavior, i.e., ductile fracture when strained in the build direction, but brittle trans-granular fracture when strained perpendicular to the build direction [234]. Employing additional post process heat treatments, the tensile strength numbers reached somewhat closer/equal to the conventionally produced ODS steels [234]. The difference in mechanical properties of LPBF manufactured steels available in numerous grades depending upon on specific applications is attributed to its wide range of technological parameters, which lead to the formation of anisotropy of cellular dendrite microstructure and some deviation in part densities of steel samples [227,267].

#### 4.3.2. Fatigue properties

LPBF processed steels are exposed to a dynamic loading condition in many functional industrial applications; Hence, a thorough understanding of fatigue behavior and characteristics is requisite to evaluate their fatigue life. However, there is only a limited number of studies available in the literature that are dealing with the fatigue properties of LPBF built steels. The most important parameters that affect the fatigue property of the LPBF processing of steels are surface finish and the building direction [167,249,276]. Furthermore, process parameters

along with fatigue testing conditions also influence the fatigue life of LPBF built steels [277,278]. The fatigue limit of LPBF fabricated part mainly depends on its surface finish. It is commonly believed that fatigue crack initiation starts at the surface of metallic materials. Similar to conventionally manufactured steels, LPBF manufactured steels are greatly affected by the rough surface finish, as well as other surface defects caused by micropores, surface cracks and un-melted and partially melted powder particles that are stuck on the surface. Additionally, the unstable molten melt pool aggravates the surface roughness [279,280]. The higher surface roughness ( $R_a$ ) paves the way for the higher local stresses under the dynamic loading conditions, which result in lower fatigue limits and consequently reduces the fatigue life of LPBF processed steels [281]. High cycle fatigue (HCF) limit is strongly dependent on the surface roughness related defects compared to low cycle fatigue (LCF). Hence, the HCF performance of LPBF steels can be improved by decreasing the surface roughness and the defects that occur on the part surface [281–283].

Another important parameter that has a considerable impact on fatigue properties is the build direction. The direction in which the load is applied to the built layers during LPBF process defines the fatigue strength [249,284]. The build direction governs the size, shape and the distribution of the LPBF processed defects, such as insufficient fusion holes and porosities that are elongated perpendicular to building direction [285,286] (see Fig. 32a–d). The horizontal built components (build direction normal to the loading axis) are exposed to longer inter-time intervals which experiences higher cooling rates and faster solidification (see Fig. 32d). Thus, a formation of finer microstructure and higher distribution of smaller scale porosities which causes less stress flow and concentrations around the defect that results in better fatigue limits as compared to vertical built component (build direction parallel to loading axis). The stress concentrations are maximum in vertical components due to comparatively weak interfacial bonding between successive layers and the axis of linear and planar bigger size defects (Fig. 32c). The arrangement of these defects normal to loading direction provides easy access paths for voids to grow bigger and coalescence, causing failure at lower fatigue limits. Irrespective of the building direction, LPBF built parts are generally more susceptible to the fatigue characteristics [167,277,287,288].

LPBF process induces distinct (elongated grain structure along the build direction) microstructure as compared to conventional process of steels. Also, LPBF process stimulates higher surface roughness, which is particularly detrimental to their fatigue performance [289,290]. Nehzadfar et al. studied fatigue behavior of LPBF process of steels under the influence of process induced defects such as voids, oxides, un-melted powder particles, and other surface defects causing higher roughness. Other researchers [249,291] reported that in addition to crystallographic texture and the anisotropic distribution of process defects, LPBF processed 17-4 PH is highly reliant on the build orientation under both low-cycle and high-cycle fatigue properties. Fatigue limit of LPBF built components depend on directions of load applied. For parallel loading to the direction of grain growth, crack path was highly tortuous, resulting in slow crack propagation and yielding high fatigue limit [290]. On the other case loading perpendicular to the grain long axis, the crack propagation along grain boundaries was straight and easy without any resistance to the applied load [180,217]. Crococo et al. found that the fatigue properties of LPBF processed maraging steels were isotropic, and with a fatigue limit of 600 MPa [292], which is approximately equal to 1/3rd of the static yield strength; which is in line with fatigue limit obtained for conventionally-produced maraging steels [293,294]. Isotropy is caused because of the weak texture in this type of steels as a consequence of the martensitic phase transformation. The achieved fatigue life of LPBF built H13 tool steel was significantly below that of conventionally produced steel [265]. This can be related to LPBF process induced residual stress and the higher sample surface roughness [264]. The higher surface roughness of LPBF processed steels is particularly detrimental to the fatigue performance. It is found that by employing

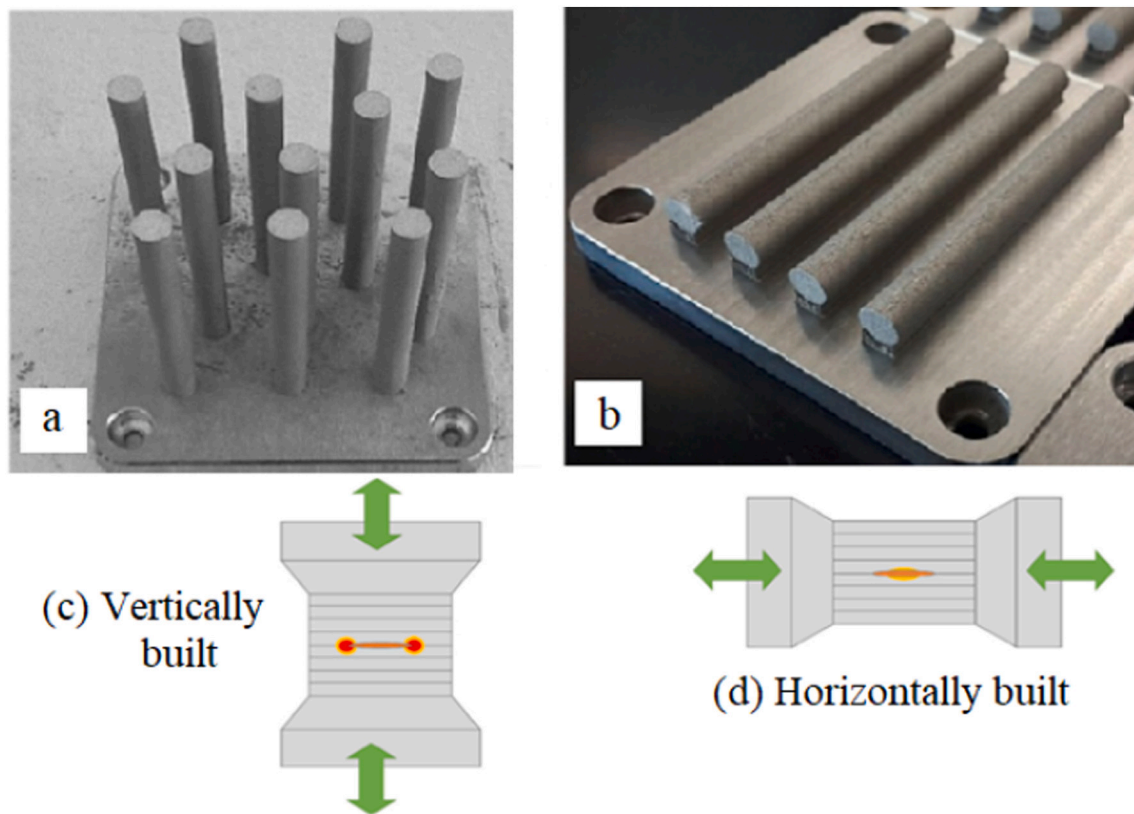


**Fig. 32.** Schematic illustration of LPBF build directions and stress concentrations associated with it, (a) vertically built, (b) horizontal built LPBF specimens, (c) higher stress concentrations around the defect in the vertical sample and (d) fewer stress concentrations in the horizontal sample [249].

post-process surface finishing treatment, fatigue limit can be doubled [180,282]. Stress relief heat treatments and hot-isostatic-pressing (HIP) both have only a marginal effect on fatigue performance, but primarily, after surface finishing post-process treatment, the fatigue limit lies in the range of conventionally processed steels [180,217,282].

The biggest challenge of LPBF process pose is the selection of optimum set of processing parameters from a wide array of parameters. Each parameter presents its own impact on the final properties of the manufactured part. Thus, controlling and estimating the characteristics of the final product is a very daunting task. Inappropriate energy densities result in the formation of unfavorable defects, which impart local stress concentrations during cyclic loading and leads to premature fatigue failure. Even by selecting optimum laser fluence, few small entrapped spherical gas pores inevitably occur in the LPBF processed parts. However, the effect of these pores on fatigue life of LPBF processed 316L steels is unaccountable, as they are less sensitive to notch due to its higher ductility and more resistant towards defects and residual stresses [295]. LPBF process induced defects formed due to lower or extremely higher energy densities are more detrimental to HCF because of their higher level of stress concentrations [296].

##### 5. Effect of post process treatments on LPBF process of steels

The impact of post process treatments on microstructure, surface texture and mechanical properties of LPBF built steels have been studied by many researchers [69,210,247,273–275,287–303]. The most commonly used post-process heat treatment processes are annealing (with vacuum, argon etc.), solution heat treatment (in air cooling, water quenching etc.), and ageing. In addition, a typical industrial densification post processing method: hot-isostatic pressing (HIP) is accustomed to drastically reduces the micro-defects, and effectively improves the uniformity of microstructure. HIP refines the microstructure by the

dislocation migration, and recrystallization of grains, thereby enhancing mechanical properties of LPBF processed steels [274]. Unlike hot working processes, cold working post processing method such as shot peening can be employed. Shot peening induces compressive residual stresses, grain refinement and macro strain, thereby improving the surface roughness, microhardness, compressive yield strength and wear resistance [247]. Other post-processing methods that are mainly focused to enhance the surface integrity characteristics of LPBF built steels are finish machining (FM), vibratory surface finishing (VSF), drag finishing (DF), laser polishing, magnetic field-assisted finishing, grinding, sandblasting and electro-polishing [300]. The surface roughness of LPBF built steels can be reduced (from 8.2  $\mu\text{m}$  to 0.05  $\mu\text{m}$ ) by grinding [240]. Lower surface roughness (by 48.72%) was reported after sandblasting in two phases [304].

Gas atomized maraging steel powders generally contains only ( $\alpha$ ) martensite phase. LPBF built specimens contain a large number of nano precipitates embedded in the matrix of columnar martensites along with the traces of austenite ( $\gamma$ ) phase [297–299]. The inherent heating and rapid cooling during LPBF process cause the phase transformation from martensite to austenite. Despite the revision of martensite to a more stable austenite phase transformation, the size and the number of austenite increases during ageing process [297]. The ageing post-process treatment provides ample time for the initiation of intermetallic compounds that are heterogeneously precipitated in to dislocations resulting in diffusion and grain growth. Solution heat treatment effectively dissolves alloying elements into a supersaturated austenite solution. Solution heat treatment (at 820–850  $^{\circ}\text{C}$  for 1–2 h) above the austenite finish (750  $^{\circ}\text{C}$ ) temperature with the age hardening (at 460–520  $^{\circ}\text{C}$  for 5–24 h) leads to the formation of intermetallic precipitates [298]. These formed intermetallic precipitates induces uniform dissolution of alloying elements into austenite solid solution. Consequently, cooling the austenite results in the formation of complete

martensite by eliminating austenite [298,299]. The average grain size remains the same for both as-built LPBF and aged steel specimens, while the martensitic matrix grain growth and the grain orientation substantially changes in case of solution treated-aged parts. Nanoprecipitates consists of spherical nanoparticles with an amorphous outer shell and crystalline core structure (see Fig. 33a), a line scan showing the atomic composition of each element in the precipitate is shown in the Fig. 33b. Maraging steels are generally strengthened by  $\text{Ni}_3\text{Ti}$  precipitate phase. In some cases, Ti is replaced partially by other elements such as Mo, Co or Al, depending on the composition of the alloy [297].

Salman et al. revealed a single-phase austenite in as-built LPBF followed by post-process heat treated (annealed) sample at various temperatures for 316L stainless steels (see Fig. 34a–f) [275]. Finer equiaxed sub-grained (nano-precipitate with amorphous structure rich in Mn and Si) characteristic cellular microstructure embedded into 316L matrix resulted in both as-built LPBF and annealed SS samples. They did not report any changes in random crystallographic orientation in microstructure except the lone difference being the average cell size. Size of the cells was gradually increased with increasing annealing temperature. Higher annealing temperature caused grains and cells to grow bigger until the cellular microstructure was no longer be observed at higher temperatures ( $T \geq 1273 \text{ K}$ ) [275].

Sun et al. compared the microstructure of wrought and LPBF produced 17–4 PH steels in as-built, solution heat treated ( $1038 \text{ }^\circ\text{C}$  for 4 h) and aged ( $482 \text{ }^\circ\text{C}$  for an hour) samples. From their research it was found that, both solution and ageing heat treatments have no significant impact on the initial microstructure of wrought as well as-built LPBF 17–4 PH steel samples [231]. Few other researchers have studied the solution heat treated and aged microstructures of LPBF processed 17–4 PH steel and their investigation yielded similar results as one to that of Sun et al. [249,305].

Heat treatment of LPBF built duplex stainless steels was examined by [306]. Their observations reveal that recrystallization occurs in the temperatures ranging between  $900$  and  $1200 \text{ }^\circ\text{C}$ , whilst, the maximum austenite fraction was achieved at the intermediate temperature  $1000 \text{ }^\circ\text{C}$  [306]. They also reported that missing nitrogen during the process but without quantifying it. Fig. 35a–d gives a clear picture of the comparison between as-built LPBF and heat treated (recrystallized micro- and nanostructure) of duplex stainless steels. LPBF processed duplex stainless steel displayed almost fully ferritic in as-built condition. On the contrary, conventionally processed steel displayed small austenite

grains and chromium nitride precipitates along the grain boundaries (Fig. 35b & c). Applying suitable post process treatment partially recovers the desired duplex austenite/martensite microstructure (see Fig. 35e & f) [306].

Post process heat treatment at  $500 \text{ }^\circ\text{C}$  dissolves the retained austenite, at the same time the dominant cellular microstructure disperses at the tempering temperatures above  $600\text{--}700 \text{ }^\circ\text{C}$  in LPBF processed H-13 steel [192,307]. Also, Martensitic microstructure, similar to that of conventionally processed tool steels (without any trace of retained austenite) could be achieved by complete austenitization followed by quenching [192,308,309]. As-built LPBF samples that are tempered directly at low tempering temperatures did not exhibit any drop-in hardness value due to softening of the martensite, coincidentally which is also the characteristic of conventionally manufactured H-13 tool steels [192,307]. Furthermore, secondary hardness peak transitioned to higher temperatures can be attributed to the large formation of carbon and carbide embedded in the retained austenite that is stable up to relatively high temperatures [192,307]. Secondary carbides could be formed only after this austenite is completely decomposed. As-built LPBF samples displayed a relatively lower tensile yield strength and UTS as compared to heat treated and conventionally manufactured steels. This could be attributed to the extreme brittleness that lead to premature failure without any deformation [68,262,264–266]. Again, tempering effect did not display any changes in as-built LPBF steels. Instead, the tensile value remained same as wrought and heat-treated tool steels [265]. However, the ductility obtained was much lower in as-built as well as aged samples, presumably due to the surviving process-induced defects [68,262,264–266].

Salman et al. investigated the changes induced by the various post process heat treatments on the mechanical properties of LPBF built 316L stainless steels under tensile loading conditions [275]. They revealed that the tensile strength of the 316L samples decreased with increasing annealing temperature as a result of the microstructural coarsening (see Fig. 36a). As-built LPBF samples exhibited an excellent combination of strength and ductility, along with the plastic deformation exceeding 50%. This can be attributed to the complex cellular microstructure and subgrains along with the misorientation between the grains, cells, cell walls and subgrains; which would prevent the formation of higher local stresses, repel dislocation movements and defers premature fracture until ultimate tensile stress is reached [275]. Degradation of yield strength and ultimate tensile strength with increasing annealing

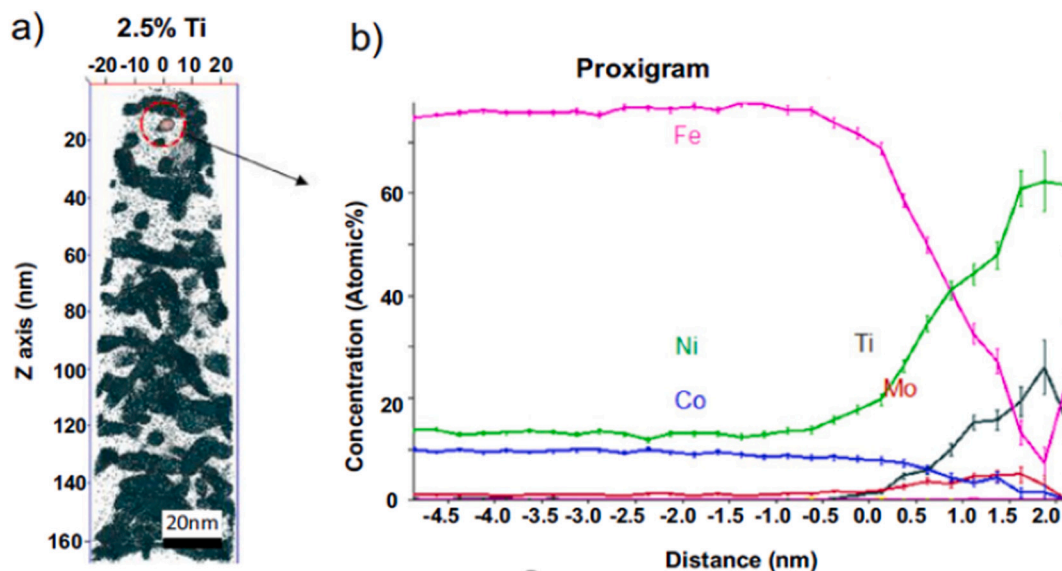


Fig. 33. Atom probe tomography (APT) images of LPBF maraging steels for the aged sample at  $510 \text{ }^\circ\text{C}$  for 2 h (a) spherical precipitate enriched in Ti and Ni, and (b) line scan showing the atomic concentration of each element [297].

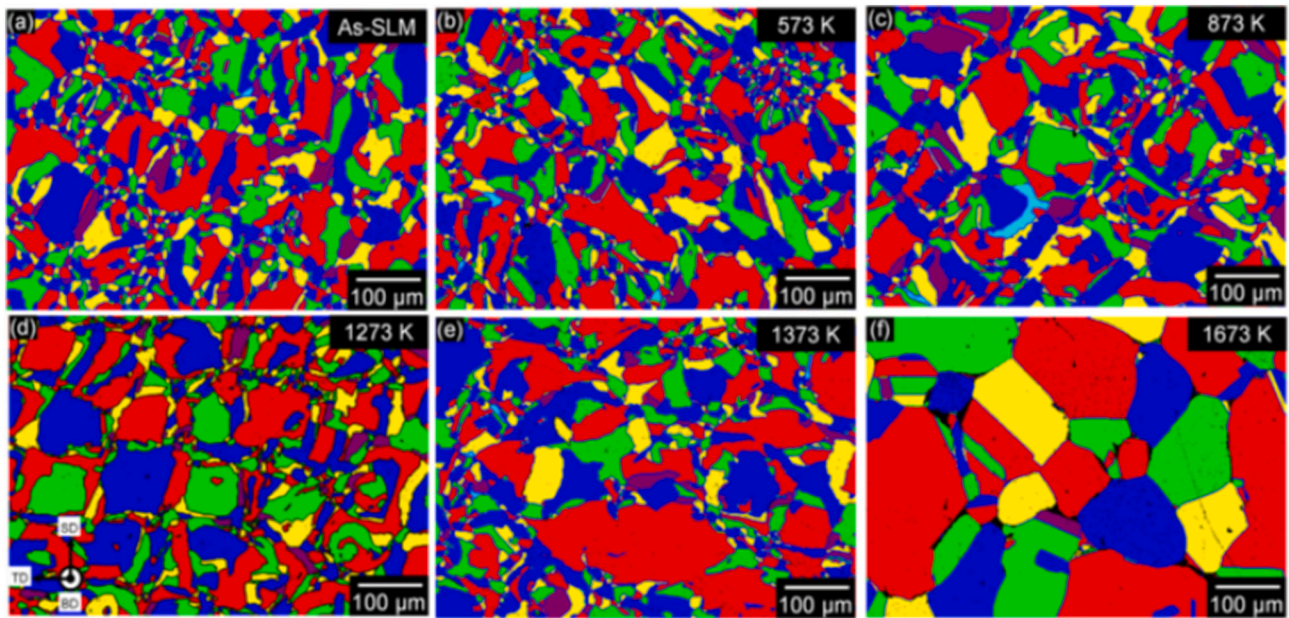


Fig. 34. EBSD Grains maps of 316L stainless steel for: (a) as-built LPBF samples and specimens annealed at (b) 573 K, (c) 873 K, (d) 1273 K, (e) 1373 K and (f) 1673 K [275].

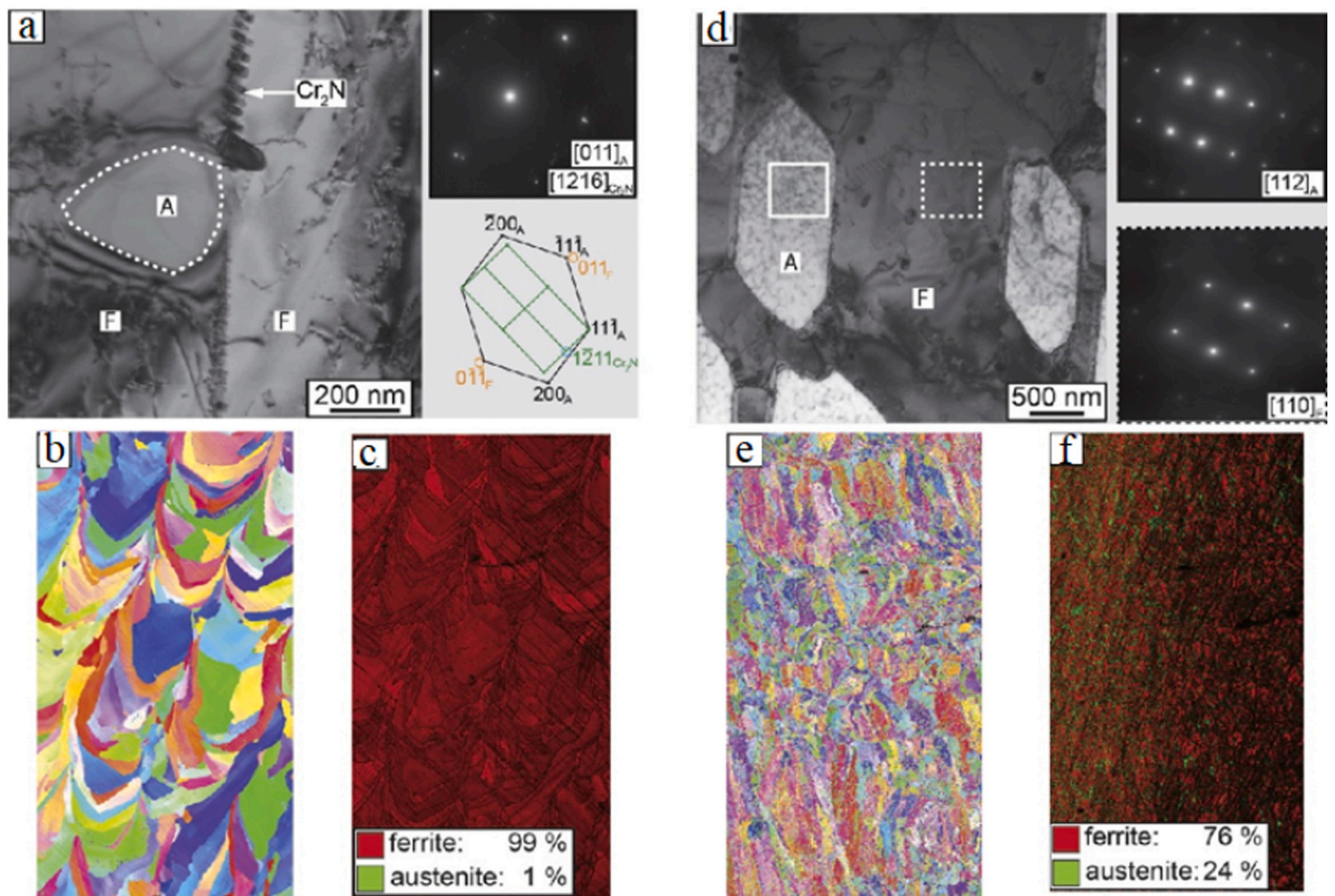


Fig. 35. TEM images of LPBF produced duplex stainless steel in the (a) as-built (d) heat treated condition, (b and c) electron backscatter diffraction (EBSD) inverse pole figure, and phase mappings for as-built condition, while (e and f) for heat treated condition [306].

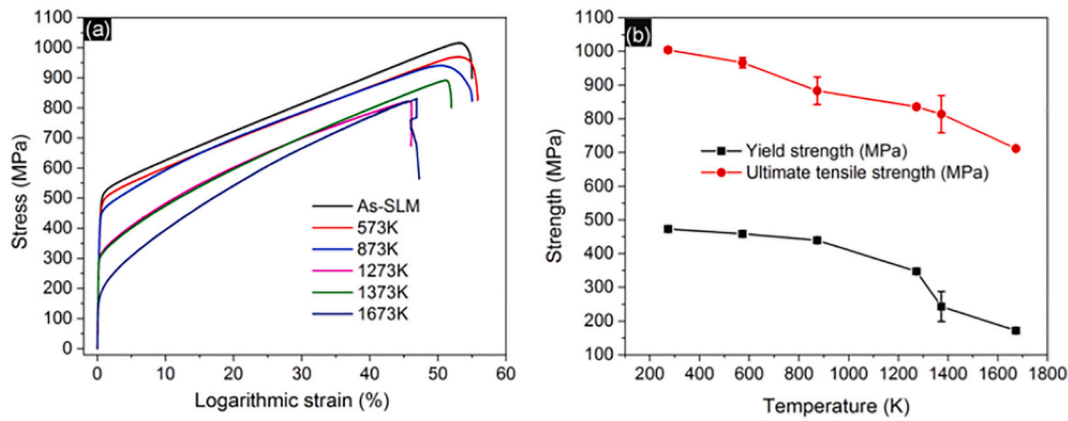


Fig. 36. (a) Tensile stress-strain curves of LPBF processed 316L stainless steel at different heat treatment conditions, and (b) effect of heat treatment on the yield and ultimate tensile strength of the different samples [275].

temperature is shown in Fig. 36b. This is due to microstructural variations that occur under various post process heat treatments. No preferred orientation of the grains was observed as annealing caused the growth of grains and cells while decreasing the dislocation network [275].

Conde et al. reported enormous improvement in hardness values (~60%), and bending strength (~73%) similar to that of UTS while the substantial decrease in ductility can be noticed in age hardened martensite steel sample as compared to the as-built LPBF sample [298]. This remarkable hardness and tensile strength enhancement can be ascribed to the precipitation hardening and strengthening by the formation of fine precipitates of intermetallic compounds such as  $\text{Ni}_3\text{Ti}$  in the martensite matrix. To overcome the loss of ductility, solution treatment combined with ageing or hot isostatic pressing can be employed which would result in better overall mechanical strength [298], along with considerable improvement in elongation (ductility) that lies within the standard ranges [69,210,274,297]. A stable microstructure was reported after conducting the stress relieving through post process heat treatments with temperature up to 650 °C [180]. As a result of unchanged microstructure, there was no significant effect on crack propagation or the fatigue life of austenitic steels [180]. However, at higher annealing temperatures (above 800 °C in a furnace or HIP), resulted in partial recrystallization of austenitic steels. HIP induces partial recrystallization which is predominantly dual-mode isotropic. Consequently, this isotropic microstructure eventually lead to isotropic crack propagation under fatigue loading. Similarly, Saeidi et al. found that there were no changes in microstructure at annealing heat treatment at 800 °C [310]. In addition, they noticed unstable phase transformation in the form of sharp edged  $\delta$ -ferrite at annealing temperatures over 1150 °C. This needle shaped  $\delta$ -ferrite was stable during slow cooling to room temperature as indicated in the equilibrium phase diagram. Combination of recrystallization and coarsening phenomena renounce tensile strength of the steels [310].

Applying appropriate post process solution treatment followed by subsequent ageing treatment helps in transforming the retained austenite to martensite. Higher YS can be obtained as compared to conventional processed 17-4 PH steels but with the compromised ductility [305,311,312]. Unfortunately, the fatigue life of LPBF processed 17-4 steel has minimal advantage of undergoing any post process heat treatments under all conditions. At high strain amplitudes, when fatigue life is short, the impact of defects is weaker than at longer fatigue life and low strain amplitudes. Since internal defects act as crack initiation site as well as dominating the mechanical behavior of the strong, heat-treated 17-4 steel sample displays a higher fatigue strength in the low-cycle regime as compared to the as-produced sample due to higher internal defects (Fig. 37) [249]. The fatigue life of as-produced LPBF H13 steels was significantly lower than that of conventionally produced

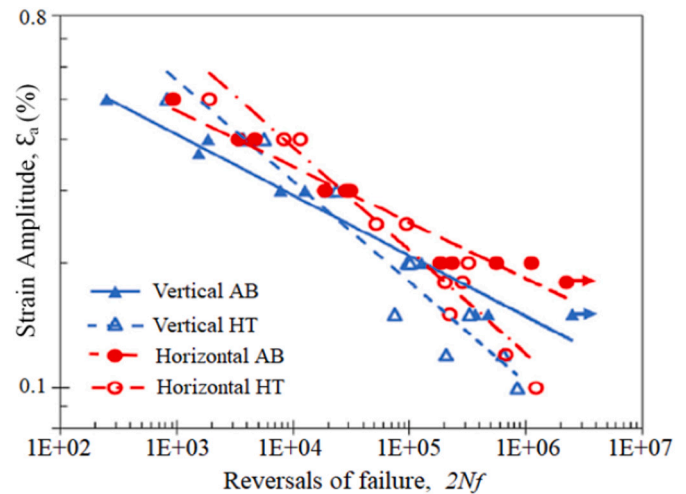


Fig. 37. Experimental data and curves of Strain-life fatigue for LPBF 17-4 PH SS in different building conditions [249].

steels [265]. Becker et al. investigated the fatigue crack growth rates of peak aged material LPBF processed maraging steels, the authors found that fatigue crack growth rates were isotropic and equal to conventionally-processed maraging steels [261]. Isotropy is due to the weak texture orientation in these type of steels which is a consequence of the martensitic phase transformation [261]. This could be correlated to the LPBF process induced residual stress and higher surface roughness [264]. Surface machining had limited impact on improving the fatigue strength as it remained significantly lower than that of reference material (50% failure probability at 107 cycles strength of 283 MPa compared to 600 MPa) [264]. The improved fatigue properties were attained when the stress relief and austenite decomposition heat treatment at 600 °C were employed [265].

Sagar et al. studied the impact of different build directions and post process heat treatments (ageing and over ageing) on HCF and LCF of LPBF built 15-5 PH steels [313]. Based on their findings, aged specimens subjected to LCF performed better than as-built specimens in both vertical and horizontal build directions, whereas, the performance of the same samples subjected to HCF was poor compared to as-built LPBF parts. This was accredited to the ageing treatment; which resulted in precipitation strengthening of the matrix through copper-rich precipitation, however, this precipitation strengthening could lead the specimen more defect sensitive in HCF regime [313]. Also, overaged samples tend to be less sensitive to the defects than aged specimens in HCF

regime. This could be attributed to the over ageing heat treatment, which resulted in a more ductile LPBF built sample through microstructure grain coarsening of copper-rich precipitates in addition to the increased amount of retained austenite [313]. In general, the higher surface roughness caused by irregular shaped defects e.g. voids, partially-melted/un-melted etc. in LPBF processed samples are more sensitive to the fatigue life than its wrought counterparts. However, relatively lesser number of defects were reported for the vertically built LPBF specimens [313].

The removal of residual stresses via stress relief (SR) heat treatment (5 h at 470 °C) does not necessarily improve the fatigue behavior. Instead, removing critical crack initiators by machining the surface of LPBF processed 316L steel significantly improved the fatigue performance. The superior fatigue performance was achieved through machined samples with and without SR heat treatment when compared to conventionally fabricated 316L steels. SR treatment coupled with the machining is recommended to obtain desired fatigue performance when cyclically loaded at high stresses. Overall, the post process treatments has very minimum effect on the fatigue performance of LPBF processed steels [287,302].

## 6. Summary and future trends

### 6.1. Steels in LPBF process

An outline of already published and ongoing research reveals that LPBF process influences the time related spatial variations of molten melt pool, thermal gradients induced vortex flow, solid-liquid interface velocity which leads to the formation of spatial microstructure and diverse mechanical properties within a specific geometry and the processing conditions for a wide variety of steels. The limiting factors for research and development of LPBF process of steels are mainly related to: Firstly, LPBF technique is not fully standardized and reliable for the industries to completely adapt as it is a maturing technology. However, some of the steels structural components have been approved to be used in the service. Secondly, it is difficult to regulate the metallurgical defects, microstructure evolution, and efficacy of mechanical performance driven studies have not been consistent. LPBF processing of steels research is largely concentrated on the limited type of steels. Current research trend is mostly focused on LPBF process optimization, studying the impact of post-process treatments on the microstructural changes and mechanical behavior (under static loading) of various alloying compositions, and commercially available stainless steels [314–317], tool steels [26,30,215], and maraging steels [297–299]. LPBF processing of alloy composition steels intensifies the solid-solution limit of the alloying elements in the molten melt pool and leads to the formation of unfavorable microstructure. Similarly, carbon bearing tool steels experiences relatively uncontrolled in-situ-tempering during LPBF processing. It is extremely important to accurately control the interplay between LPBF process parameters and the different type of steels, and possibly redesign/modify the new type of steels whose composition is best suited for the LPBF processing features, concurrently fulfill the desired functional properties. Some alloy combinations of stainless steels (i.e. 304 SS, 410 SS, 420 SS, 430 SS, Inco904L SS), maraging steels and other low alloy steels are not completely explored in LPBF process. Meanwhile, there is a continuous scope for expanding LPBF process of steels. A further investigation of other types of steels such as iron-based and nickel-based superalloys, single crystal alloys, and cobalt chromium alloy steels is much-needed. These materials are of high interest in wide range of aerospace and biomedical applications.

As a general rule, steels and iron-based alloys are intended for structural applications. However, there is an increase in demand utilizing LPBF process for fabricating steels parts with functional properties. Fe-Al (low-density low-carbon ferritic) steels display outstanding strength to weight ratio. Owing to excellent resistance to corrosion, wear and oxidation LPBF built Fe-Al steels are considered for high

temperature system's functional applications [164]. This include jet engines, turbine blades, heat exchangers piping, holding fixtures of a heat treatment furnaces and etc. The next category of functional LPBF processed steels are invar steels. The unique features on invar steels (FeNi or FeCoNi steels) possess over a wide temperature range and a negligible coefficient of thermal expansion, makes them perfect candidates in high temperature applications such as household appliances, electronic devices and aircraft controllers. Electrical steels are the other important category of LPBF functional components that are already in service. These electric steels are soft-magnetic materials that demand a specific crystallographic texture (i.e. Goss texture,  $\{011\} \langle 100 \rangle$ ) to achieve a low hysteresis losses [318], and have high permeability which means that the electrical current needed to produce magnetization should be as minimal as possible. This exclusive characteristics makes electric steels best suited for generators, alternators, amplifiers, transformers and iron electric motor applications. Furthermore, electrical steels are subjected to the series of rolling and annealing treatments to achieve Goss orientation; induces better power and higher permeability properties in the rolling direction. However, this (rolling and annealing treatments) requirement can be easily substituted by LPBF processing. On the other hand, by increasing Si content in Fe-Si-alloy which is again a soft magnetic polycrystalline metal alloy. LPBF processing of modified Fe-Si alloy steel exhibit a higher electrical resistivity and a lower hysteresis loss compared to the conventional electrical steels [319]. Modifying bulk Fe by adding Mn content enhances corrosion resistance along with displaying good cytocompatibility during LPBF process of Fe-Mn steels [320]. A basic research investigation is not sufficient, an advanced and thorough research is vital before using Fe-Mn scaffolds as functional components. Some of the other steels and iron-based functional components that are considered for use in laser based additive manufacturing includes amorphous, nanocrystalline, and magneto-caloric materials [321]. A number of LPBF processed steels and iron-based alloy components have already been in use for economic reasons, and further growth is expected in the near future.

Development of LPBF process steel lattice structures with unique thermal, mechanical, electrical and acoustic features opened the door for cellular light weight structures applications in aerospace and biomedical industries. Cellular structures offers an exciting opportunity especially in design light weight applications due to their high strength to stiffness ratio provided by the porous structure. The light weight applications includes personal protective equipment (PPE), conformal cooling channels, thermal controllers, bone scaffolds, antimicrobial functionality possessing medical implants, sports equipment and etc. There have been good number of researchers attempted to study the microstructure relating to the mechanical properties of LPBF processed steel lattice structures. However, comprehensive analysis including FEM prediction of defects, structure and property relationship of LPBF steel lattice structures, and their overall performance capabilities is one area of the future scope to be explored in upcoming days. Functional graded steel lattice structures which display varying densities across the structure in contrast to regular lattice structures with uniform density throughout the structure is another exciting topic requires further research.

Future developments of LPBF process of steels in the healthcare sector is focused on various features, such as biocompatibility, corrosion resistance, mechanical properties, printing properties, biomimetics, and degradation. The development of new type of steels as biomaterials with various compositions to achieve reprogrammed mechanical properties and functions would become a reliable method for building various organs and tissues with diverse mechanical requirements. For example, type 302 stainless steel was introduced solely for its application in orthopaedic surgery. Additionally, 316L type stainless steel is most commonly used in surgical procedures to replace biological tissue or to assist in stabilizing a biological component like bone tissue to aid the healing process. Stents, screws, plates, scaffolds are some of the commonly used functional components of LPBF produced 316L stainless

steels [322]. This type of stainless steel is the most corrosion resistant when it is in direct contact with biological fluid. A surgical implant must not be vulnerable to corrosion when positioned inside the human body to avoid any possible chance of infection. Hence, 316L stainless-steel implant is particularly effective when it is used in cold-worked condition, due to the non-existence of any inclusion in this material. Steel materials with inclusions also contain sulphur which is a key alloying element to encourage corrosion in steels. 316L stainless steel used in surgical implants contains approximately ~17 to ~19% of chromium and ~14% nickel. Corrosion resistance can also be achieved with the carbon, but only when the carbon is in a solid solution state. Chemical composition of stainless steel can be altered by adding chromium (~16%) to become corrosion resistant. Similarly, the addition of carbon and nickel (~7%) helps to stabilize the austenite in stainless steels. Adding Pd into TWIP steels can significantly improve corrosion resistance by forming decent intermetallic compounds. Similarly, adding silver into TWIP steels results in improved mechanical strength by establishing  $\epsilon$ -martensite during deformation. Also, molybdenum is added to the steels implants that act as a protective layer sheltering the metal from exposure to an acidic environment. It is important to note that including ferrite element into stainless steel gives the metal a magnetic property, which is not ideal for surgical implants as it could obstruct the Magnetic Resonance Imaging (MRI) equipment. One of the most evident problems with using magnetic implants is their susceptibility to heating which could change the shape or structural position of this steel implants. The potential solution to resolve this magnetic property is by adding Mn in to steels, which enhances MRI compatibility by promoting austenitic growth. LPBF process of steels and iron-based alloys as biodegradable medical implants is the one of the exciting and novel research areas that can be further explored. Meanwhile, enhancing mechanical properties along with maintaining biocompatibility as well as good corrosion resistance of LPBF processed steels implants is another challenge which require detailed attention. Development and fabrication of complex biodegradable LPBF processed implants with porous architecture imparts poor surface quality. A suitable post-processing is necessary to overcome this issue. Addressing the link between post-processing and the poor surface finish of these implants is extremely paramount which is another important topic for the future examination.

LPBF process of steels induces process related higher residual stresses, inevitable internal defects such as porosities, balling and thermal cracks that result in higher surface roughness. Metallurgical defects or any irregularities present at the surface pose an adverse effect on the final part geometry, and consequently, lead to poor surface quality and mechanical performance of the LPBF fabricated parts. Hence, unique and effective statistical approaches are needed that would consider of all these interdependencies of process related parameters while a minimum number of experiments are to be conducted. A considerable number of researchers have attempted to optimize the LPBF process by altering parameters and used many new approaches like employing multiple laser beams, laser de-focusing, laser re-melting, or adapting different scan strategies, substrate preheating and/or using a hybrid substrate to boost the efficiency of LPBF technology. However, there is still lack of detailed scientific understanding; how these inevitable metallurgical defects associated with LPBF process are going to behave when subjected to the dynamic loading conditions i.e. fatigue properties. A very limited research has been carried out focused on the influence of process parameters on the surface quality and fatigue properties of an LPBF processed product to optimize the given process in terms of time, cost, and properties of a product.

Also, from the existing literature, most of the experiments that were carried out are based on recommended parameter settings provided by LPBF/AM machine vendors, which might induce uncertainty in the outcome of the process depending on the operator or expert knowledge of the vendors. Mathematical models based on FEM and regression analysis are developed to predict the process performance. However,

these methods are usually not sufficient mainly because they lack the ability to extrapolate the given input data or information. Overall, the vast majority of available studies in the literature have investigated optimal process parameters for steels using simulation and/or experimental approach. The limitation of this approach is, if we change the experimental conditions (e.g., materials, process, system, or environment conditions), the resulting optimal process parameters settings may no longer be valid and applicable. New experiments are required to revalidate the samples. In addition, it is worth noting that very little attention has been paid towards the systematic study of surface texture characterization. The surface texture of LPBF processed steel parts impart anisotropic or sometimes isotropic. Surface finish is generally very sensitive to the mechanical performance especially under dynamic loading (fatigue testing) conditions. As in case of HCF limit, which is predominantly dependent on the surface texture of the LPBF fabricated steel products.

## 6.2. LPBF technology

LPBF process of metals is gaining popularity while displaying significant growth along with taking greater steps in novel and advanced technologies to make it more competent, cost-effective. LPBF technology offers new opportunities in production paradigms, versatility of fabricating complex structures ranging from various scientific and technical innovation industrial applications to the retail and personal products. Due to higher freedom of design, LPBF process is very efficient in producing individual or customized products mainly in healthcare, aerospace, and automotive industrial applications. Medical implants, lattice type structures, high temperature resistant, and high strength combined with lower weight large components are among the examples. LPBF technology is also included in the group of sustainable and efficient production processes which helps in saving resources and protecting the environment. Sustainability studies carried out on LPBF process displays that significant reduction in material waste and fuel consumption are the two other principal benefits. Moreover, eco-design in LPBF process provides this opportunity where the environmental issues are considered in each design and fabrication phase, in accordance with, various eco-design tools, for example, life cycle analysis (LCA) method, could become handy to quantify the environmental impact associated with the LPBF built products. Despite several exciting opportunities and advantages offered by LPBF technique, there are still some obstacles that act against its rapid growth, such as size limitation, production time, limited number of materials, machine and production costs. LPBF technology is not completely matured yet and is still in its infancy stages. The technology needs to be further developed and standardized in the coming years, including the availability of the LPBF machines, and feedstock materials at a lower cost. Also, expanding the capabilities of the LPBF machines so that they are more autonomous, faster, more accurate and able to mass-produce design surface quality components in addition to the superior mechanical properties. In particular, innovative research and development steps are to be taken up by governments, academics, public and private sectors to design and improve the speed and accuracy of LPBF machines and raise the number of its applicable metal alloys and new methods while maintaining its economic viability.

LPBF process needs to overcome some of these specific technical challenges before it becomes a reality for operational use in the industry. LPBF process lacks robustness, repeatability, reliability and process monitoring because two machines from the same manufacturer (or from different manufacturers) can yield different part quality. It is a requirement to understand, and efficiently be able to control the effects of machine-to-machine variability. It is also paramount to develop specifications and industrial standards for the processing of LPBF steel components. Development of integrated processes, through the advancement of technologies for monitoring and control of production processes needs to be prioritized. Find/propose alternatives using existing conventional qualification methods based on validated models,

probabilistic methods and standard parts. New standard and advanced non-destructive (NDT) capable of sensing LPBF processed critical defects with a high degree of accuracy shall also be developed. New design guidelines with innovative and customized structural features are needed to build optimized components in structural terms and weight, which is essential for the validation of virtual models based on physical models, to predict the characteristics of microstructure, surface texture, mechanical properties and corrosion properties. Existing design tools are not capable of capitalizing the full advantage from the process due to the compatibility of LPBF process specific features with present LPBF machines as the design rules are not fully checked and established. In addition, designers are forced to follow the design rules set for conventional manufacturing processes. Along with the product level testing, qualification process, methodologies for part verification and the product assurance of LPBF built parts need to be established.

LPBF technology can be enhanced by introducing genetic algorithms, artificial intelligence, machine learning, and other similar computer automated systems, which are helpful to optimize process parameters. Also, these intelligent LPBF systems are beneficial to predict the geometry of the molten melt pool, microstructure, surface finish and mechanical properties by eradicating time-consuming, expensive trial and error methods to carry out the physical experiments. For example, introducing trained computer vision or unsupervised machine learning algorithm, operative on a small to medium size training data base of image patches will be beneficial to detect and classify the anomalies that occur during LPBF process. Similarly, developing new algorithms that are able to automatically alter the LPBF processed part geometry by compensating CAD model would be interesting. A significant update of the existing CAD software is required as it holds more important information than the normal STL files. Thereby, upgraded software could make reliable and meaningful alterations based on the example constraints already stored in the CAD file. This novel approach can be applied not only for the simple parts but also be useful for the complicated parts including internal surfaces, overhangs of curved and inclined LPBF processed components. Prediction, maintenance and regulation the dimensional tolerance variations of LPBF produced components are extremely important. Geometrical tolerances must kept to the lowest minimum tolerance range. The existing statistical analysis to develop linear models for the tolerance prediction is not sufficient. Adapting machine learning techniques for the prediction of dimensional features would be very valuable.

LPBF product quality can be improved by minimizing or eliminating the defects. Metallurgical defects could be controlled by employing advanced numerical modelling and simulation methods, as well as real-time defects elimination by in-situ detection. In addition, coupling near infrared image (NIR) camera within LPBF systems would become advantageous to analyse each layer characteristics before and after it is selectively melted and deposited. The NIR data that provides information about the possible location of metallurgical defects and the surface dimensions can be utilized as an important tool to mitigate LPBF process related defects. Innovative hybrid LPBF process (combining LPBF technology with other AM process like cold spraying) would become more beneficial to fabricate high quality functional products with improved properties. It is essential for LPBF technology to advance in the direction of multiple materials fabrication of different products simultaneously. Developing intelligent materials should be concurrent with some advances in LPBF technique itself. With this advancement, smart materials can be produced into complex and multifunctional structures with higher precision and particular responsiveness. Altering the steel alloy by mixing with another metallic powder at various compositions on demand to create a flexible system is another interesting aspect in LPBF of steels. This flexible prototype system can work for in-situ alloying of various elements, in the meantime helpful to produce composite materials. There has been sincere effort to investigate the LPBF feasibility on fabricating multi-materials (Fe and Al-12Si metallic powders) [323]. These LPBF composite materials applications are found in hybrid or

translational junctional elements; nodes in heterologous frame space. However, a detailed work is needed in further to investigate the various processing strategies to enhance the part quality as well as component metallurgy [323].

### 6.3. Materials

The other key challenges faced by metal LPBF technology is the cost of materials and the array of materials. To tackle this, materials suppliers need to invest highly in the research and development of new LPBF materials to claim their stake in the global market. It is estimated that the cost of materials shall be driven down in the near future and a wider array of materials would be made widely available. In addition, the demand for industrial-grade materials such metals and its alloys also driving growth, particularly across the critical industrial sectors like aerospace, automotive, shipbuilding, transportation, and etc. Hence, there is a continuous rise in demand for materials like high-performance low weight functionally graded materials. New materials shall be developed to optimize the production process and the final quality of LPBF processed components. Physical (morphology, flowability, particle size distribution, humidity, moisture content), and chemical properties (impurities level) of LPBF powders (including steel powders) are not fully defined to achieve functional parts quality. Currently, there is no powder handling or recycling specifications to ensure traceability and avoid contamination of feedstock materials, which needs to be established at the earliest convenience.

### 6.4. Post processing

The post-processing in LPBF technology is cited as “hidden dirty secret” because it is a necessary part of LPBF process workflow. Post processing has naturally been manual and highly labor intensive. Simplifying the entire LPBF process starting from designing a 3D computer model that goes for a print, to the finished part, which is ready to use has therefore been key imperative for the industries. An imperative that is been driven by complete automation. The ability to automate the post-processing stage comes with several benefits, such as saving costs in both manual labor force and machine running cost as well as being able to reduce the overall production times. For example, automated post-processing systems could be comprised of automated cleaning, polishing, injection molding to achieve smoother surface finish. The effect of existing post process heat treatments (stress relieving, solution/ageing, vacuum furnaces, hot-isostatic-pressing), surface treatments (mechanical and electrochemical polishing, abrasive flow polishing), and cleaning procedures (jet blasting, sand blasting) applied to LPBF processed components on the final properties is still unclear, which needs to be addressed.

It is utmost important for the researchers and manufacturers to shift their focus on design and development of specific application orientated-optimized part geometries, compositions, and functionality of AM/LPBF steels or other metal components. Overall, more and more researchers and experts in AM fraternity (including LPBF) are turning their interest towards fabricating bulk structures using customized large-format additive manufacturing machines, hoping to create large structures all at once, to avoid assembly or post processing methods that are expensive and time-consuming. All in all, the versatility at which LPBF and/or AM offers as non-conventional approach providing new opportunities for mass customization of complex parts by saving time, costs, and establishing process efficiency; which is playing a major role in branding AM is leading the subsequent main industrial revolution 4.0. Industrial manufacturing companies tend to enter the highly decentralized industrial revolution. However, AM experts presume that neither LPBF technology nor any other technique in AM process is going to substitute traditional manufacturing processes completely.

In the coming years, a greater correlation between the machines, materials and software is expected as manufacturers demand continuous

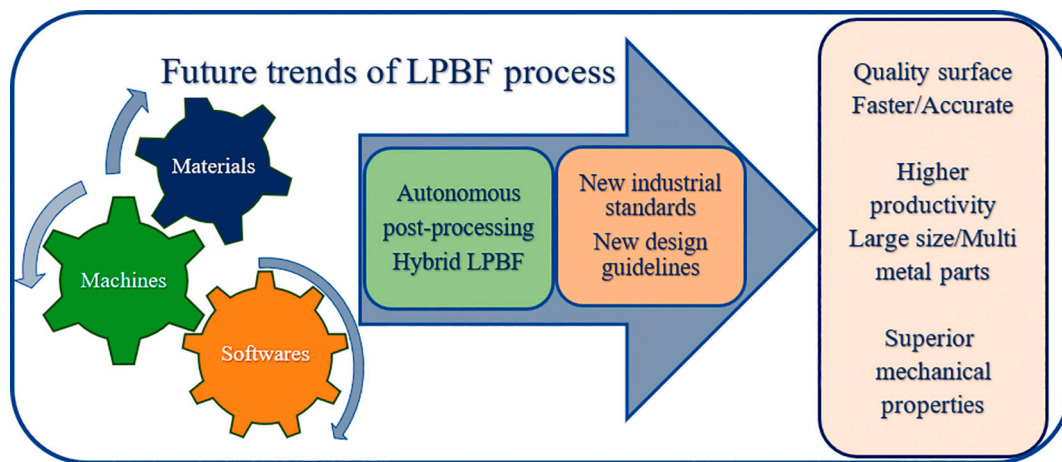


Fig. 38. Schematic illustration to show the correlation between the machines, materials, and software work together to ensure an end-to-end seamless LPBF process workflow.

workflows and systems that collaborates harmoniously (see Fig. 38). All of these elements would consequently need to come together, work hand-in-hand to ensure an end-to-end seamless LPBF process workflow.

#### Declaration of competing interest

The authors declare that they have no known competing financial interests or personal relationships that could have appeared to influence the work reported in this paper.

#### Acknowledgements

Dr. Shan Lou would also like to thank the EPSRC (EP/S000453/1) for funding this work. The authors gratefully acknowledge the UK's Engineering and Physical Sciences Research Council (EPSRC) funding of the Future Advanced Metrology Hub (EP/P006930/1).

#### References

- [1] Quader MA, Ahmed S, Ghazilla RAR, Ahmed S, Dahari M. A comprehensive review on energy efficient CO<sub>2</sub> breakthrough technologies for sustainable green iron and steel manufacturing. *Renew Sustain Energy Rev* 2015;50:594–614.
- [2] Peckner D, Bernstein IM. *Handbook of stainless steel*. McGraw-Hill; 1977.
- [3] Pellegriano J, Jamison K. US DOE Roundtable and Workshop on Advanced Steel Technologies: Emerging Global Technologies and R&D Opportunities. No. ORNL/TM-2015/742. Oak Ridge, TN (United States): Oak Ridge National Lab. (ORNL); 2015.
- [4] <https://www.thebalance.com/steel-grades-2340174>.
- [5] Herzog D, Seyda V, Wycisk E, Emmelmann C. Additive manufacturing of metals. *Acta Mater* 2016;117:371–92.
- [6] Hsiao CN, Chiou CS, Yang JR. Aging reactions in a 17–4 PH stainless steel. *Mater Chem Phys* 2002;74(2):114–34.
- [7] Fayazfar H, Salarian M, Rogalsky A, Sarker D, Russo P, Paserin V, Toyserkani E. A critical review of powder-based additive manufacturing of ferrous alloys: process parameters, microstructure and mechanical properties. *Mater Des* 2018; 144:98–128.
- [8] Kurnsteiner P, Stern F, Wilms MB, Streubel R, Kusoglu IM, Tenkamp J, et al. Microstructure formation and mechanical properties of ODS steels built by laser additive manufacturing of nanoparticle coated iron-chromium powders. *Acta Mater* 2020;206:116566–79.
- [9] W.D. Jr. Callister. *Materials Science and Engineering: An Introduction*, 8th Edition.
- [10] Ozsoy K. Examining mechanical properties of profiles manufactured aluminum extrusion dies using powder bed fusion. *Measurement* 2021;177:109266.
- [11] Am Tofail S, Koumoulos EP, Bandyopadhyay A, Bose S, O'Donoghue L, Charitidis C. Additive manufacturing: scientific and technological challenges, market uptake and opportunities. *Mater Today* 2018;21(1):22–37.
- [12] Correa EO. In: Sudnik Wladislav, editor. *Weldability of Iron Based Powder Metal Alloys Using Pulsed GTAW Process*, Arc Welding; 2011.
- [13] C. Selcuk, S. Bond and P. Woollin Metallurgy, Corrosion & Surfacing Technology Group, TWI Ltd, Granta Park, Great Abington, Cambridge.
- [14] Song B, Zhao X, Li S, Han C, Wei Q, Wen S, Liu J, Shi Y. Differences in microstructure and properties between selective laser melting and traditional manufacturing for fabrication of metal parts: a review. *FrontMech Eng* 2015;10.
- [15] Brooks WK, Tsopanos S, Stamp R, Sutcliffe CJ, Cantwell WJ, Todd J, et al. The production of open cellular lattice structures using selective laser melting. In: 6th National Conference on Rapid Design, Prototyping, and Manufacturing. Buckinghamshire Chilterns University College; 2005. June.
- [16] X. Li, Y.H. Tan, H.J. Willy, et al., Heterogeneously tempered martensitic high strength steel by Selective laser melting and its micro-lattice: Processing, microstructure, superior performance and mechanisms, *Materials & Design*.
- [17] Li W, Yang K, Yin S, Yang X, Xu Y, Lupoi R. Solid-state additive manufacturing and repairing by cold spraying: a review. *J Mater Sci Technol* 2018;34(3):440–57.
- [18] Alipooramirabad H, Paradowsk A, Ghomashchi R, Reid M. Investigating the effects of welding process on residual stresses, microstructure and mechanical properties in HSLA steel welds. *J Manuf Process* 2017;28:70–81.
- [19] Deng QL, Xie AN, Ge ZJ, et al. Experimental researches on rapid forming full compacted metal parts by selective laser melting. *Mater Sci Forum* 2006; 532–533:428–31.
- [20] Yakout M, Elbestawi MA, Veldhuis SC. Density and mechanical properties in selective laser melting of invar 36 and stainless steel 316L. *J Mater Process Technol* 2019;266:397–420.
- [21] Hong Y, Zhou C, Zheng Y, Zhang L, Zhen J, Chena X, Bai.. Formation of strain-induced martensite in selective laser melting austenitic stainless steel an. *Mater SciEng A* 2019;740–741:420–6.
- [22] Sun S, Ishimoto T, Hagihara K, Tsutsumi Y, Hanawa T, Nakano T. Excellent mechanical and corrosion properties of austenitic stainless steel with a unique crystallographic lamellar microstructure via laser powder bed fusion. *Scr Mater* 2019;159:89–93.
- [23] Bertoli US, MacDonald BE, Schoenung JM. Stability of cellular microstructure in laser powder bed fusion of 316L stainless steel. *Mater Sci Eng A* 2019;739: 109–17.
- [24] Nguyena QB, Zhua Z, Nga FL, Chuua BW, Naia SML, Wei J. High mechanical strengths and ductility of stainless steel 304L fabricated using selective laser melting. *J Mater Sci Technol* 2019;35:388–94.
- [25] Smelov VG, Sotov AV, Agapovichev AV, Tomilina TM. Selective laser melting of metal powder of steel 316L. *Mater Sci Eng* 2016;142:012071.
- [26] Sande J, Hufenbach J, Giebler L, Wendrock H, Kühn U, Eckert J. Microstructure and properties of FeCrMoVC tool steel produced by Selective laser melting. *Mater Des* 2016;89:335–41.
- [27] Gua D, Chen H. Selective laser melting of high strength and toughness stainless steel parts: the roles of laser hatch style and part placement strategy. *Mater Sci Eng A* 2018;725:419–27.
- [28] Bandar A, Dariusz G, Tushar B, Jenn-Ming Y. Densification behavior, microstructural evolution, and mechanical properties of TiC/316L stainless steel nanocomposites fabricated by selective laser melting. *Mater Des* 2018;138: 119–28.
- [29] Chen H, Gu D, Dai D, Ma C, Xi Mujian. Microstructure and composition homogeneity, tensile property, and underlying thermal physical mechanism of selective laser melting tool steel parts. *Mater Sci Eng A* 2017;682:279–89.
- [30] Agapovichev AV, Sotov AV, Smelov VG, Sufiiarov VS, Masaylo DV. The investigation of microstructure and mechanical properties of tool steel produced by Selective laser melting technology. *Mater Sci Eng* 2018;441:012003.
- [31] Tucho WM, Lysne VH, Austb H, Sjolyst-Kverneland A, V.. Hansen investigation of effects of process parameters on microstructure and hardness of SLM manufacturing SS316L. *J Alloys Compd* 2018;740:910–25.
- [32] Murr LE, Martinez E, Gaytan SM, Ramirez DA, Machado BI, Shindo PW, Martinez JL, Medina F, Wooten J, Cisel D, Ackelid U, Wicker RB. Microstructural architecture, microstructures, and mechanical properties for a nickel-base superalloy fabricated by electron beam melting. *Metall Mater Trans A* 2011;42: 3491–508.
- [33] Frazier WE. Metal additive manufacturing: a review. *J Mater Eng Perform* 2014; 23(6):1917–28.

- [34] L Song, J Mazumder. "Real-time implementation of generalized predictive algorithm for direct metal deposition (DMD) process control." U.S. Patent 9,044,827, issued June 2, 2015.
- [35] Zhang J, Liou F, Seufzer W, et al. A coupled finite element cellular automaton model to predict thermal history and grain morphology of ti-6Al-4V during direct metal deposition (DMD). *Addit Manuf* 2016;11:32–9.
- [36] Levy GN, Schindel R, Kruth JP. Rapid Manufacturing and rapid tooling with layer manufacturing (LM) technologies, state of the art and future perspectives. *CIRP Ann Manuf Technol* 2003;52:589–609.
- [37] <https://www.smartechpublishing.com/news/metal-am-report-2018/>.
- [38] Amt B.S. "EN ISO/ASTM 52900: 2017-Additive manufacturing. General principles." Terminology.
- [39] Wohlers Report. Wohlers Associates. 2020.
- [40] Guo N, Leu MC. Additive manufacturing: technology, applications and research needs. *Front. Mech. Eng.* 2013;8:215–43.
- [41] Khajavi SH, Partanen J, Holmström J. Additive manufacturing in the spare parts supply chain. *Comput Ind* 2014;65:50–63.
- [42] Cong D, Zhou H, Ren Z, Zhang Z, Zhang H, Meng C, C.. Wang The thermal fatigue resistance of H13 steel repaired by a biomimetic laser remelting process. *Mater Des* 2014;55:597–604.
- [43] [https://www.slmsolutions.com/fileadmin/user\\_upload/SLM\\_Solutions\\_Gro\\_up\\_AG\\_Annual\\_Report\\_2018.pdf](https://www.slmsolutions.com/fileadmin/user_upload/SLM_Solutions_Gro_up_AG_Annual_Report_2018.pdf).
- [44] <https://www.netl.doe.gov/sites/default/files/event-proceedings/2017/utsr/general/Grylls.pdf>.
- [45] Wohlers report. 3D printing and additive manufacturing state of the industry. Wohlers Associates; 2019.
- [46] Liu Y, Yang Y, Mai S, Wang D, Song C. Investigation into spatter behavior during selective laser melting of AISI 316L stainless steel powder. *Mater Des* 2015;87:797–806.
- [47] Kruth JP, Froyen L, Vaerenbergh JV, Mercelis P, Rombouts M, Lauwers B. Selective laser melting of iron-based powder. *J Mater Process Technol* 2004;149(1–3):616–22.
- [48] Kruth JP, Levy G, Klocke F, Childs THC. Consolidation phenomena in laser and powder-bed based layered manufacturing." *CIRP Ann* 2007;56(2):730–59.
- [49] Stucker B. Additive manufacturing technologies: technology introduction and business implications. In: *Frontiers of engineering 2011: reports on leading-edge engineering from the 2011 symposium*; 2012. p. 19–21.
- [50] Lee HW, Jung KH, Hwang S-K, Kang SH, Kim DK. Microstructure and mechanical anisotropy of CoCrW alloy processed by selective laser melting. *Mater Sci Eng A* 2019;749:65–73.
- [51] Murr LE, Martinez E, Amato KN, Gaytan SM, Hernandez J, Ramirez DA, Shindo PW, Medina F, Wicker RB. Fabrication of metal and alloy components by additive manufacturing: examples of 3D materials science. *J Mater Res Technol* 2012;1:42–54.
- [52] Patil SN, Mulay AV, Ahuja BB. Development of experimental setup of metal rapid prototyping machine using selective laser sintering technique. *J Inst Eng (India) Ser C* 2018;99(2):159–67.
- [53] Mumtaz K, Hopkinson N. Top surface and side roughness of Inconel 625 parts processed using selective laser melting. *Rapid Prototyp J* 2009;15(2):96–103 (8).
- [54] Casavola C, Campanelli S, Pappalettere C. Preliminary investigation on distribution of residual stress generated by the selective laser melting process. *J Strain Anal Eng Des* 2009;44(1):93–104.
- [55] Ilin A, Logvinov R, Kulikov A, et al. Computer aided optimization of the thermal management during laser beam melting process. *Phys Procedia* 2014;56(56):390–9.
- [56] Hussein A, Hao L, Yan C, Everson R. Finite element simulation of the temperature and stress fields in single layers built without-support in selective laser melting. *Mater Des* 2013;52:638–47.
- [57] Jung HY, Choi SJ, Prashanth KG, Stoica M, Scudino S, Yi SH, Kim DH, Kim KB, Eckert J. Fabrication of Fe-based bulk metallic glass by selective laser melting: a parameter study. *Mater Des* 2015;86:703–8.
- [58] Jägle EA, Choi PP, Humbeek JV, et al. Precipitation and austenite reversion behavior of a maraging steel produced by selective laser melting. *J Mater Res* 2014;29:2072–9.
- [59] Gu DD, Meiners W, Wissenbach K, Poprawe R. Laser additive manufacturing of metallic components: materials, processes and mechanisms. *Int Mater Rev* 2012;57:116–33.
- [60] Prashanth KG, Eckert J. Formation of metastable cellular microstructures in selective laser melted alloys. *J Alloys Compd* 2017;707:27–34.
- [61] Spierings AB, Herres N, Levy G. Influence of the particle size distribution on surface quality and mechanical properties in AM steel parts. *Rapid Prototyp J* 2011;17:195–202.
- [62] Cherry JA, Davies HM, Mehmood S, Lavery NP, Brown SGR, Sieng J. Investigation into the effect of process parameters on microstructural and physical properties of 316L stainless steel parts by selective laser melting. *Int J Adv Manuf Technol* 2015;76:869–79.
- [63] Kong D, Ni X, Dong C, Zhang L, Mana C, Cheng X, Li X. Anisotropy in the microstructure and mechanical property for the bulk and porous 316L stainless steel fabricated via selective laser melting. *Mater Lett* 2019;235:1–5.
- [64] Hitzler L, Hirsch J, Heine B, Merkel M, Hall W, Öchsner A. On the anisotropic mechanical properties of selective laser-melted stainless steel. *Materials* 2017;10:1136.
- [65] Yadollahi A, Shamsaei N, Thompson SM, Elwany A, Bian L. Mechanical and microstructural properties of selective laser melted 17-4 PH stainless steel. In: *ASME 2015 Int. Mech. Eng. Congr. Expo. American Society of Mechanical Engineers*; 2015.
- [66] Laakso P, Riipinen T, Laukkanen A, Andersson T, Jokinen A, Revuelta A, Ruusuvuori K. Optimization and simulation of SLM process for high density H13 tool steel parts. In: *9th Int. Conf. Photonic Technol. LANE.* 83; 2016. p. 26–35.
- [67] Nakamoto T, Shirakawa N, Miyata Y, Inui H. Selective laser sintering of high carbon steel powders studied as a function of carbon content. *J Mater Process Technol* 2009;209:5653–60.
- [68] Mertens R, Vrancken B, Holmstock N, Kinds Y, Kruth J-P, Van Humbeek J. Influence of powder bed preheating on microstructure and mechanical properties of H13 tool steel SLM parts. *Phys Procedia* 2016;83:882–90.
- [69] Mutua J, Nakata S, Onda T, Chen Z. Optimization of selective laser melting parameters and influence of post heat treatment on microstructure and mechanical properties of maraging steel. *Mater Des* 2018;139:486–97.
- [70] Vilario T, Colin C, J.D Bartout". As-fabricated and heat-treated microstructures of the Ti6Al4 V alloy processed by selective laser melting". *Metallurgical and Materials Transactions A* 2011;42(10):3190–9.
- [71] Gong HJ, Rafi K, Gu HF, Starr T, Stucker B. Analysis of defect generation in Ti6Al4 V parts made using powder bed fusion additive manufacturing processes. *Addit Manuf* 2014;1–4:87–98.
- [72] Haboudou A, Peyre P, Vannes AB, Peix G. Reduction of porosity content generated during Nd:YAG laser welding of A356 and AA5083 aluminium alloys. *Mater Sci Eng A* 2003;363(1–2):40–52.
- [73] Zhang S, Gui RZ, Wei QS, Shi Y. "Cracking behaviour and formation mechanism of TC4 alloy formed by selective laser melting. *J Mech Eng* 2013;49(23):21–7 (in Chinese).
- [74] Li RD, Shi YS, Wang ZG, Wang L, Liu J, Jiang W. Densification behaviour of gas and water atomized 316L stainless steel powder during selective laser melting. *Appl Surf Sci* 2010;256(13):4350–6.
- [75] Gu D, Shen Y. Balling phenomena in direct laser sintering of stainless-steel powder: metallurgical mechanisms and control methods. *Mater Des* 2009;30(8):2903–10.
- [76] Mazur M, Leary M, McMillan M, Elambasseril J, Brandt M. SLM additive manufacture of H13 tool steel with conformal cooling and structural lattices. *Rapid Prototyp J* 2016;22:504–18.
- [77] Kempen K, Yasa E, Thijs L, Kruth J-P, Van Humbeek J. Microstructure and mechanical properties of selective laser melted 18Ni-300 steel. *Phys Procedia* 2011;12:255–63.
- [78] Yasa E, Kempen K, Kruth J-P, Thijs L, Van Humbeek J. Microstructure and mechanical properties of maraging steel 300 after Selective laser melting. *Solid Free Fabr Symp Proc* 2010:383–96.
- [79] Kempen K. Expanding the Materials Palette for Selective laser melting of Metals. 2015.
- [80] Yasa E, Poyraz O, Solakoglu EU, Akbulut G, Oren S. A study on the stair case effect in direct metal laser sintering of nickel-based super alloys. *Procedia CIRP* 2016;45:175–8.
- [81] Childs THC, Hauser C, Badrossamay M. Mapping and modelling single scan track formation in direct metal selective laser melting. *CIRP Annals* 2004;53(1):191–4.
- [82] Childs THC, Hauser C, Badrossamay M. Selective laser sintering (melting) of stainless and tool steel powders: experiments and modelling. *Proc Inst Mech Eng B J Eng Manuf* 2005;219(4):339–57.
- [83] Badrossamay M, Childs THC. Further studies in selective laser melting of stainless and tool steel powders. *Int J Mach Tool Manuf* 2007;47(5):779–84.
- [84] Li C, Fu CH, Guo YB, Fang FZ. A multiscale modeling approach for fast prediction of part distortion in selective laser melting. *J Mater Process Technol* 2016;229:703–12.
- [85] Contuzzi N, Campanelli SL, Ludovico AD. 3 d finite element analysis in the selective laser melting process. *Int J Simul Modell* 2011;10(3):113–21.
- [86] Peng T, Chen C. Influence of energy density on energy demand and porosity of 316L stainless steel fabricated by selective laser melting. *Int J Precis Eng Manuf Green Technol* 2018;5(1):55–62.
- [87] Shamsaei N, Yadollahi A, Bian L, Thompson SM. An overview of direct laser deposition for additive manufacturing; part II: mechanical behavior, process parameter optimization and control. *Addit Manuf* 2015;8:12–35.
- [88] Khairallah SA, Anderson A. Mesoscopic simulation model of selective laser melting of stainless-steel powder. *J Mater Process Technol* 2014;214(11):2627–36.
- [89] Liu B, Wildman R, Tuck C, Ashcroft I, Hague R. Investigation the effect of particle size distribution on processing parameters optimisation in selective laser melting process. In: *Additive manufacturing research group. Loughborough University*; 2011. p. 227–38.
- [90] H. Azizi, R. Ghiaasiaan, R. Prager, M.H. Ghoncheh, Khaled Abu Samk, Ante Lausic, Wes Byleveld, A.B. Phillion *Metallurgical and Mechanical Assessment of Hybrid Additively-Manufactured Maraging Tool Steels via Selective laser melting.*
- [91] Coe HG, Pasebani S. Use of bimodal particle size distribution in selective laser melting of 316L stainless steel. *J Manuf Mater Process* 2020;4(1):8.
- [92] Li C, Wang Y, Zhan H, Han T, Han B, Zhao W. Three-dimensional finite element analysis of temperatures and stresses in wide-band laser surface melting processing. *Mater Des* 2010;31(7):3366–73.
- [93] Roberts A, Wang CJ, Esterlein R, Stanford M, Mynors DJ. A three-dimensional finite element analysis of the temperature field during laser melting of metal powders in additive layer manufacturing. *Int J Mach Tools Manuf* 2009;49(12):916–23.
- [94] Gusarov AV, Kovalev EP. Model of thermal conductivity in powder beds. *Phys Rev B Condens Matter Mater Phys* 2009;80(2):16–20.
- [95] Gusarov AV, Kruth JP. Modelling of radiation transfer in metallic powders at laser treatment. *Int J Heat Mass Transf* 2005;48(16):3423–34.

- [96] Tolochko NK, Khlopkov YV, Mozzharov SE, Ignatiev MB, Laoui T, Titov VI. Absorbance of powder materials suitable for laser sintering. *Rapid Prototyp J* 2000;6:155–61.
- [97] Thomas M, Baxter GJ, Todd I. Normalised model-based processing diagrams for additive layer manufacture of engineering alloys. *Acta Mater* 2016;108:26–35.
- [98] Boley CD, Khairallah SA, Rubenchik AM. Calculation of laser absorption by metal powders in additive manufacturing. *Appl Optics* 2015;54(9):2477–82.
- [99] Le TN, Lo YL. Effects of sulfur concentration and marangoni convection on melt-pool formation in transition mode of selective laser melting process. *Mater Des* 2019;179:107866.
- [100] Khairallah SA, Anderson AT, Rubenchik A, King WE. Laser powder-bed fusion additive manufacturing: physics of complex melt flow and formation mechanisms of pores, spatter, and denudation zones. *Acta Mater* 2016;108:36–45.
- [101] Korner C, Attar E, Heintl P. Mesoscopic simulation of selective beam melting processes. *J Mater Process Technol* 2011;211(6):978–87.
- [102] Korner C, Bauereiß A, Attar E. Fundamental consolidation mechanisms during selective beam melting of powders 2013;21(8):85011.
- [103] Das S. Physical aspects of process control in selective laser sintering of metals. *Adv Eng Mater* 2003;5(10):701–11.
- [104] Cormier D, Harrysson O, West H. Characterization of H13 steel produced via electron beam melting. *Rapid Prototyp J* 2004;10(1):35–41.
- [105] AlMangour B, Grzesiak D, Yang J. Rapid fabrication of bulk-form TiB<sub>2</sub>/316L stainless steel nanocomposites with novel reinforcement architecture and improved performance by selective laser melting. *J Alloys Compd* 2016;680:480–93.
- [106] Glicksman ME. Principles of solidification: an introduction to modern casting and crystal growth concepts. Springer Science & Business Media; 2010.
- [107] Yadroitsova I, Yadroitsev I. Residual Stress in metal specimens produced by direct metal laser sintering. <https://sffsymposium.engr.utexas.edu/sites/default/files/2015/2015-49-Yadroitsev.pdf>.
- [108] Hanzl P, Zetek M, Baksa T, Kroupa T. The influence of processing parameters in the mechanical properties of SLM parts. *Energy Procedia* 2015;100C:1405–13.
- [109] Gong X, Chou K. Phase-field modeling of microstructure evolution in electron beam additive manufacturing. *JOM* 2015;67(5):1176–82.
- [110] Niendorf T, Leuders S, Riemer A, Richard HA, Schwarze D, Troster T. Highly anisotropic steel processed by selective laser melting. *The Minerals, Metals & Materials Society and ASM International*; 2013.
- [111] Lu Y, Wu S, Gan Y, Huang T, Yang C, Junjie L, Lin J. Study on the microstructure, mechanical property and residual stress of SLM Inconel-718 alloy manufactured by differing island scanning strategy. *Optics & Laser Technol* 2015;7:197–206.
- [112] Popovich A, Sufiarova VSh, Borisova EV, Polozova IA, Masayloa DV, Grigoriev AV. Anisotropy of mechanical properties of products manufactured using selective laser melting of powdered materials. *Russ J Non-Ferrous Metals* 2017;58:389–95.
- [113] Fathi A, Toyserkani E, Khajepour A, Durali M. Prediction of melt pool depth and dilution in laser powder deposition. *J Phys D Appl Phys* 2006;39:2613–23.
- [114] Mirkoochi E, Sievers DE, Garmestani H, Chiang K, Liang SY. Three-dimensional semi-elliptical modeling of melt pool geometry considering hatch spacing and time spacing in metal additive manufacturing. *J Mater Process* 2019;45:532–43.
- [115] Lee KH, Yun GJ. A novel heat source model for analysis of melt pool evolution in selective laser melting process. *Addit Manuf* 2020;36:101497.
- [116] P. Ninpetch, P. Kowitwarangkul, S. Mahathanabodee, P. Chalermkarnnon, P. Rattanadecho, Computational Investigation of Thermal Behavior and Molten Metal Flow with Moving Laser Heat Source for Selective Laser Melting Process, *Case Studies in Thermal Engineering*. 100860.
- [117] M. Lindroos, T. Pinomaa, A. Antikainen, J. Lagerbom, J. Reijonen, T. Lindroos, T. Andersson, and A. Laukkanen. "Micromechanical modeling approach to single track deformation, phase transformation and residual stress evolution during Selective Laser Melting using crystal plasticity." *Additive Manufacturing*: 101819.
- [118] L. Cao. "Mesoscopic-scale numerical investigation including the influence of scanning strategy on Selective Laser Melting process." *Computational Materials Science* 189: 110263.
- [119] Liu B, Fang G, Lei L, Liu W. A new ray tracing heat source model for mesoscale CFD simulation of selective laser melting (SLM). *App Math Model* 2020;79:506–20.
- [120] Liu Y, Zhang J, Pang Z. Numerical and experimental investigation into the subsequent thermal cycling during selective laser melting of multi-layer 316 L stainless steel. *Opt Laser Technol* 2018;98:23–32.
- [121] Panwisawas C, Qiu C, Anderson MJ, Sovani Y, Turner RP, Attallah MM, Brooks JW, Basoalto HC. Mesoscale modelling of selective laser melting: thermal fluid dynamics and microstructural evolution. *Comput Mater Sci* 2017;126:479–90.
- [122] Li C, Guo Y, Fang X, Fang F. A scalable predictive model and validation for residual stress and distortion in selective laser melting. *CIRP Annals* 2018;67(1):249–52.
- [123] Shiomi M, Osakada K, Nakamura K, Yamashita T, Abe F. Residual stress within metallic model made by selective laser melting process. *CIRP Ann* 2004;53:195–8.
- [124] Li L, Yan L, Chen Y, Pan T, Zhang X, Cui W, Flood A, Liou F. Predictive model for thermal and stress field in selective laser melting process—part II. *Procedia Manuf* 2019;39:547–55.
- [125] Tang Q, Chen P, Chen J, Chen Y, Chen H. Numerical simulation of selective laser melting temperature conduction behavior of H13 steel in different models. *Optik* 2020;201:163336.
- [126] Tian Y, Yang L, Zhao D, Huang Y, Pan J. Numerical analysis of powder bed generation and single track forming for selective laser melting of SS316L stainless steel. *J Mater Process* 2020;58:964–74.
- [127] B. Liu, G. Fang, and L. Lei. "An analytical model for rapid predicting molten pool geometry of Selective laser melting (SLM)." *Applied Mathematical Modelling* 92: 505–524.
- [128] Schanzel M, Shakirov D, Ilin A, Ploshikhin V. Coupled thermo-mechanical process simulation method for selective laser melting considering phase transformation steels. *Comput Math Appl* 2019;78(7):2230–46.
- [129] Baumard A, Ayrault D, Fandeur O, Bordreuil C, Deschaux-Beaume F. Numerical prediction of grain structure formation during laser powder bed fusion of 316 L stainless steel. *Mater Des* 2020;109434.
- [130] Kou S. *Welding metallurgy*. 2nd edition. John Wiley & Sons; 2003.
- [131] Wang C, Zhang J, Liu L, Fu H. Effect of melt superheating treatment on directional solidification Interface morphology of multi-component alloy. *J Mater Sci Technol* 2011;27(7):668–72.
- [132] Gäumann M, Henry S, Cléton F, Wagnière JD, Kurz W. Epitaxial laser metal forming: analysis of microstructure formation. *Mater Sci Eng A* 1999;271(1–2):232–41.
- [133] Kurz W, Fisher DJ. In: Enfield NH, editor. *Fundamentals of solidification*. 4th edition. Switzerland: CRC Press; 1998.
- [134] Shi Q, Gu D, Xia M, Cao S, Rong T. Effects of laser processing parameters on thermal behavior and melting/solidification mechanism during selective laser melting of TiC/Inconel 718 composites. *Optics Laser Technol* 2016;84:9–22.
- [135] Gu D. *Laser additive manufacturing of high-performance materials*. Springer; 2015.
- [136] Garibaldi M, Ashcroft I, Simonelli M, Hague R. Metallurgy of high-silicon steel parts produced using selective laser melting. *Acta Mater* 2016;110:207–16.
- [137] Krakhmalev P, Fredriksson G, Svensson K, Yadroitsev Z, Thuvander M, Peng R, Yadroitsova I. Microstructure, solidification texture, and thermal stability of 316 L stainless steel manufactured by laser powder bed fusion. *Metals* 2018;8:643.
- [138] Alnajjar M, Christien F, Wolski K, Bosch C. Evidence of austenite by-passing in a stainless steel obtained from laser melting additive manufacturing. *Addit Manuf* 2019;25:187–95.
- [139] Sun S, Hagihara K, Nakano T. Effect of scanning strategy on texture formation in ni-25 at.%Mo alloys fabricated by selective laser melting. *Mater Des* 2018;140:307–16.
- [140] Kurzynowski T, Gruber K, Stopyra W, Kuznicka B, Chlebus E. Correlation between process parameters, microstructure and properties of 316 L stainless steel processed by selective laser melting. *Mater Sci Eng A* 2018;718:64–73.
- [141] Tan C, Zhou K, Kuang M, Ma W, T. kuang. Microstructural characterization and properties of selective laser melted maraging steel with different build directions. *Sci Technol Adv Mater* 2018;19(1):746–58.
- [142] Sing SL, An J, Yeong WY, Wiria FE. Laser and electron-beam powder-bed additive manufacturing of metallic implants: a review on processes, materials and designs. *J Orthop Res* 2016;34(3):369–85.
- [143] Jung HY, Choi SJ, Prashanth KG, Stoica M, Scudino S, Yi S, Kühn U, Kim DH, Kime KB, Eckert J. Fabrication of Fe-based bulk metallic glass by selective laser melting: a parameter study. *Mater Des* 2015;86:703–8.
- [144] Qiu C, Al-Kindi M, Aladawi AS, Al-Hatmi I. A comprehensive study on microstructure and tensile behaviour of a selectively laser melted stainless steel. *Sci Rep* 2018;8:7785.
- [145] <https://arxiv.org/ftp/arxiv/papers/1801/1801.01408.pdf>.
- [146] Flemings MC. *Solidification processing*. New York: McGraw-Hill; 1974.
- [147] Zhang Q, Xue H, Tang Q, Pan S, Rettenmayr M, Zhu M. Microstructural evolution during temperature gradient zone melting: cellular automaton simulation and experiment. *Comput Mater Sci* 2018;146:204–12.
- [148] F. Yan, W. Xiong and E.J. Faierson. *Grain Structure Control of Additively Manufactured*.
- [149] Casalino G, Campanelli SL, Contuzzi N, Ludovico AD. Experimental investigation and statistical optimization of the selective laser melting process of a maraging steel. *Optics Laser Technol* 2015;65:151–8.
- [150] Sames WJ, List FA, Pannala S, Dehoff RR, Babu SS. The metallurgy and processing science of metal additive manufacturing. *Int. Mater. Rev.* 2016;61:315–60.
- [151] Collins PC, Brice DA, Samimi P, Ghamarian I, Fraser HL. Microstructural control of additively manufactured metallic materials. *Annu Rev Mat Res* 2016;46:63–91.
- [152] P. Murkute, S. Pasebani, O.B. Isgor. *Production of corrosion-resistant 316L stainless steel clads on carbon steel using powder bed fusion-Selective laser melting*.
- [153] Feuerhahn F, Schulzb A, Seefeldt T, Vollertsena F. Microstructure and properties of selective laser melted high hardness tool steel. *Phys Procedia* 2013;41:843–8.
- [154] Zhu Y, Zou J, Yang H, Zhu, et al. Wear performance of metal parts fabricated by selective laser melting: a literature review. *J Zhejiang Univ-Sci A (Appl Phys & Eng)* 2018;19(2):95–110.
- [155] Narasimharaju SR, Liu W, Zeng W, See TL, Scott P, Jiang X, Lou S. Surface texture characterization of metal selective laser melted part with varying surface inclinations. *J Tribol* 2021;143(5):051106.
- [156] Zhang B, Li Y, Bai Q. Defect formation mechanisms in selective laser melting: a review. *Chin J Mech Eng* 2017;30:515–27.
- [157] Morgan R, Sutcliffe CJ, O'neil W. Density analysis of direct metal laser re-melted 316L stainless steel cubic primitives. *J Mater Sci* 2004;39:1195–205.
- [158] Yakout M, Elbestawi MA, Veldhuis SC. A study of thermal expansion coefficients and microstructure during selective laser melting of Invar 36 and stainless steel 316L. *Addit Manuf* 2018;24:405–18.
- [159] Y.F. Shen, D. Gu and Y.F. Pan. *Balling Process in Selective Laser Sintering 316 Stainless Steel Powder*, 315-316/2006 pp 357-360.
- [160] Tang P, Wang S, Duan H, Long M, Li Y, Fan S, Chen D. The formation of humps and ripples during selective laser melting of 316L stainless steel. *JOM* 2020;72:3.

- [161] Yadroitsev I, Gusarov A, Yadroitsava I, Smurov I. Single track formation in selective laser melting of metal powders. *J Mater Process Technol* 2010;210:1624–31.
- [162] Yasa E, Kruth JP. Microstructural investigation of selective laser melting 316L stainless steel parts exposed to laser re-melting. *Procedia Eng* 2011;19:389–95.
- [163] Yasa E, Deckers J, Kruth JP. The investigation of the influence of laser re-melting on density, surface quality and microstructure of selective laser melting parts. *Rapid Prototyp J* 2011;17(5):312–27.
- [164] Song B, Dong SJ, Liao HL, Coddet C. Morphology evolution mechanism of single tracks of Fe-Al intermetallics in Selective Laser melting. *J Mater Res Innov* 2012;16:321–5.
- [165] Yadroitseva I, Krahkhaliev P, Yadroitsava I, Johansson S, Smurov I. Energy input effect on morphology and microstructure of selective laser melting single track from metallic powder. *J Mater Process Technol* 2013;213:606–13.
- [166] Galicki D, List F, Babu SS, Plotkowski A, Meyer III HM, Seals R, Hayes C. Localized changes of stainless steel powder characteristics during selective laser melting additive manufacturing. *Metall Mater Trans A* 2019;50A:1582–605.
- [167] Liverani E, Toschi S, Ceschini L, Fortunato A. Effect of selective laser melting (SLM) process parameters on microstructure and mechanical properties of 316L austenitic stainless-steel. *J Mater Process Technol* 2017;249:255–63.
- [168] Kaynak Y, Kitay O. Porosity, surface quality, microhardness and microstructure of selective laser melted 316L stainless steel resulting from finish machining. *J Manuf Mater Process* 2018;2:36.
- [169] King WE, Barth HD, Castillo VM, Gallegos GF, Gibbs JW, Hahn DE, Kamath C, Rubenchik AM. Observation of keyhole mode laser melting in laser powder-bed fusion additive manufacturing. *J Mater Process Technol* 2014;214:2915–25.
- [170] Wang D, Song C, Yang Y, Bai Y. Investigation of crystal growth mechanism during selective laser melting and mechanical property characterization of 316L stainless steel parts. *Mater Des* 2016;100:291–9.
- [171] Wang J, Wu WJ, Jing W, Tan X, Bi GJ, Tor SB, Leong KF, Chu CK, Liu E. Improvement of densification and microstructure of ASTM A131 EH36 steel samples additively manufactured via selective laser melting with varying laser scanning speed and hatch spacing. *Mater Sci Eng A* 2019;746:300–13.
- [172] Sun Z, Tan X, Tor SB, Yeong WY. Selective laser melting of stainless steel 316L with low porosity and high build rates. *Mater Des* 2016;104:197–204.
- [173] Xia M, Gu D, Yu G, Dai D, Chen H, Shi Q. Porosity evolution and its thermodynamic mechanism of randomly packed powder-bed during selective laser melting of inconel 718 alloy. *Int J Mach Tool Manuf* 2017;116:96–106.
- [174] Choo H, Sham KL, Bohling J, Ngo A, Xiao X, Ren Y, Depond PJ, Matthews MJ, Garlea E. Effect of laser power on defect, texture, and microstructure of a laser powder bed fusion processed 316L stainless steel. *Mater Des* 2019;164:107534.
- [175] Zheng H, Li H, Lang L, Gong S, Ge Y. Effects of scan speed on vapor plume behavior and spatter generation in laser powder bed fusion additive manufacturing. *J Manuf Process* 2018;36:60–7.
- [176] Dadbakhsha S, Humbeck JVan, Kruth J-P, Mertensa R. Application of base plate preheating during selective laser melting. *CIRP* 2018;74:5–11.
- [177] Mugwagwa L, Dimitrov D, Matope S, Yadroitsev I. Influence of process parameters on residual stress related distortions in selective laser melting. *Procedia Manuf* 2018;21:92–9.
- [178] Mercelis P, Kruth J-P. Residual stresses in selective laser sintering and selective laser melting. *Rapid Prototyp J* 2006;12:254–65.
- [179] Simson T, Emmel A, Dwars A, J. Böhm residual stress measurements on AISI 316L samples manufactured by selective laser melting. *Addit Manuf* 2017;17:183–9.
- [180] Kempen K, Vrancken B, Buls S, Thijs L. Selective laser melting of crack-free high density M2 high speed steel parts by baseplate preheating. *J Manuf Sci Eng* 2014;136(6).
- [181] <https://link.springer.com/content/pdf/10.1007%2Fs11837-003-0137-4.pdf>.
- [182] Harrison NJ, Todd I, Mumtaz K. Reduction of micro-cracking in nickel superalloys processed by selective laser melting: a fundamental alloy design approach. *Acta Mater* 2015;94:59–68.
- [183] Chen Y, Lu F, Zhang K, Nie P, Elmi Hosseini SR, Feng K, Li Z. Dendritic microstructure and hot cracking of laser additive manufactured inconel 718 under improved base cooling. *J Alloys Compd* 2016;670:312–21.
- [184] Chen Y, Zhang K, Huang J, Elmi-Hosseini SR, Li Z. Characterization of heat affected zone liquation cracking in laser additive manufacturing of inconel 718. *Mater Des* 2016;90:586–94.
- [185] Carter LN, Martin C, Withers PJ, Attallah MM. The influence of the laser scan strategy on grain structure and cracking behaviour in SLM powder-bed fabricated nickel superalloy. *J Alloys Compd* 2014;615:338–47.
- [186] Carter LN, Attallah MA, Reed RC. Laser powder bed fabrication of nickel base superalloys: influence of parameters, characterisation, quantification and mitigation of cracking. *Superalloys* 2012;2012:577–608.
- [187] Yu J, Rombouts M, Maes G. Cracking behavior and mechanical properties of austenitic stainless-steel parts produced by laser metal deposition. *Mater Des* 2013;45:228–35.
- [188] Cheruvathur S, Lass EA, Campbell CE. Additive manufacturing of 17–4 PH stainless steel: post-processing heat treatment to achieve uniform reproducible microstructure. *JOM* 2016;68:930–42.
- [189] Marchese G, Basile G, Bassini E, Aversa A, Lombardi M, Ugues D, Fino P, Biamino S. Study of the microstructure and cracking mechanisms of hastelloy X produced by laser powder bed fusion. *Materials* 2018;11:106.
- [190] Simonelli M, Tuck C, Aboukhalil NT, Maskery I, Ashcroft Ian, Wildman RD, Hague R. A study on the laser spatter and the oxidation reactions during selective laser melting of 316L stainless steel, Al-Si10-Mg, and Ti-6Al-4v. In: *The minerals, metals & materials society and asm international*; 2015.
- [191] <http://sffsymposium.engr.utexas.edu/Manuscripts/1999/1999-030-Hauser.pdf>.
- [192] Krell J, Röttger A, Geenen K, Theisen W. General investigations on processing tool steel X40CrMoV5-1 with selective laser melting. *J Mater Process Technol* 2018;255:679–88.
- [193] Jia Q, Gu D. Selective laser melting additive manufactured Inconel718 superalloy parts: high-temperature oxidation property and its mechanisms. *Optics Laser Technol* 2014;62:161–71.
- [194] <https://core.ac.uk/download/pdf/34507098.pdf>.
- [195] Letenneur M, Brailovski V, Kreitzberg A, Paserin V, Bailon-Poujol I. Laser powder bed fusion of water-atomized iron-based powders: process optimization. *J Manuf Mater Process* 2017;1:23.
- [196] Al-Mangour B. Powder metallurgy of stainless steel: state-of-the art, challenges, and development. *StainlSteel* 2015:37–80.
- [197] Hoeges S, Schade CT, Causton R. Development of a maraging steel powder for additive manufacturing. *MPIF World Congr. Powder Metall. Part. Mater* 2015. <https://businessdocbox.com/Metals/79943654-Development-of-a-maraging-steel-powder-for-additive-manufacturing-simon-hoeges-gkn-sinter-metals-engineering-gmbh-radevormwald-germany.html>.
- [198] Sun Y, Hebert RJ, Aindow M. Non-metallic inclusions in 17–4PH stainless steel parts produced by selective laser melting. *Mater Des* 2018;140:153–62.
- [199] Yan J, Zhou Y, Gu R, Zhang X, Quach W, Yan M. A comprehensive study of steel powders (316L, H13, P20 and 18Ni300) for their selective laser melting additive manufacturing. *Metals* 2019;9:86.
- [200] <https://iopscience.iop.org/article/10.1088/1757-899X/167/1/012048/pdf>.
- [201] Vasquez E, Giroux PF, Lomello F, Chniouelb A, Maskrotb H, Schuster F, Castanyd P. Elaboration of oxide dispersion strengthened fe-14Cr stainless steel by selective laser melting. *J Mater Process Technol* 2019;267:403–13.
- [202] <https://pdfs.semanticscholar.org/31fe/7c1b0344856e09bd5a7460781820c61362c3.pdf>.
- [203] Guo Q, Zhao C, Escano LI, Young Z, Xiong L, Fezzaa K, Everhart W, Brown B, Sun T, Chen L. Transient dynamics of powder spattering in laser powder bed fusion additive manufacturing process revealed by in-situ high-speed highenergy x-ray imaging. *Acta Mater* 2018;151:169–80.
- [204] Matthews MJ, Guss G, Khairallah SA, Rubenchik AM, Depond PJ, King WE. Denudation of metal powder layers in laser powder bed fusion. *Acta Materialia* 2016;114:33–42.
- [205] Yadroitsev I, Bertrand P, Smurov I. Parametric analysis of the selective laser melting process. *Appl Surf Sci* 2007;253:8064–9.
- [206] Bidare P, Bitharas I, Ward RM, Attallah MM, Moore AJ. Fluid and particle dynamics in laser powder bed fusion. *Acta Mater* 2018;142:107–20.
- [207] Zhang B, Dembinski L, Coddet C. The study of the laser parameters and environment variables effect on mechanical properties of high compact parts elaborated by selective laser melting 316L powder. *Mater Sci Eng A* 2013;584:21–31.
- [208] Rombout M, Kruth JP, Froyen L, Mercelis P. Fundamentals of Selective laser melting of alloyed steel powders. *CIRP Ann.* 2006;55:187–92.
- [209] Huang B, Zhai Y, Liu S, Mao X. Microstructure anisotropy and its effect on mechanical properties of reduced activation ferritic/martensitic steel fabricated by selective laser melting. *J Nucl Mater* 2018;500:33–41.
- [210] Tan C, Zhou K, Ma W, Zhang P, Liu M, Kuang T. Microstructural evolution, nanoprecipitation behavior and mechanical properties of selective laser melted high-performance grade 300 maraging steel. *Mater Des* 2017;134:23–34.
- [211] Boes J, Röttger A, Mutke C, Escher C, Theisen W. Microstructure and mechanical properties of X65MoCrWV3-2 cold-work tool steel produced by selective laser melting. *Addit Manuf* 2018;23:170–80.
- [212] Wang YM, Voisin T, McKeown JT, Ye J, Caltà NP, Li Z, Zeng Z, Zhang Y, Chen W, Roehling TT, Ott RT, Santala MK, Depond PJ, Matthews MJ, Hamza AV, Zhu T. Additively manufactured hierarchical stainless steels with high strength and ductility. *Nat Mater* 2018;17:63–70.
- [213] Davidson KP, Singamneni SB. Metallographic evaluation of duplex stainless-steel powders processed by selective laser melting". *Rapid Prototyp J* 2017;23:1146–63.
- [214] Wei M, Chen S, Xi L, Liang J, Liu CS. Selective laser melting of 24CrNiMo steel for brake disc: fabrication efficiency, microstructure evolution, and properties. *Optics Laser Technol* 2018;107:99–109.
- [215] Casati R, Coduri M, Lecis N, Andrianopoli C, Vedani M. Microstructure and mechanical behavior of hot-work tool steels processed by selective laser melting. *Mater Charact* 2018;137:50–7.
- [216] Yu H, Yang J, Yin J, Wang Z, Zeng X. Comparison on mechanical anisotropies of selective laser melted ti-6Al-4V alloy and 304 stainless steel. *Mater Sci Eng A* 2017;695:92–100.
- [217] Suryawanshi J, Prashanth KG, Ramamurty U. Mechanical behavior of selective laser melted 316L stainless steel. *Mater Sci Eng A* 2017;696:113–21.
- [218] Zhong Y, Liu L, Wikman S, Cui D, Shen Z. Intragranular cellular segregation network structure strengthening 316L stainless steel prepared by selective laser melting. *J Nucl Mater* 2016;470:170–8.
- [219] Jerrard PGE, Hao L, Evans KE. Experimental investigation into selective laser melting of austenitic and martensitic stainless steel powder mixtures. *Proc Inst Mech Eng B J Eng Manuf* 2009;223:1409–16.
- [220] Abd-Elghany K, Bourell DL. Property evaluation of 304L stainless steel fabricated by selective laser melting. *Rapid Prototyp J* 2012;18:420–8.
- [221] Niendorf T, Leuders S, Riemer A, Richard HA, Troster T, Schwarze D. Highly anisotropic steel processed by selective laser melting. *Metall Mater Trans B* 2013;44:794–6.

- [222] Gorsse S, Hutchinson C, Goune M, Banerjee R. Additive manufacturing of metals: a brief review of the characteristic microstructures and properties of steels, ti-6Al-4V and high-entropy alloys. *Sci Technol Adv Mater* 2017;18:584–610.
- [223] Sun Z, Tan X, Tor SB, Chua CK. Simultaneously enhanced strength and ductility for 3D-printed stainless steel 316L by selective laser melting. *NPG Asia Mater* 2018;10:127–36.
- [224] Sun S-H, Ishimoto T, Hagihara K, Tsutsumi Y, Hanawa T, Nakano T. Excellent mechanical and corrosion properties of austenitic stainless steel with a unique crystallographic lamellar microstructure via selective laser melting. *Scr Mater* 2019;159:89–93.
- [225] Shamsujjoha M, Agnew SR, Fitz-Gerald JM, Moore WR, Newman TA. High strength and ductility of additively manufactured 316L stainless steel explained. *Metall Mater Trans A* 2018;49:3011–27.
- [226] Jagle EA, Sheng Z, Kirmsteiner P, Oclok S, Weisheit A, Raabe D. Comparison of maraging steel micro- and nanostructure produced conventionally and by laser additive manufacturing. *Materials* 2017;10.
- [227] Sha W, Guo Z. Maraging steels: modelling of microstructure, properties and applications. New York: CRC Press; 2009.
- [228] Ren B, Lu D, Zhou R, Li Z, Guan J. Preparation and mechanical properties of selective laser melted H13 steel. *J Mater Res* 2019;1–11.
- [229] Facchini L, Vicente N, Lonardelli I, Magalini E, Robotti P, Molinari A. Metastable austenite in 17–4 precipitation-hardening stainless steel produced by selective laser melting. *Adv Eng Mater* 2010;12:184–8.
- [230] Clausen B, Brown DW, Carpenter JS, Clarke KD, Clarke AJ, Vogel SC, et al. Deformation behavior of additively manufactured GP1 stainless steel. *Mater Sci Eng A* 2017;696:331–40.
- [231] Sun Y, Hebert RJ, Aindow M. Effect of heat treatments on microstructural evolution of additively manufactured and wrought 17–4PH stainless steel. *Mater Des* 2018;156:429–40.
- [232] Haase C, Bültmann J, Hof J, Ziegler S, Bremen S, Hinke C, Schwedt A, Prah U, Bleck W, Haase C, Bültmann J, Hof J, Ziegler S, Bremen S, Hinke C, Schwedt A, Prah U, Bleck W. Exploiting process-related advantages of selective laser melting for the production of high-manganese steel. *Materials* 2017;10:56.
- [233] Walker JC, Berggreen KM, Jones AR, Sutcliffe CJ. Fabrication of Fe-Cr-Al oxide dispersion strengthened PM2000 alloy using selective laser melting. *Adv Eng Mater* 2009;11:541–6.
- [234] Boegelein T, Dryepondt SN, Pandey A, Dawson K, Tatlock GJ. Mechanical response and deformation mechanisms of ferritic oxide dispersion strengthened steel structures produced by selective laser melting. *Acta Mater* 2015;87:201–15.
- [235] Tatlock GJ, Dawson K, Boegelein T, Moustoukas K, Jones AR. High resolution microstructural studies of the evolution of nano-scale, yttrium-rich oxides in ODS steels subjected to ball milling, selective laser melting or friction stir welding. *Mater Today Proc* 2016;3:3086–93.
- [236] Hunt RM, Kramer KJ, El-dasher B. Selective laser sintering of MA956 oxide dispersion strengthened steel. *J Nucl Mater* 2015;464:80–5.
- [237] Li X, Zhang CH, Zhang S, Wu CL, Zhang JB, Chen HT, Abdulla Adil O. Design, preparation, microstructure and properties of novel wear-resistant stainless steel-base composites using laser melting deposition. *Vacuum* 2019;165:139–47.
- [238] Y. Sun, A. Moroz, and K. Alrbaey. Sliding Wear Characteristics and Corrosion Behaviour of Selective Laser Melted 316L Stainless Steel.
- [239] Lia H, Ramezania M, Li M, Ma C, Wang J. Tribological performance of selective laser melted 316L stainless steel. *Tribol Int* 2018;128:121–9.
- [240] Townsend A, Senin N, Blunt L, Leach RK, Taylor JS. Surface texture metrology for metal additive manufacturing: a review. *Precis Eng* 2016;46:34–47.
- [241] Gogolewski D, Bartkowiak T, Kozior V, Zmarzly P. Multiscale analysis of surface texture quality of models manufactured by laser powder-bed fusion technology and machining from 316L steel. *Materials* 2021;14(11):2794.
- [242] Strano G, Hao L, Everson RM, Evans KE. Surface roughness analysis, modelling and prediction in selective laser melting. *J Mater Process Technol* 2013;213: 589–97.
- [243] Lou S, Zhu Z, Zeng W, Majewski C, Scott PJ, Jiang X. Material ratio curve of 3D surface topography of additively manufactured parts: an attempt to characterise open surface pores. *Surf Topogr Metrol Prop* 2021;9(1):015029.
- [244] K. Alrbaey, D. Wimpenny, R. Tosi, W. Manning, and A. Moroz. On Optimization of Surface Roughness of Selective Laser Melted Stainless Steel Parts: A Statistical Study.
- [245] Mohammadian N, Turenne S, Brailovski V. Surface finish control of additively-manufactured inconel 625 components using combined chemical-abrasive flow polishing. *J Mater Process Technol* 2018;252:728–38.
- [246] X. Yan, C. Chen, R. Zhao, W. Ma, R. Bolot, J. Wang, Z. Ren, H. Liao, M. Liu. Selective laser melting of WC reinforced maraging steel 300: Microstructure characterization and tribological performance.
- [247] Bandar A, Jenn-Ming Y. Improving the surface quality and mechanical properties by shot-peening of 17–4 stainless steel fabricated by additive manufacturing. *bandar. Mater Des* 2016;110:914–24.
- [248] Wen S, Hu H, Zhou Y, Chen Z, Wei Q, Shi Y. Enhanced hardness and wear property of S136 mould steel with nano-TiB<sub>2</sub> composites fabricated by selective laser melting method. *Appl Surf Sci* 2018;457:11–20.
- [249] Yadollahi A, Shamsaei N, Thompson SM, Elwany A, Bian L. Effects of building orientation and heat treatment on fatigue behavior of selective laser melted 17–4 PH stainless steel. *Int J Fatigue* 2017;94:218–35.
- [250] Yin YJ, Sun JQ, Guo J, Kan XF, Yang DC. Mechanism of high yield strength and yield ratio of 316 L stainless steel by additive manufacturing. *Mater Sci Eng A* 2019;744:773–7.
- [251] Saeidi K, Gao X, Zhong Y, Shen ZJJ. Hardened austenite steel with columnar sub-grain structure formed by laser melting. *Mater Sci Eng A* 2014;625:221–9.
- [252] Guan K, Wang Z, Gao M, Li X, Zeng X. Effects of processing parameters on tensile properties of selective laser melted 304 stainless steel. *Mater Des* 2013;50:581–6.
- [253] Lewandowski JJ, Seifi M. Metal additive manufacturing: a review of mechanical properties. *Annu Rev Mat Res* 2016;46:14.
- [254] Lou X, Andresen PL, Rebak RB. Oxide inclusions in laser additive manufactured stainless steel and their effects on impact toughness and stress corrosion cracking behavior. *J Nucl Mater* 2018;499:182–90.
- [255] Carlton HD, Haboub A, Gallegos GF, Parkinson DY, MacDowell AA. Damage evolution and failure mechanisms in additively manufactured stainless steel. *Mater Sci Eng A* 2016;651:406–14.
- [256] Saeidi K, Alvi S, Lofaj F, Petkov VI, Akhtar F. Advanced mechanical strength in post heat treated SLM 2507 at room and high temperature promoted by hard/ductile sigma precipitates. *Metals* 2019;9:199.
- [257] Meredith SD, Zuback JS, Keist JS, Palmer TA. Impact of composition on the heat treatment response of additively manufactured 17–4 PH grade stainless steel. *Mater Sci Eng A* 2018;738:44–56.
- [258] Cheruvathur S, Lass EA, Campbell CE. Additive manufacturing of 17–4 PH stainless steel: post-processing heat treatment to achieve uniform reproducible microstructure. *JOM* 2015;68:930–42.
- [259] Guo Z, Kindt JT. Partitioning of size-mismatched impurities to grain boundaries in 2d solid hard-sphere monolayers. *Langmuir* 2018;34:12947–56.
- [260] Bai Y, Yang Y, Wang D, Zhang M. Influence mechanism of parameters process and mechanical properties evolution mechanism of maraging steel 300 by selective laser melting. *Mater Sci Eng A* 2017;703:116–23.
- [261] Becker T, Dimitrov D. The achievable mechanical properties of SLM produced maraging steel 300 components. *Rapid Prototyp J* 2016;22:487–94.
- [262] Safka J, Ackermann M, Voleský L. Structural properties of H13 tool steel parts produced with use of selective laser melting technology. *J Phys Conf Ser* 2016; 709.
- [263] Ren B, Lu D, Zhou R, Li Z, Guan J. Preparation and mechanical properties of selective laser melted H13 steel. *J Mater Res* 2019;1–11.
- [264] Dorfert R, Zhang J, Clausen B, Freife H, Schumacher J, Vollertsen F. Comparison of the fatigue strength between additively and conventionally fabricated tool steel 1.2344. *Addit Manuf* 2019;27:217–23.
- [265] Mazur M, Brincat P, Leary M, Brandt M. Numerical and experimental evaluation of a conformally cooled H13 steel injection mould manufactured with selective laser melting. *Int J Adv Manuf Technol* 2017;93:881–900.
- [266] Holzweissig MJ, Taube A, Brenne F, Schaper M, Niendorf T. Microstructural characterization and mechanical performance of hot work tool steel processed by selective laser melting. *Metall Mater Trans B Process Metall Mater Process Sci* 2015;46:545–9.
- [267] Tewari R, Mazumder S, Batra IS, Dey GK, Banerjee S. Precipitation in 18 wt% ni maraging steel of grade 350. *Acta Mater* 2000;48:1187–200.
- [268] Montero-Sistiaga ML, Godino-Martinez M, Boschmans K, Kruth J-P, Humbeeck JV, Vanmeensel K. Microstructure evolution of 316L produced by HP-SLM (high power selective laser melting). *Addit Manuf* 2018;23:402–10.
- [269] Mahmoudi M, Elwany A, Yadollahi A, Thompson SM, Bian L, Shamsaei N. Mechanical properties and microstructural characterization of selective laser melted 17–4 PH stainless steel. *Rapid Prototyp J* 2017;23:280–94.
- [270] Yan X, Chen C, Zhao R, Ma W, Bolot R, Wang J, Ren Z, Liao H, Liu M. Selective laser melting of WC reinforced maraging steel 300: microstructure characterization and tribological performance. *Surf Coat Technol* 2019;371: 355–65.
- [271] Pasebani S, Ghayoor M, Badwe S, Irrinki H, Atre SV. Effects of atomizing media and post processing on mechanical properties of 17-4 PH stainless steel manufactured via selective laser melting. *Addit Manuf* 2018;22:127–37.
- [272] Zhu Y, Peng T, Jia G, Zhang H, Xu S, Yang H. Electrical energy consumption and mechanical properties of selectivelaser-melting-produced 316L stainless steel samples using various processing parameters. *J Clean Prod* 2019;208:77–85.
- [273] Kamariah MSIN, Harun WSW, Khalil NZ, Ahmad F, Ismail MH, Sharif S. Effect of heat treatment on mechanical properties and microstructure of selective laser melting 316L stainless steel. *Mater Sci Eng* 2017;257:012021.
- [274] Zhai Y, Huang B, Mao X, Zheng M. Effect of hot isostatic pressing on microstructure and mechanical properties of CLAM steel produced by selective laser melting. *J Nucl Mater* 2019;515:111–21.
- [275] Salmana OO, Gamber C, Chaubey AK, Eckert J, Scudino dS. Effect of heat treatment on microstructure and mechanical properties of 316L steel synthesized by selective laser melting. *Mater Sci Eng A* 2019;748:205–12.
- [276] Kruth J-P, Mercelis P, Van Vaerenbergh J, Froyen L, Rombouts M. Binding mechanisms in selective laser sintering and selective laser melting. *Rapid Prototyp J* 2005;11:26–36.
- [277] Miroslav P, Pavlina T, Jana H, Pavel S, Boivie K. A study of selective laser melting technology on the ultra-high strength tool steel use—quality, mechanical properties and fatigue. *Applied mechanics, behavior of materials, and engineering systems. El- Qued* 2016.
- [278] Srivatsan TS, Sudarshan TS. Additive manufacturing: Innovations, advances, and applications. New York: CRC Press; 2015.
- [279] Stoffregen HA, Butterweck K, Abele E. Fatigue analysis in Selective laser melting: review and investigation of thin-walled actuator housings. In: *Proceedings of the 25th solid freeform fabrication symposium, Austin, 2014.*
- [280] Lai J, Huang H, Buising W. Effects of microstructure and surface roughness on the fatigue strength of high-strength steels. *Procedia Struct Integr* 2016;2:1213–20.
- [281] Uhlmann E, Fleck C, Gerlitzky G, Faltin F. Dynamical fatigue behavior of additive manufactured products for a fundamental life cycle approach. *Procedia CIRP* 2017;61:588–93.

- [282] Spierings AB, Starr TL, Wegener K. Fatigue performance of additive manufactured metallic parts. *Rapid Prototyp J* 2013;19:88–94.
- [283] Riemer A, Leuders S, Thöne M, Richard HA, Tröster T, Niendorf T. On the fatigue crack growth behavior in 316L stainless steel manufactured by selective laser melting. *Eng Fract Mech* 2014;120:15–25.
- [284] Suryawanshi J, Prashanth KG, Ramamurthy U. Tensile, fracture, and fatigue crack growth properties of a 3d printed maraging steel through selective laser melting. *J Alloys Compd* 2017;725:355–64.
- [285] Ziolkowski G, Chlebus E, Szymczyk P, Kurzac J. Application of X-ray CT method for discontinuity and porosity detection in 316L stainless steel parts produced with SLM technology. *Archiv Civ Mech Eng* 2014;14:608–14.
- [286] Shrestha R, Simsirirwong J, Shamsaei N, Thompson SM, Bian L. Effect of build orientation on the fatigue behavior of stainless steel 316L manufactured via laser powder bed fusion process. In: 27th Annual solid freeform fabrication symposium proceedings, Austin; 2016.
- [287] Blinn B, Klein M, Gläßner C, Smaga M, Aurich JC, Beck T. An investigation of the microstructure and fatigue behavior of additively manufactured AISI 316L stainless steel with regard to the influence of heat treatment. *Metals* 2018;8(4): 1–23.
- [288] Blinn B, Klein M, Beck T. Determination of the anisotropic fatigue behaviour of additively manufactured structures with short-time procedure PhyBal. In: MATEC web of conferences; 2018.
- [289] Carneiro L, Jalalahmadi B, Ashtekar A, Jiang Y. Cyclic deformation and fatigue behavior of additively manufactured 17–4 PH stainless steel. *Int J Fatigue* 2019; 123:22–30.
- [290] Nezhdafar PD, Shrestha R, Phan N, Shamsaei N. Fatigue behavior of additively manufactured 17–4 PH stainless steel: synergistic effects of surface roughness and heat treatment. *Int J Fatigue* 2019;124:188–204.
- [291] Nezhdafar PD, Burford E, Anderson-Wedge K, Zhang B, Shao S, Daniewicz SR, et al. Fatigue crack growth behavior of additively manufactured 17-4 PH stainless steel: effects of build orientation and microstructure. *Int. J. Fatigue* 2019;123: 168–79.
- [292] Crocchio D, De Agostinis M, Fini S, Olmi G, Vranic A, Ciric-Kostic S. Influence of the build orientation on the fatigue strength of EOS maraging steel produced by additive metal machine. *Fatigue Fract Eng Mater Struct* 2016;39:637–47.
- [293] Yin GQ, Kang X, Zhao GP. Fatigue properties of the ultra-high strength steel TM210A. *Materials* 2017;10.
- [294] Chen Q, Nagano T, Nakamura Y, Maeda Y, Kawagoishi N. Initiation and propagation behavior of a fatigue crack of maraging steel in high humidity. In: 13th Int. Conf. Fract; 2013.
- [295] Zhang M, Sun CN, Zhang X, Goh PC, Wei J, Li H, et al. Elucidating the relations between monotonic and fatigue properties of laser powder bed fusion stainless steel 316L. *JOM* 2018;70(3):390–5.
- [296] Zhang M, Sun CN, Zhang X, Goh PC, Wei J, Hardacre D, et al. Fatigue and fracture behaviour of laser powder bed fusion stainless steel 316L: influence of processing parameters. *Mater Sci Eng A* 2017;703:251–61.
- [297] Bodziak S, Al-Rubaie KS, Valentina LD, Lafratta FH, Santos EC, Zanatta AM, Y. Chen precipitation in 300 grade maraging steel built by selective laser melting: aging at 510 °C for 2 h. *Mater Charact* 2019;151:73–83.
- [298] F.F Conde, J. D. Escobar, J.P. Oliveira, M. Béres, A.L. Jardini, W.W. Bose, J.A. Avila. Effect of thermal cycling and aging stages on the microstructure and bending strength of a selective laser melted 300-grade maraging steel.
- [299] Yin S, Chen C, Yan X, Feng X, Jenkins R, O'Reilly P, Liu M, Li H, Lupoi R. The influence of aging temperature and aging time on the mechanical and tribological properties of selective laser melted maraging 18Ni-300 steel. *Addit Manuf* 2018; 22:592–600.
- [300] Kaynak Y, Kitay O. The effect of post-processing operations on surface characteristics of 316L stainless steel produced by selective laser melting. *Addit Manuf* 2019;26:84–93.
- [301] Song B, Dong S, Liu Q, Liao H, Coddet C. Vacuum heat treatment of iron parts produced by selective laser melting: microstructure, residual stress and tensile behavior. *Mater Des* 2014;54:727–33.
- [302] Elangswaran C, Cutolo A, Muralidharan GK, de Formanoir C, Berto F, Vanmeensel K, Hooreweder BV. Effect of post-treatments on the fatigue behaviour of 316L stainless steel manufactured by laser powder bed fusion. *Int J Fatigue* 2019;123:31–9.
- [303] Cabanettes F, Joubert A, Chardon G, Dumas V, Rech J, Grosjean C, Dimkovski Z. Topography of as built surfaces generated in metal additive manufacturing: a multi scale analysis from form to roughness. *Precis Eng* 2018;52:249–65.
- [304] M A Baciú, E R Baciú, C Bejinariu, S L Toma, A Danila and C Baciú. Influence of Selective laser melting Processing Parameters of Co-Cr-W Powders on the Roughness of Exterior Surfaces.
- [305] Rafi HK, Pal D, Patil N, Starr TL, Stucker BE. Microstructure and mechanical behavior of 17–4 precipitation hardenable steel processed by selective laser melting. *J Mater Eng Perform* 2014;23:4421–8.
- [306] Hengsbach F, Koppa P, Duschik K, Holzweissig MJ, Burns M, Nellesen J, Tillmann W, Troster T, Hoyer K-P, Schaper M. Duplex stainless steel fabricated by selective laser melting - microstructural and mechanical properties. *Mater Des* 2017;133:136–42.
- [307] Deirmina F, Peghini N, Almangour B, Grzesiak D, Pellizzari M. Heat treatment and properties of a hot work tool steel fabricated by additive manufacturing. *Mater Sci Eng A* 2019;753:109–21.
- [308] Åsberg M, Fredriksson G, Hatami S, Fredriksson W, Krakhmalev P. Influence of post treatment on microstructure, porosity and mechanical properties of additive manufactured H13 tool steel. *Mater Sci Eng A* 2019;742:584–9.
- [309] Mazumder J, Choi J, Nagarathnam K. The direct metal deposition of H13 tool steel for 3-D components. *J Occup Med* 1997;55–60 (Accessed 29 April 2013), <http://www.springerlink.com/index/6018462763247J00.pdf>.
- [310] Saeidi K, Gao X, Lofaj F, Kvetkova L, Shen ZJ. Transformation of austenite to duplex austenite-ferrite assembly in annealed stainless steel 316L consolidated by laser melting. *J Alloy Comp* 2015;633:463–9.
- [311] Lass EA, Stoudt MR, Williams ME. Additively manufactured nitrogen-atomized 17–4 PH stainless steel with mechanical properties comparable to wrought. *Mater Mater Trans A* 2019;50A:1619–24.
- [312] LeBrun T, Nakamoto T, Horikawa K, Kobayashi H. Effect of retained austenite on subsequent thermal processing and resultant mechanical properties of selective laser melted 17–4 PH stainless steel. *Mater Des* 2015;81:44–53.
- [313] Sarkar S, Siva Kumar C, Kumar Nath A. Effects of heat treatment and build orientations on the fatigue life of selective laser melted 15–5 PH stainless steel. *Mater Sci Eng A* 2019;755:235–45.
- [314] Liu Y, Pang Z, Zhang J. Comparative study on the influence of subsequent thermal cycling on microstructure and mechanical properties of selective laser melted 316L stainless steel. *Appl Phys A* 2017;123:688.
- [315] Yusuf SM, Nie M, Chen Y, Yang S, Gao N. Microstructure and corrosion performance of 316L stainless steel fabricated by selective laser melting and processed through high-pressure torsion. *J Alloys Compd* 2018;763:360–75.
- [316] Miranda G, Faria S, Bartolomeu F, Pinto E, Madeira S, Mateus A, Carreira P, Alves N, Silva FS, Carvalho O. Predictive models for physical and mechanical properties of 316L stainless steel produced by selective laser melting. *Mater Sci Eng A* 2016;657:43–56.
- [317] Davies CM, Withnell O, Ronnerberg T, Williams R, Hooper PA. Fracture analysis of 316L steel samples manufactured by selective laser melting. *Procedia Struct Integr* 2018;13:1384–9.
- [318] Bajaj P, Hariharan A, Anoop K, Kürnsteiner P, Raabe D, Jäggle EA. Steels in additive manufacturing: a review of their microstructure and properties. *Mater Sci Eng A* 2020;772:138633.
- [319] Garibaldi M, Ashcroft I, Hillier N, Harmon SAC, Hague R. Relationship between laser energy input, microstructures and magnetic properties of selective laser melted Fe-6.9%wt Si soft magnet. *Mater Charact* 2018;14(3):144–51.
- [320] Carluccio D, Xu C, Venezuela J, Cao Y, Kent D, Birmingham M, Demir AG, Previtali B, Ye Q, Dargusch M. Additively manufactured iron-manganese for biodegradable porous load-bearing bone scaffold applications. *Acta Biomater* 2020;103:346–60.
- [321] Mikler CV, Chaudhary V, Borkar T, Soni V, Jaeger D, Chen X, Contieri R, Ramanujan RV, Banerjee R. Laser additive manufacturing of magnetic materials. *JOM* 2017;69(3):532–43.
- [322] Carluccio D, Demir AG, Birmingham MJ, Dargusch MS. Challenges and opportunities in the selective laser melting of biodegradable metals for load-bearing bone scaffold applications. *Metall Mater Trans A Phys Metall Mater Sci* 2020;51A:3311–34.
- [323] Demir AG, Previtali B. Multi-material Selective laser melting of Fe/Al-12Si components. *Manuf Lett* 2017;11:8–11.